Numerical Simulation of Non-LTE Radiative Transfer and Atomic Physics Effects in Plasmas Created by Intense Proton Beams

J.J. MacFarlane, P. Wang, D.L. Henderson

January 1991

UWFDM-847

FUSION TECHNOLOGY INSTITUTE

UNIVERSITY OF WISCONSIN

MADISON WISCONSIN

Numerical Simulation of Non-LTE Radiative Transfer and Atomic Physics Effects in Plasmas Created by Intense Proton Beams

J.J. MacFarlane, P. Wang, D.L. Henderson

Fusion Technology Institute
University of Wisconsin
1500 Engineering Drive
Madison, WI 53706

http://fti.neep.wisc.edu

January 1991

UWFDM-847

Contents

1. Introduction

The purpose of this report is to provide a detailed description of work performed during the 1990 calendar year in the area of spectral diagnostics for ion beam-heated plasmas. This work has been supported by Kernforschungszentrum Karlsruhe (KfK) as part of a multiyear effort to develop theoretical models and computational tools that can be used to study high energy density plasmas created by KALIF (the Karlsruhe Light Ion Facility). To date, our efforts have primarily concentrated on the development and testing of a non-LTE (LTE $\equiv$ local thermodynamic equilibrium) radiative transfer/ionization balance code which can be used to predict the spectral radiation flux from laboratory plasmas. In addition, atomic physics codes have been developed to provide the data base for the radiative transfer code.

The statement of work for the 1990 calendar year is listed in Table 1. Each of these tasks will be described in detail below. In Section 2, progress in the development of the radiative transfer code is described. Here, we discuss all of the items in Tasks 1 and 6, along with some recent improvements in the areas of line profiles and convergence techniques. In Section 3, a discussion of the Dirac chord length method and its potential for improving the accuracy of the angle-averaging algorithm in the radiative transfer code is presented. In Section 4, we present the results of calculations in which we benchmarked the escape probability radiative transfer code with ONEDANT calculations.

Table 1. Tasks for 1990

1. Model attenuation of line radiation by bound-free absorption; compute bound-free coupling coefficients for calculating photoionization rates; include effects of "shifts" in photoionization edges for different ionization stages; compute frequency-dependent spectra for bound-bound and bound-free emission.

2. Perform calculations for potential KALIF targets; find suitable candidate lines for a temperature determination; examine emission and transport for K_α lines for diagnostic purposes; send preliminary results to KfK, preferably by the end of August 1990.

3. Document atomic physics models; compare results with experimental data (where available) and other calculations, especially at plasma conditions relevant to KALIF experiments ($T \sim 10 - 50$ eV, $\rho \sim 10^{-2}\rho_0$ and higher).

4. Examine Dirac chord length method to improve accuracy of angle-averaging technique in cylindrical and spherical geometries; compare with exact solutions for 2-level atom cases.

5. Benchmark escape probability code with S_N neutron transport code (either ONEDANT or ANISN).

6. Perform preliminary steps to model temperature and density gradients; work out details for model in which escape probability integrals are computed using line profiles based on local temperature and density conditions; begin implementation into radiative transfer code and perform test calculations.

A brief description of the atomic physics codes we use to compute the data base for the radiative transfer/ionization balance calculations is presented in Section 5. In addition, we compare the results of some of our atomic physics calculations with those from other published calculations and experimental data. A more detailed write-up of the atomic physics codes is currently being prepared by Wang Ping for his Ph.D. dissertation. This will be sent to KfK when completed. In Section 6, we describe results from our target (beam-plasma interaction) calculations. We have examined in particular the potential for using K_α satellite line radiation as a temperature diagnostic for beam-heated laboratory plasmas. We also discuss our recommendations concerning the types of targets that can be used for beam-plasma interaction experiments on KALIF. Finally, we present an overall summary of this year's work in Section 7.

2. Progress in the Development of the Non-LTE Radiative Transfer Code

2.1. Overview of Radiative Transfer/Ionization Balance Code

Let us first briefly review the major features of our non-LTE radiative transfer code (RTEP). Steady-state ionization and excitation populations are computed by solving multilevel atomic rate equations self-consistently with the radiation field. This is a collisional-radiative equilibrium (CRE) model which includes the effects of photoexcitation and photoionization on the level populations. Detailed configuration accounting (DCA) is used to track the populations of the atomic levels. That is, the population of each atomic level is determined by computing the collisional and radiative transition rates between each level. This type of model — as opposed to an average atom model, for instance — must be used to compute the detailed radiation spectra from laboratory plasmas.

The ionization processes considered in determining the atomic level populations are collisional ionization and recombination, photoionization and stimulated recombination, and radiative and dielectronic recombination. In addition, when proton beam effects are important (such as when computing the K_α line spectrum), proton-impact ionization and autoionization rates are also included. The excitation processes considered are collisional excitation and deexcitation, photoexcitation and stimulated emission, and spontaneous radiative decay. A description on the models used to compute the various transition rates is presented in Section 5.

The photoexcitation and photoionization rates depend on the characteristics of the radiation field. To evaluate these rates we use an escape probability radiation transport model (Apruzese et al. 1980, Apruzese 1981, MacFarlane et al. 1990, hereafter Paper I). This model employs angle- and frequency-averaging techniques that allow for computationally efficient solutions that produce only a modest loss in accuracy (typically ∼10-30%). The motivation for using this approach for non-LTE radiative transfer is that it can be coupled with hydrodynamics codes to study rapidly changing laboratory plasmas (Duston et al. 1983, Clark et al. 1986, Clark and Davis 1990).

2.2. Bound-Free Radiation Transport

We now discuss improvements to the radiative transfer code in modeling the transport of bound-free radiation. This work began in 1989, and initial results were described in Paper I. During 1990, the model was completed and benchmarked against ONEDANT calculations (see Section 4).

The frequency-averaged escape probability is obtained by averaging the attenuation factor, $e^{-\tau_\nu}$, over the emission profile ϕ_E:

$$P_e(\tau_0, \alpha_0) = \int_{\nu_1}^{\infty} \phi_E(\nu, \alpha_0) \exp(-\tau_\nu) d\nu, \tag{1}$$

where

$$\phi_E(\nu, \alpha_0) = \frac{\exp(-h\nu/kT_e)}{\nu E_1(\alpha_0)}$$

and

$$\alpha_0 \equiv h\nu_1/kT_e.$$

The optical depth and frequency at the photoionization edge are τ_0 and ν_1, respectively, τ_ν is the optical depth at frequency ν, T_e is the electron temperature, and $E_1(x)$ represents the exponential integral of order 1. The quantities h and k as usual refer to the Planck constant and Boltzmann constant, respectively.

As in the case of line transport, frequency-averaged escape probabilities have been fitted to simple analytic functions to allow for computationally efficient solutions. We have obtained new curve fits that are somewhat more accurate than those shown in Paper I. The curve fits are given by:

$$P_e(\tau_0, \alpha_0) = \begin{cases} e^{-\gamma_1 t} & , \quad t \leq 1.0 \\ t^{-1/3} \exp[-\gamma_1 - \gamma_2 (t^{1/3} - 1)] & , \quad t > 1.0 \end{cases} \tag{2}$$

where

$$\begin{aligned} \gamma_1(\alpha_0) &= 2.01\alpha_0 - 1.23\alpha_0^{3/2} + 0.210\alpha_0^2, \\ \gamma_2(\alpha_0) &= 1.01\alpha_0 + 0.0691\alpha_0^{3/2} - 0.0462\alpha_0^2, \end{aligned}$$

and $t \equiv \tau_0/3$. The fits are accurate to about 15% over a wide range of parameter space: $0.3 < \alpha_0 < 10$ and values of τ_0 such that $P_e(\tau_0, \alpha_0) \geq 10^{-5}$. Figure 1 shows a comparison of the numerical solution to Eq. (1) (solid curves) and the fitted values (dashed curves). For a constant optical depth, the escape probability increases as the electron temperature increases (i.e., as α_0 decreases). This occurs because as the temperature — and hence the mean thermal speed of electrons — increases, the photons emitted by recombinations tend to have energies farther above the threshold energy. Thus, as the photon energies become higher, the probability of photoabsorption decreases, and the escape probability increases.

The photoionization rate in zone a is obtained by summing the recombinations over all emitting zones e. Thus, the photoionization rate from lower level ℓ to upper level u can be written as:

$$\frac{dN_u^a}{dt} = \sum_{e=1}^{N_D} N_u^e \, n_e^e \, \alpha_{rr}^e \, Q^{ea}, \tag{3}$$

where α_{rr}^e is the radiative recombination rate coefficient for zone e, n_e^e is the electron density in zone e, and N_D is the total number of spatial zones in the plasma. The coupling coefficient, Q^{ea}, represents the probability that a photon emitted in zone e will be absorbed in zone a. These are obtained by integrating escape probability integrals over the emission zones. Formulae for evaluating Q^{ea} are given by Eqs. (17) and (26) in Paper I.

2.3. Calculation of Frequency-Dependent Emission Spectra

When calculating the atomic level populations self-consistently with the radiation field, we use *frequency-averaged* escape probabilities. Given those populations, the spectral flux is computed at a large number of frequency points. Thus, the computed spectral fluxes depend only indirectly on the frequency-averaged escape probabilities. We now describe how the frequency-dependent emission spectrum from a plasma is computed.

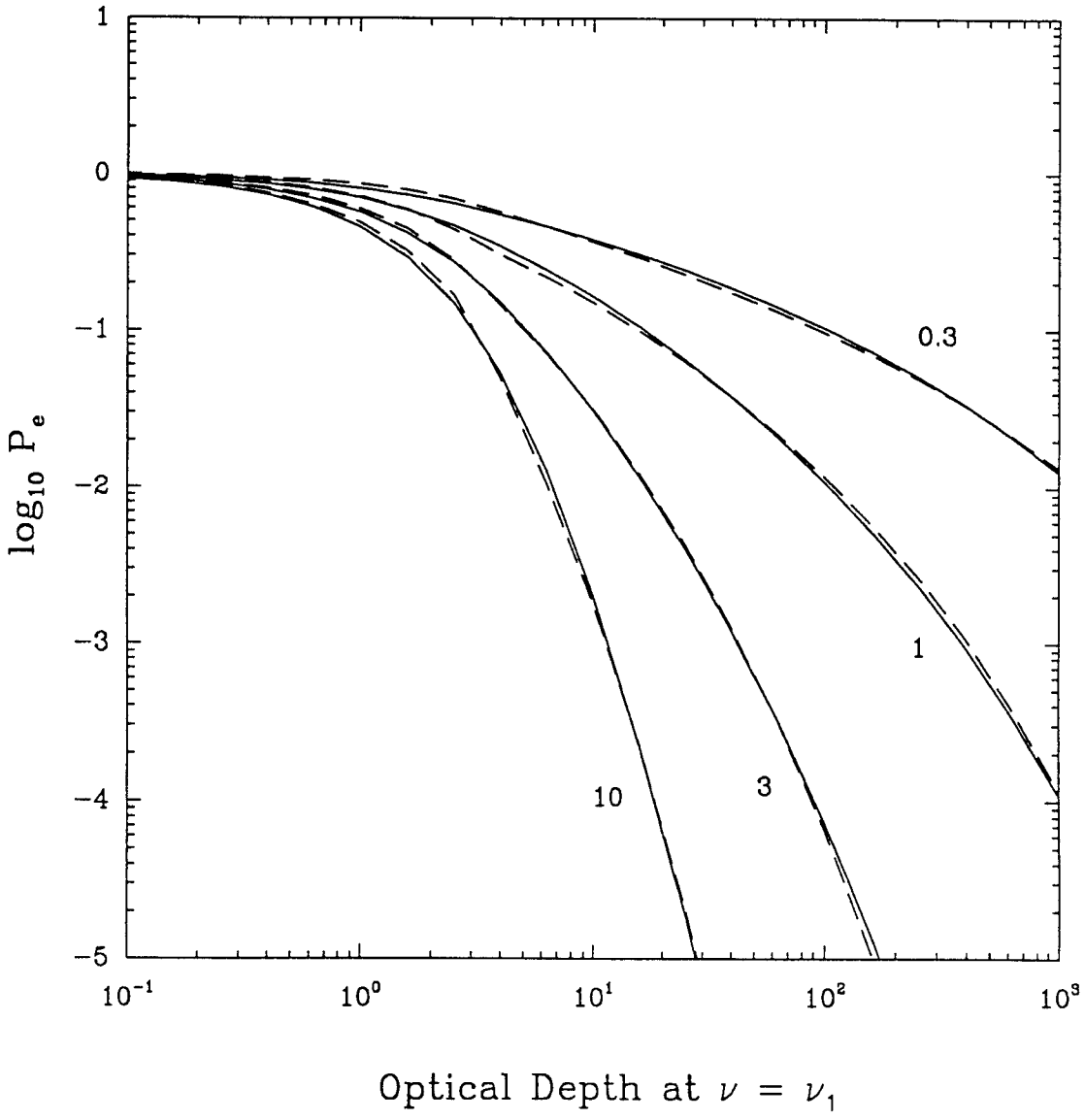

Figure 1. Frequency-averaged bound-free escape probabilities as a function of the optical depth at the photoionization edge. Numerical solutions (solid curves) are compared with fitted values (dashed curves). Curve labels correspond to different values of $\alpha_0 \equiv h\nu_1/kT_e$.

We first compute the opacities and optical depths in each spatial zone from all possible sources. At present, we consider the contributions from free-free (Bremsstrahlung), bound-free (photoabsorption), and bound-bound (line) transitions. The optical depth at frequency ν in zone d, is related to the opacity by:

$$\begin{aligned} \tau_{\nu,d} &= \int_{z_{min}}^{z_{min}} \chi_\nu(z) dz \\ &= \chi_{\nu,d}\ \Delta z_d, \end{aligned} \tag{4}$$

where the opacity in zone d, $\chi_{\nu,d}$, is assumed to be constant throughout the zone, and Δz_d is the zone thickness. The opacity can be written as (Mihalas 1978):

$$\begin{aligned} \chi_\nu &= \sum_j n_e n_{j+1} (1 - e^{h\nu/kT})\ \alpha^{ff}(\nu) \\ &+ \sum_j \sum_n \left[n_{nj} - n^*_{nj} e^{-h\nu/kT} \right]\ \alpha^{bf}_n(\nu) \\ &+ \sum_j \sum_n \sum_{m>n} \left[n_{nj} - \left(\frac{g_{nj}}{g_{mj}} \right) n_{mj} \right] \alpha^{bb}_{mn}(\nu), \end{aligned} \tag{5}$$

where the index j refers to the ionization stage, n and m refer to the excitation levels, n_e is the electron density, g_{nj} and g_{mj} are the statistical weights, n_{nj} is the number density of atoms in level n of ionization stage j, and n_{j+1} is the number density of atoms in ionization stage $j+1$ summed over all excitation levels. The quantity n^*_{nj} is the LTE population of state n_{nj} computed using the actual ion density of the upper ionization stage. The first term in Eq. (5) is the contribution from free-free absorption, the second is from bound-free absorption, and the third is due to bound-bound absorption. The free-free cross section is given by

$$\alpha^{ff}(\nu) = \left(\frac{4e^6}{3ch} \right) \left(\frac{3\pi}{3km_e} \right)^{1/2} \overline{g_{ff}}\ Z^2_{eff}\ T^{-1/2}\ \nu^{-3}, \tag{6}$$

where e and m_e are the electron charge and mass, respectively, c is the speed of light, $\overline{g_{ff}}$ is the free-free Gaunt factor (Karzas and Latter 1961), and Z_{eff} is the effective charge.

We use the hydrogenic frequency dependence for the bound-free cross section:

$$\alpha^{bf}(\nu) = \alpha^{bf}(\nu_1) \left(\frac{\nu_1}{\nu} \right)^3, \qquad \nu \geq \nu_1, \tag{7}$$

where ν_1 is the cutoff frequency. The value of $\alpha^{bf}(\nu_1)$ is determined such that it is consistent with the radiative recombination rate, which is based on Hartree-Fock calculations. The bound-bound cross section is given by

$$\alpha^{bb}(\nu) = \left(\frac{\pi e^2}{m_e c}\right) f_{nm} \phi_\nu,$$

where f_{nm} is the oscillator strength and ϕ_ν is the normalized line profile ($\int \phi_\nu d\nu = 1$).

After the total optical depth for each spatial zone is calculated, the frequency-dependent flux at the plasma boundary is computed as follows. The flux at the surface due to photons emitted in zone d, $F_{\nu,d}$, can be written in terms of the plasma emissivity of the zone, $\eta_{\nu,d}$:

$$F_{\nu,d} = \frac{4\pi \eta_{\nu,d} \Delta V_d}{A} \mathcal{A}_{\nu,d}, \tag{8}$$

where ΔV_d is the volume of zone d, and A is the area of the plasma boundary. The attenuation factor, $\mathcal{A}_{\nu,d}$, represents the attenuation due to all other zones along the path to the boundary. As before (Paper I), the path from the emitting zone to the boundary is defined by the "mean diffusivity angle." The optical depths for each zone are computed along this path. An example of this is illustrated in Figure 2, where $\Delta\tau_d$ is the optical depth of the emitting zone and τ_d is the optical depth from the plasma boundary to the closer boundary of zone d. The attenuation factor is then obtained by averaging over the emitting zone:

$$\mathcal{A}_{\nu,d} = \frac{1}{\Delta\tau_{\nu,d}} \int_{\tau_{\nu,d}}^{\tau_{\nu,d}+\Delta\tau_{\nu,d}} e^{-\tau_\nu} d\tau_\nu. \tag{9}$$

The emissivity can be written as (Mihalas 1978):

$$\begin{aligned} \eta_\nu &= \left(\frac{2h\nu^3}{c^2}\right) \sum_j \Bigg\{ n_e n_{j+1} e^{-h\nu/kT} \alpha^{ff}(\nu) \\ &+ \sum_n n^*_{nj} e^{-h\nu/kT} \alpha^{bf}_n(\nu) \\ &+ \sum_n \sum_{m>n} \left(\frac{g_{nj}}{g_{mj}}\right) n_{mj} \alpha^{bb}_{mn}(\nu) \Bigg\}. \end{aligned} \tag{10}$$

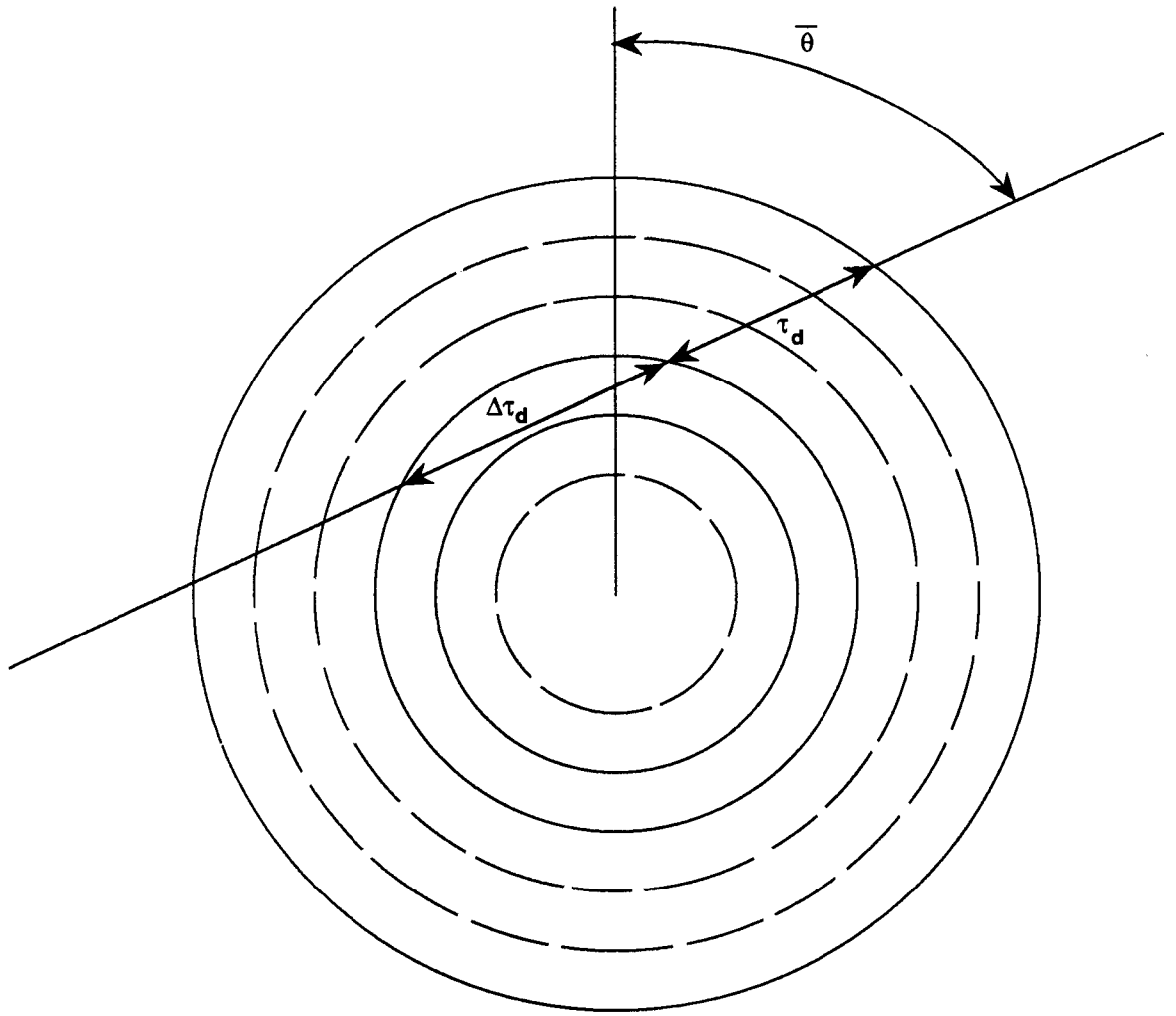

Figure 2. Schematic illustration of photon transport in cylindrical and spherical geometries. The mean diffusivity angle is indicated by $\bar{\theta}$.

An example of the frequency-dependent emission spectrum from a laboratory plasma is shown in Figure 3, where the flux has been computed for a planar Al plasma of thickness 0.1 mm, $T = 50$ eV, and $n = 10^{-2} n_0$ ($n_0 \equiv$ solid density). Shown along with the total flux are the contributions from free-free, bound-free, and bound-bound emission. Also shown for comparison is the blackbody spectrum.

Figure 3 shows that except at frequencies near optically thick lines, the greatest contribution to the flux below 100 eV is free-free emission. It is also seen that at energies below 30 eV, the calculated flux lies very close to the blackbody curve. This is because the free-free optical depth becomes larger than unity at lower photon energies ($\tau_{ff} \sim \nu^{-3}$). At energies above 100 eV, bound-free emission is the greater contributor to the continuum flux. The fluxes of a large number of emission lines exceed the continuum flux between 30 eV and 300 eV.

Note that the radiation produced by one type of transition can be significantly attenuated by other types of transitions. For instance, the free-free emission flux decreases abruptly near the cores of optically thick lines and photoabsorption edges. We note, however, that this interaction of the radiation field for different transitions is not fully accounted for when calculating the level populations. We do not expect this to be a serious deficiency in the model for most types of plasma diagnostics. But it is important to recognize that occasionally the approximations in the model will lead to inaccuracies.

2.4. Attenuation by Inner Shell Photoabsorption

Attenuation by inner shell photoabsorption has recently been included in computing emission spectra. The process — the ejection of an inner shell electron by a high energy photon — can significantly affect the observed spectral flux in an experiment (Duston et al. 1983). For example, when a relatively cold plasma lies between a hot x-ray-emitting plasma and a detector, high energy photons created in the hot region can be photoabsorbed in inner shell electrons of the cooler material.

The optical depth across zone d due to inner shell photoabsorption can be written as:

$$\tau_{\nu,d} = \sum_j \sum_s n_j N_s \alpha_{j,s}(\nu) \Delta z_d, \tag{11}$$

where N_s is the number of electrons in shell s, and n_j is the number density of ions in ionization stage j. Cross sections for each ionization stage and shell, $\alpha_{j,s}(\nu)$, are tabulated from Hartree-Fock calculations. For each ionization stage, we use the frequency-dependent cross sections corresponding to the ground state.

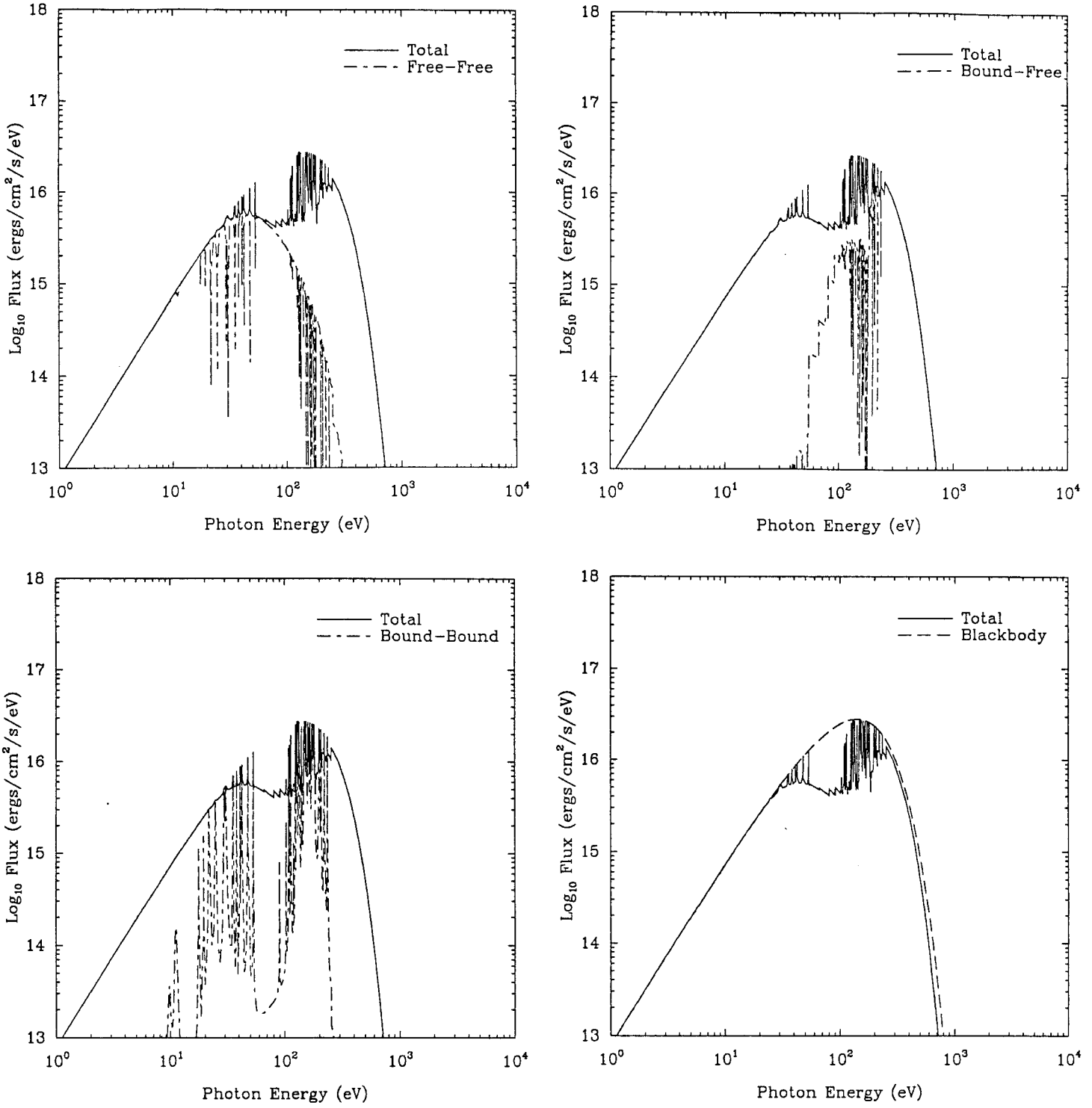

Figure 3. Calculated spectral flux from a 0.1 mm-thick Al plasma at $T = 50$ eV and $n = 10^{-2} n_0$. Contributions from free-free, bound-free, and bound-bound emission are indicated by dashed lines.

Figure 4 shows the calculated photoabsorption cross section for the first 10 ionization stages of Al. The curve for neutral Al is represented by the dashed line. Also shown for comparison are the calculated cross sections of Reilman and Manson (1979) for Al I and Al II. Note that the energy of the photoionization edges for the K-shell (near 1 to 2 keV) and L-shell (near 100 to 300 eV) electrons increases as the ionization increases. Our results are in good agreement with those of Reilman and Manson at energies above 50 eV. We expect our results to be more accurate in the 10 to 50 eV range because of the approximations used in the Reilman and Manson calculations.

An example of how inner shell absorption affects the opacity of a plasma is shown in Figure 5. The frequency-dependent optical depth is shown for an Al plasma at $T = 20$ eV, $n = 10^{-2} n_0$, and $L = 0.1$ cm. Shown with the total optical depth (solid curve) is the contribution to the absorption from inner shell electrons (dashed curve). Note that at photon energies above 0.5 keV this effect is the dominant continuum opacity. It is also seen that because of this effect, the continuum optical depth is ~ 1 around 1.5 keV. This suggests that inner shell absorption can affect the K_α satellite line spectrum in beam-plasma interaction experiments (see Section 6).

2.5. Voigt Line Profiles

In this section we will briefly describe improvements in our modeling of line profiles. We recently have added the capability of modeling Voigt line profiles. Thus, our code now has the capability to transport 3 types of line profiles: Doppler, Lorentz, and Voigt.

In evaluating the escape probability integrals we use an approach similar to that of Apruzese (1985). Simple analytical fits to exact numerical solutions to the frequency-averaged escape probability were obtained for two different regimes of the Voigt broadening parameter a. For $a < 0.49$:

$$P_e(\tau) = \begin{cases} (1 + 1.5\tau)^{-1} & (\tau \leq 1), \\ 0.4\tau^{-1} & (1 < \tau \leq \tau_c), \\ 0.4(\tau_c \tau)^{-1/2} & (\tau > \tau_c), \end{cases} \tag{12}$$

where

$$\tau_c \equiv \frac{0.83}{a(1 + a^{1/2})}.$$

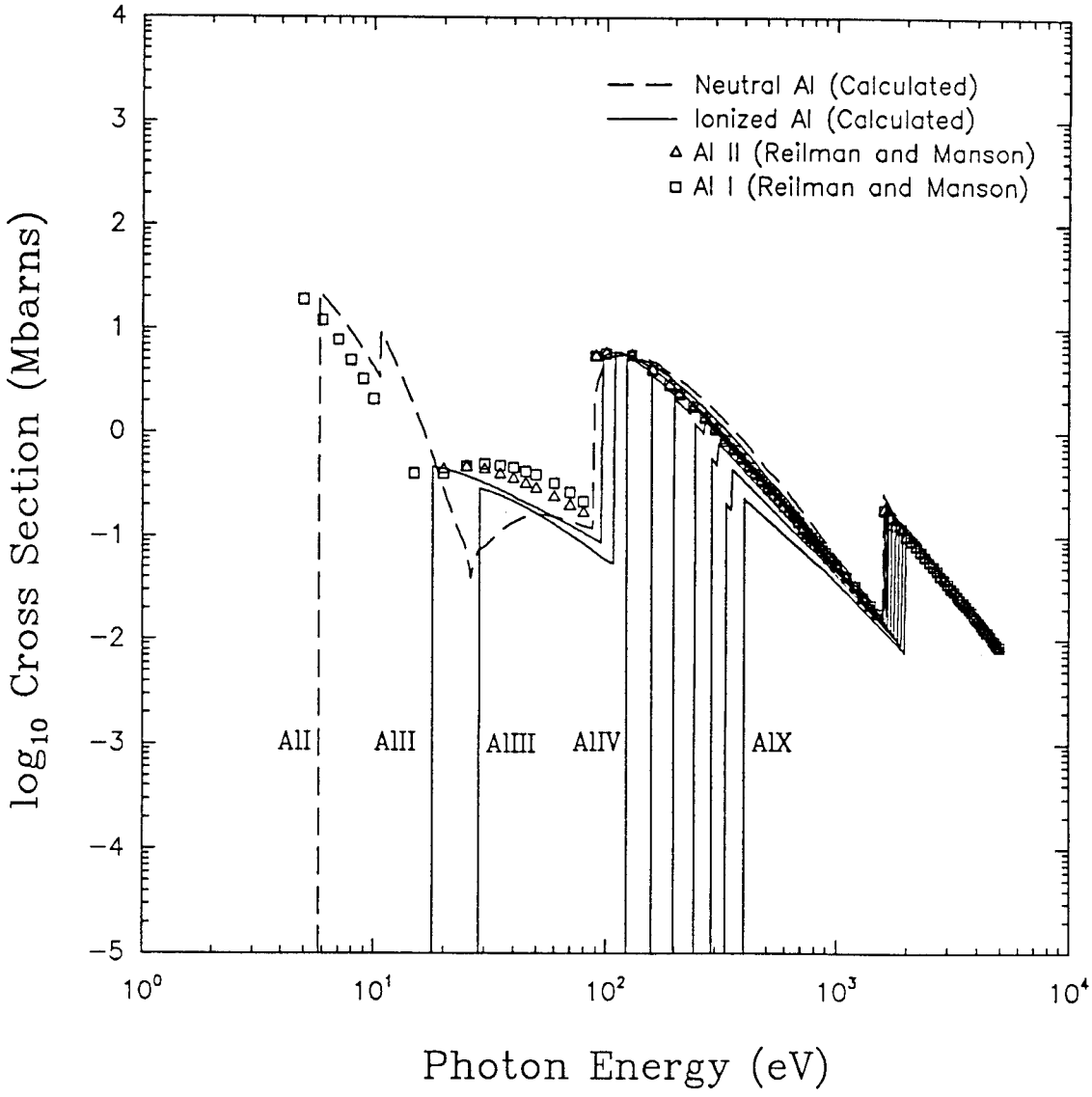

Figure 4. Calculated photoabsorption cross sections for neutral Al (dashed curve) and Al ions (solid curves). The squares and triangles represent the calculated cross sections of Reilman and Manson (1979).

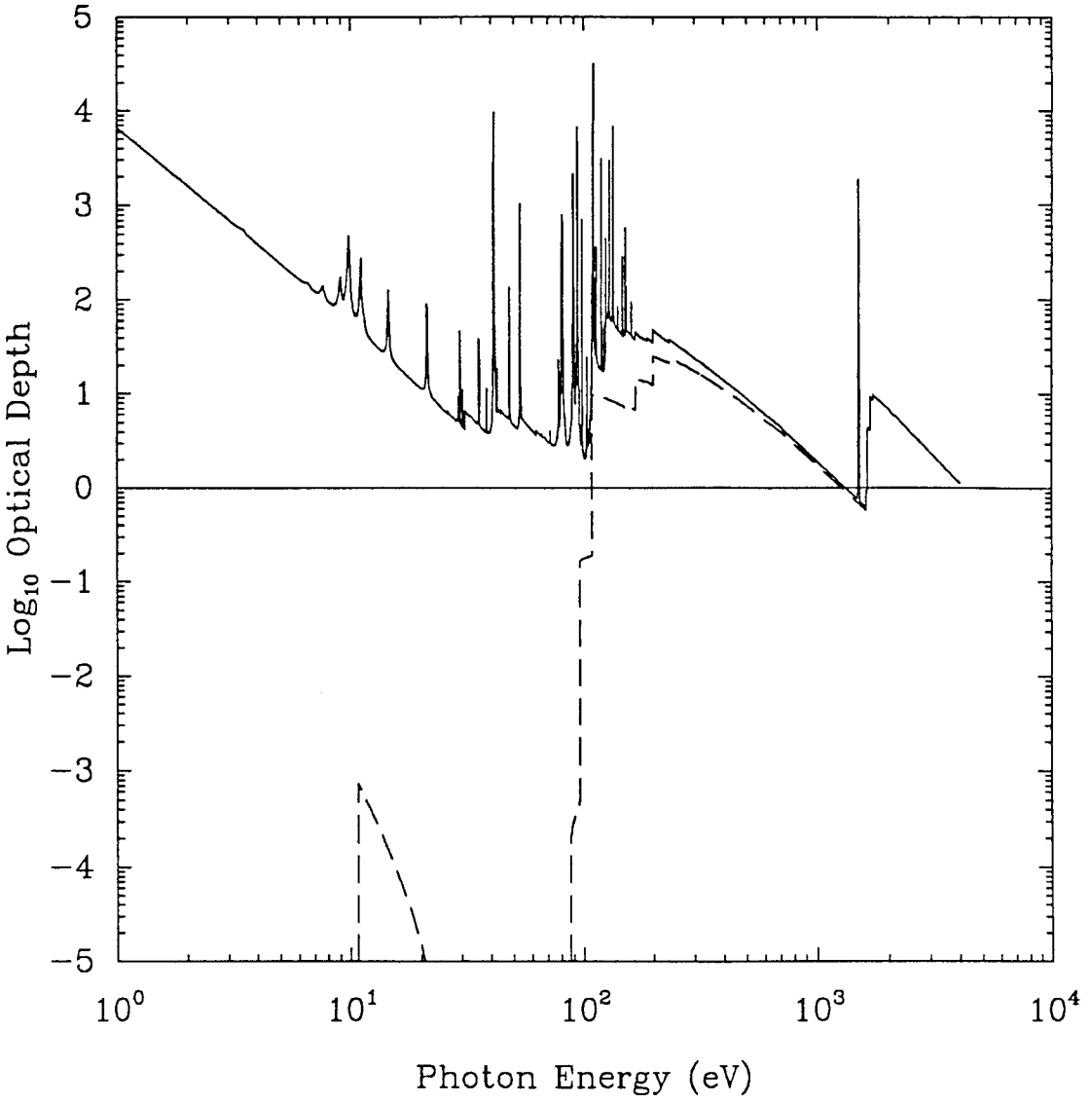

Figure 5. Frequency-dependent optical depths showing the influence of inner shell photoabsorption for Al at $T = 20$ eV, $n = 10^{-2} n_0$, and $L = 0.1$ cm. The inner shell contribution is indicated by the dashed curve.

For $a \geq 0.49$,

$$P_e(\tau) = \begin{cases} (1+\tau)^{-1} & (\tau \leq 1), \\ 0.5\ \tau^{-1/2} & (\tau > 1). \end{cases} \tag{13}$$

The fits are typically accurate to about 20%, although errors of up to 40% can occur. Note, however, that in our present model the frequency-averaged escape probability integrals are used only to compute the level populations self-consistently with the radiation field. The frequency-dependent spectral calculations do not directly use frequency-averaged escape probabilities.

The Voigt damping parameter $a_{u\ell}$ for the transition from the upper level u to the lower level ℓ can be written as (Duston and Davis 1981):

$$a_{u\ell} = \frac{\Gamma_{u\ell}}{4\pi\Delta\nu_D}, \tag{14}$$

where $\Delta\nu_D$ is the Doppler width, and $\Gamma_{u\ell}$ represents the sum of all radiative and collisional rates, R_{ij} and C_{ij}, depopulating the upper and lower levels:

$$\Gamma_{u\ell} = \sum_k (C_{uk} + R_{uk}) + \sum_k (C_{\ell k} + R_{\ell k}). \tag{15}$$

The values of $a_{u\ell}$ for each transition are then used to evaluate the escape probability integrals and zone-to-zone coupling coefficients, much like in the cases of Doppler and Lorentz profiles.

2.6. Convergence Considerations

In non-LTE radiative transfer codes, iterative methods are generally used to obtain atomic level populations that are consistent with the radiation field. The most straightforward iterative approach, known as Λ-iteration, is to compute the radiation field using level populations obtained from the most recent solution of the multilevel rate equations. This technique can have convergence problems when plasma densities are low and optical depths are large. We have recently added three new approaches for improving the convergence rates in our code. They are: (1) a Rybicki-type core-saturation method (Rybicki 1971, Apruzese et al. 1984), (2) a "collision-radiative switching" algorithm (Hummer and Voels 1988), and (3) an acceleration scheme originally proposed by Ng (1974).

The Rybicki-type core-saturation method is based on the description of Apruzese et al. (1984). When this approach is invoked, the populations on the first iteration are obtained

by diluting the spontaneous emission coefficients by a factor which accounts for the reabsorption of photons that do not escape the plasma. Stated mathematically, if P_e is the probability a photon will escape the entire plasma, the spontaneous emission coefficient, $A_{u\ell}$, is replaced by $A_{u\ell}P_e$. The zone-to-zone coupling model effectively accounts for the reabsorption of line core photons within the emitting cell. Thus, on subsequent iterations, the spontaneous emission coefficients are diluted in each zone by the escape probability from that zone. An analogous approach is also used for bound-free radiation. Although this approach has improved convergence in some instances, it has had a less significant overall impact on convergence than the other two convergence acceleration methods.

Collisional-radiative switching is a new approach that was recently reported by Hummer and Voels (1988). The basic idea is to "steer" the iteration process from the LTE solution (i.e., the starting point) to the non-LTE solution. To do this, we use a collisional switching parameter, λ_c, which multiplies all collisional rates by the same number. At first, this number is very large so that all collisional rates dominate their corresponding radiative rates. This of course leads to LTE level populations throughout the entire plasma. Then on subsequent iteration cycles, λ_c is decreased until it reaches a value of 1, at which point the correct non-LTE populations are obtained. This method has been particularly valuable for problems in which bound-free optical depths are very large.

The third method to improve convergence rates is based on the work of Ng (1974). More recent descriptions of implementing this approach for radiative transfer problems have been presented by Olson, Auer, and Buchler (1985) and Auer (1987). This method represents an extremely powerful acceleration technique that can be applied to any linearly convergent problem.

The Ng acceleration method is applied every several (perhaps 2 to 6) iterations to obtain updated solutions to the solution vector $\mathbf{x}$. In our case, the solution vector is the level populations in each spatial zone. The "accelerated" solution is calculated from solutions obtained during the past several iterations — that is, the evolution, or history, of the convergence becomes important. The accelerated solution vector after the n'th iteration can be written as:

$$\mathbf{x}^n = \left(1 - \sum_{m=1}^{M} \alpha_m\right) \mathbf{x}^{n-1} + \sum_{m=1}^{M} \alpha_m \mathbf{x}^{n-m-1}, \tag{16}$$

where $\mathbf{x}^{m-n}$ is the solution vector of the (n−m)'th iteration. The acceleration coefficients, α, are determined from the solution

$$\mathbf{A}\alpha = \mathbf{b}, \tag{17}$$

where the elements of **A** and **b** are given by:

$$\begin{aligned} A_{ij} &= \sum_{d=1}^{D} (\Delta x_d^n - \Delta x_d^{n-i})(\Delta x_d^n - \Delta x_d^{n-j}), \\ b_i &= \sum_{d=1}^{D} \Delta x_d^n (\Delta x_d^n - \Delta x_d^{n-i}), \end{aligned} \tag{18}$$

and

$$\Delta x_d^k \equiv x_d^k - x_d^{k-i}.$$

The quantity x_d^k refers to the d'th element of $\mathbf{x}$ on iteration cycle k. The order of the acceleration method, M, represents the number of previous cycles used to compute the accelerated solution for $\mathbf{x}$.

In our radiative transfer code M can be chosen to have a value from 2 to 4. It is found that using $M = 2$ provides very good acceleration to the final solution. This method has proven to be particularly valuable in improving the computational efficiency of our radiative transfer simulations.

2.7. Modeling of Temperature and Density Gradients

During the past year, we performed preliminary steps to model the effects of temperature and density gradients. This has been done to the extent that arrays tracking the temperature and density in each spatial zone are used, and the ionization, electron density, and atomic rate coefficients are computed for each zone. Test calculations have not yet been performed. We anticipate this model will be completed within the next year, and plan to benchmark our calculations with results from previously published papers and ONEDANT calculations.

With the exception of the transition rates that depend on the radiation field, temperature and density gradient effects are easily and accurately accounted for. This can be seen by examining the multilevel rate equations. The steady-state rate equation for level i can be written as:

$$\frac{dn_i}{dt} = -n_i \sum_{j \neq i}^{N_L} W_{ij} + \sum_{j \neq i}^{N_L} n_j W_{ji} = 0, \tag{19}$$

where W_{ij} and W_{ji} are the depopulating and populating rates between levels i and j, and N_L represents the total number of levels in the system. For upward transitions ($i < j$):

$$W_{ij} = B_{ij}\bar{J}_{ij} + n_e C_{ij} + n_e \gamma_{ij} + \beta_{ij}, \tag{20}$$

while for downward transitions ($i > j$):

$$W_{ij} = A_{ij} + B_{ij}\bar{J}_{ij} + n_e D_{ij} + n_e \alpha_{ij} + n_e^2 \delta_{ij}, \tag{21}$$

where n_e is the electron density and $\bar{J}_{ij} \equiv \int \phi_{ij}(\nu) J_\nu d_\nu$. The rate coefficients for the various transitions are represented by:

A_{ij} = spontaneous emission

B_{ij} = stimulated absorption ($i < j$) or emission ($i > j$)

C_{ij} = collisional excitation

D_{ij} = collisional deexcitation

α_{ij} = radiative plus dielectronic recombination

β_{ij} = photoionization and stimulated recombination

γ_{ij} = collisional ionization

δ_{ij} = collisional recombination.

In the escape probability formalism, the stimulated absorption and emission rates are written in terms of the coupling coefficients, so that:

$$n_j^a B_{ji}\bar{J}_{ij} - n_i^a B_{ij}\bar{J}_{ij} = \begin{cases} -A_{ji}\sum_{e=1}^{N_D} n_j^e Q_{ji}^{ea}, & (i < j) \\ \\ A_{ij}\sum_{e=1}^{N_D} n_i^e Q_{ij}^{ea}, & (i > j). \end{cases} \tag{22}$$

All terms excluding photoexcitation and photoionization (and their stimulated inverse processes) depend on <u>local</u> quantities such as the rate coefficients and electron densities. These are evaluated "exactly" for each spatial zone. However, in evaluating the photoexcitation and photoionization terms, approximations are introduced because the escape probability integrals are computed assuming a spatially uniform emission and absorption profiles.

This assumption is of course not valid when temperature and density gradients exist in the plasma.

Dunston and Davis (1981) use a model in which the escape probability integrals are evaluated using properties of the emitting zone. They estimate that this approach may introduce errors of as much as a factor of 2 for most laboratory plasma conditions, with typical errors being less than this. They argue that this simple approach leads to an acceptable representation of radiative transfer in nonhomogeneous laboratory plasmas.

We plan to implement the same approach as Dunston and Davis in our radiative transfer model, and benchmark the results against ONEDANT calculations. If the accuracy of this approach is shown to be reasonable, we will continue using this method. However, if the errors are found to be unacceptably high, we intend to explore alternatives to this relatively simple model.

3. Examination of Angle-Averaging Method in Radiation Transport

3.1. Introduction

In this section we examine two methods by which the angle-averaged radiation escape probability method developed by Apruzese (1980) can be improved. The first method is based on the Dirac chord method which will be used for the establishment of a criterion for the definition of a "mean diffusivity angle". The method can be applied to planar as well as curvilinear geometries. The second method is based on the integral representation of the transport equation through the use of first-flight kernels. A brief comparison is made between the radiation transport problem under consideration and the steady-state collision probability (SSCP) method employed in reactor physics.

3.2. The Dirac Chord Length Method

The Dirac chord length method was developed by Dirac (1943) to assist in the calculation of particle escape probabilities for solids of arbitrary shape and uniform density. Though the application of the method is not restricted to solids of a specified shape, the Dirac chord method has usually been applied to solids having nonreentrant surfaces and isotropically emitting sources. Following the analysis of Case et al. (1953), the escape probability for uniformly distributed and isotropically emitting sources within a convex body can be computed from the expression

$$P_o = \frac{\ell}{R_{Av}} \int_{R_{min}}^{R_{max}} \left(1 - e^{-R/\ell}\right) \phi(R)\, dR \tag{23}$$

where R_{Av} is the average chord length, $\phi(R)$ the chord length distribution function, ℓ the mean free path of the particles in the medium and R_{min} and R_{max} are the minimum and maximum chords within the solid. The Dirac chord method provides a means of computing the chord length distribution function $\phi(R)$ and the average chord length R_{Av} for a given solid. Once these quantities have been computed, the escape probability is obtained by performing the integration indicated in Eq. 23. A tabulation of results for bodies having special shapes (slab, sphere, cylinder, hemisphere, etc.) can be found in Case et al. (1953). Lewis (1967) generalized the Dirac chord method to include problems having anisotropically emitting sources. However, the sources are still uniformly distributed throughout the solid.

From the above brief introduction, one notes that the problem of computing the particle escape probability has been reduced to the geometrical problem of finding $\phi(R)$ and R_{Av} and performing the integration over the maximum and minimum chords of the body under consideration. Additionally, one notes that the Dirac chord method in its traditional application is restricted to solids having a uniform density and that the source region is distributed throughout the solid. However, the radiation transport problems under consideration for our application have heterogeneous density and nonuniform source distributions throughout the geometrical domain of interest. Hence an exact calculation of escape probabilities for these problems using the Dirac chord method does not seem feasible. However, the relevance of the Dirac chord method to the angle-averaged radiation escape probability method proposed by Apruzese (1981) requires further investigation.

The method proposed by Apruzese (1981) uses a mean diffusivity angle along which the optical pathlength of the particles emitted is computed. Presently the only criterion used for choosing one mean diffusivity angle over another is by comparison with exact numerical results. However, it would be preferable to have a well defined criterion for the initial choice of a mean diffusivity angle. Is the mean diffusivity angle in any way related to the geometrical shape of the body under consideration? If we assume that this is the case, then the Dirac chord length method can provide a criterion for the selection of a mean diffusivity angle.

To demonstrate this we examine the radiation transport problem in planar geometry. Figure 6 depicts the geometry. The average chord length of a slab of thickness a is (Case et al., 1953);

$$R_{Av} = 2a. \tag{24}$$

The cosine of the angle μ corresponding to this average chord we denote as $\bar{\mu}$ and is given by

$$\bar{\mu} = \frac{a}{R_{Av}} = 0.50. \tag{25}$$

Apruzese (1981, 1985) has indicated that the best results are obtained using a cosine of the mean diffusivity angle of 0.51 for Doppler, Lorentz and Voigt profiles. Thus we note, to zero'th order (not including any line profile or opacity weighting), the cosine of the mean diffusivity angle can be obtained using the average chord length, R_{Av}, as computed from the Dirac chord method.

The emitted radiation is transported along one angular direction in the angle-averaged radiation escape probability method. However, because the emitted radiation travels through heterogeneous regions of differing densities and opacities, an improved calculation of particle attenuation would be obtained by going to a multiangle transport scheme and to transport the radiation within angular bins or sectors. The Dirac chord method can be used to compute the average chord length within each angular sector. Once this has been computed, a mean diffusivity angle for each angular sector can be obtained.

To illustrate this procedure, we consider the transport of radiation within two angular sectors in planar geometry. The angular sectors have boundaries $0.5 < \mu < 1.0$ and $0.0 < \mu < 0.5$. As stated above, the objective is to compute the cosine of the mean diffusivity angle for each angle sector which are denoted as $\bar{\mu_1}$ and $\bar{\mu_2}$. For this computation the chord length distribution function $\phi(R)$ is required. The chord length distribution function for the slab depicted in Figure 6 is (Case et al., 1953);

$$\phi(R)\, dR = 2a^2 \frac{dR}{R}. \tag{26}$$

The average chord length within the i'th angular sector is computed from the expression

$$\bar{R}_{Av,i} = \frac{\int_{R_{min}}^{R_{max}} R\, \phi(R)\, dR}{\int_{R_{min}}^{R_{max}} \phi(R)\, dR}, \tag{27}$$

where R_{min} and R_{max} are the maximum and the minimum chord lengths within the angular sector. They are obtained from the relationship

$$R_i = \frac{a}{\mu_i}, \tag{28}$$

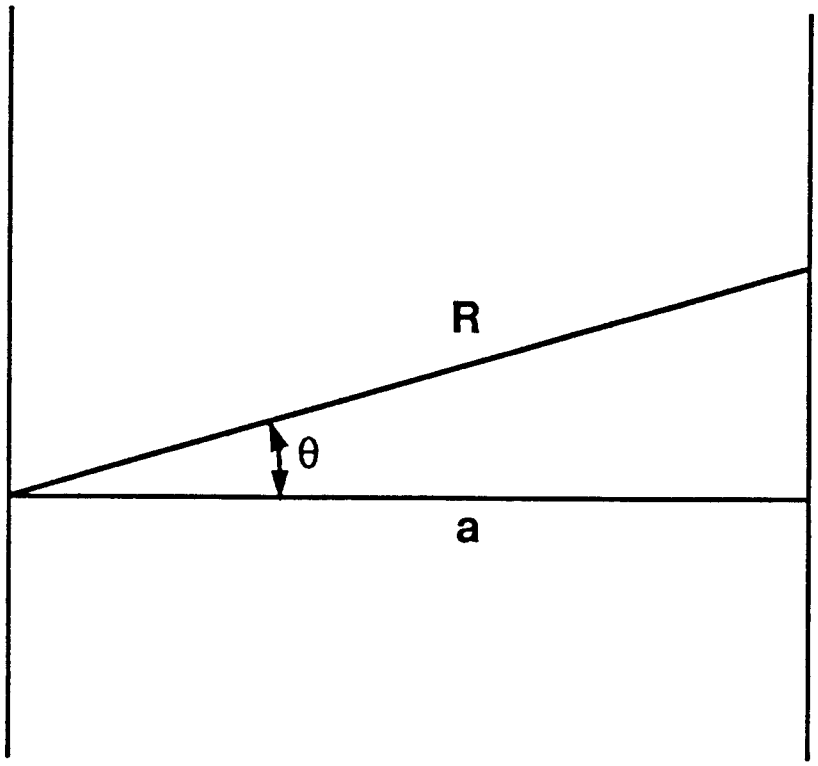

Figure 6. Planar geometry transport configuration. Depicted is a slab of thickness a.

where μ_i is the i'th angular sector boundary. Computing the minimum and maximum chords for each angular sector and completing the integrations indicated in Eq. (27), the cosine of the mean diffusivity angles along which the optical pathlengths are to be computed are (using the relationship indicated in Eq. (25) $\bar{\mu_1} = 0.75$ and $\bar{\mu_2} = 0.25$. Again this is a zero'th order approximation as the average chord lengths have not been weighted over line profiles or opacities. This procedure can be extended to any number of angular sectors desired.

In curvilinear geometries, the emitted radiation is also transported along one mean diffusivity angle. By choosing one mean diffusivity angle, the emitted particles miss inner and outer material zones (in a heterogeneous density configuration) which are not intersected by the chord described by the mean diffusivity angle. This forces a portion of the source particles to traverse a different optical pathlength than they would normally travel. Additionally, the mean diffusivity angle chosen is the same as that for the planar case. This is a good approximation for material zones and radiation emitted at large radii but a poor approximation for radiation emitted within inner small radii zones. The calculation in the curvilinear geometries can by improved by considering a multiangle scheme in combination with the average chord length as computed using the Dirac chord method.

To illustrate the multiangle transport scheme in curvilinear geometries, we consider the transport of radiation in a heterogeneous spherical shell configuration. Figure 7 depicts the geometry under consideration. We are interested in obtaining the radiation impinging upon the outer spherical shell at radius $r = a$ which can be obtained by considering the radiation impinging upon the point A. The most straightforward division of the angular range into sectors is to draw lines tangent to the radii zone boundaries as depicted in Fig. 7. The procedure illustrated in planar geometry can now be used in spherical geometry by properly defining the angular sector boundaries. The cosine of the angle of a ray tangent to an inner shell is

$$\mu_i = \sqrt{1 - \left(\frac{r_i}{a}\right)^2}, \tag{29}$$

where r_i is the radius of the i'th inner shell. Once having computed the angular sector boundaries, the length of the chords along the angular sectors, R_{min} and R_{max}, which are required for the calculation of the average chord length within the angular sector, can be computed from

$$R_i = \mu_i \times 2a. \tag{30}$$

The chord length distribution function for a sphere of radius a is (Case et al. 1953)

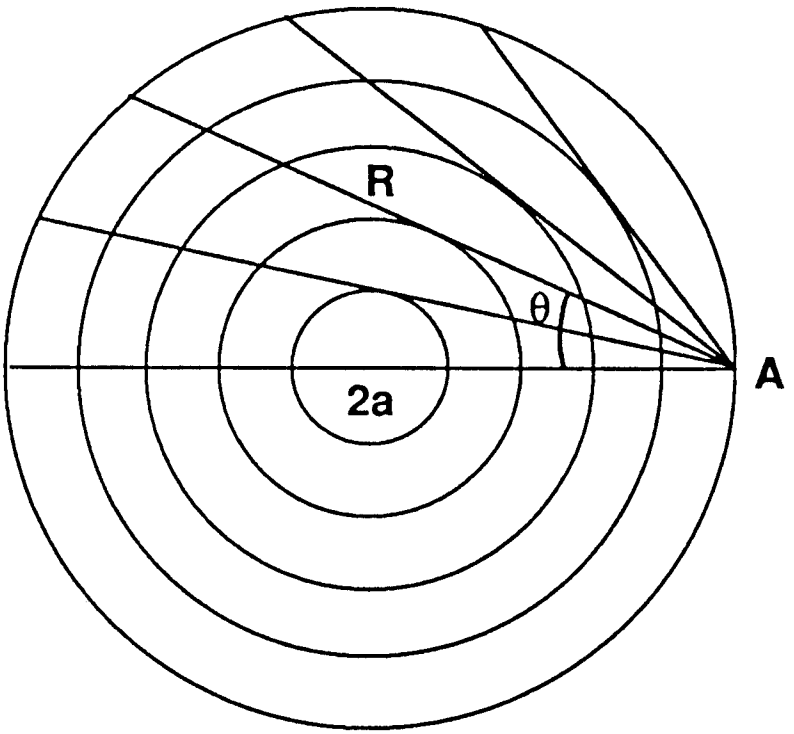

Figure 7. Heterogeneous spherical shell transport configuration. Depicted is a sphere of radius a.

$$\phi(R)\, dR = \frac{R}{2a^2}\, dR. \tag{31}$$

Once the average chord length has been determined from the integrations indicated in Eq. (27), the i'th cosine of the mean diffusivity angle along which the optical pathlength is computed can be obtained from the relationship

$$\bar{\mu}_i = \frac{R_{Av,i}}{2a}. \tag{32}$$

We note that with the straightforward division of the angular range, chords defined by the cosines of the mean diffusivity angles will intersect all intervening spherical regions; thus the calculation of the optical pathlength traversed by the source particles has been improved which improves the overall calculation.

In the above illustration, the radiation was transported to a point A on the surface of the spherical body. A modification to the chord length distribution function, $\phi(R)$, must be made to consider radiation transported to a point r within the spherical body. A similar procedure can be developed for cylindrical geometry.

We expect that the multiangle transport scheme outlined above will improve the photoionization rates within the medium and the line radiation flux escaping from the surface of a body in curvilinear as well as planar geometry. However, this is only one aspect of the angle-averaged radiation escape probability method. Additionally, the escape probabilities are frequency-averaged over the line profile, ϕ_ν. Hence to improve upon that aspect of the problem, a scheme should be devised to incorporate line profile averaging and/or opacity weighting of the opacities in the various regions. Another alternate approach would be to consider a multifrequency approximation.

3.3. Use of the Radiation Transfer Equation

In the previous section, we have considered a multiangle radiation transport scheme using the Dirac chord method to improve the angle-averaged radiation escape probability method. Another approach would be to solve the radiation transfer equation itself. This approach is discussed below.

The form of the radiation transfer equation considered is due to Mihalas (1984) and is given in the steady state approximation as

$$\left(\hat{\Omega} \cdot \vec{\nabla} + \chi(\vec{r}, \hat{\Omega}, \nu)\right) I(\vec{r}, \hat{\Omega}, \nu) = \eta(\vec{r}, \hat{\Omega}, \nu), \tag{33}$$

where η and χ are called the emissivity and extinction coefficients. By just considering absorption and emission, the solution to the above equation is reduced to determining what is known in transport theory as the first-flight distribution of particles for each frequency group. The first-flight distribution can readily be obtained by converting the above equation into an integral equation from which the first-flight transport kernels are obtained. The SSCP method based on the first-flight kernels has been successfully used in reactor physics for the calculation of the flux distribution in reactor lattices, the calculation of disadvantage factors in unit-cell computations, and in resonance integral calculations. Various computer programs have been written which utilize the SSCP method (Tsuchihashi 1979, 1983, 1986; Kier and Robba 1967; Kier 1965; Kavenoky 1969). Hence an integral transport formulation of the radiation transfer within the plasma would parallel the SSCP developments. We note that the only difference in the formulation of the method for radiation transport lies with the use of a scattering matrix. Since we are only considering the first-flight distribution, a scattering matrix is not required.

Above we have just considered the treatment of the spatial domain. The frequency domain can be treated as discussed in the previous section; by line profile and/or opacity weighting of the opacities or by a multifrequency approximation. We expect that both the first-flight approach and an improved frequency domain treatment will improve the angle-averaged radiation escape probability method.

3.4. Summary

Two methods by which the angle-averaged radiation escape probability method developed by Apruzese (1980) can be improved were briefly examined. The first method is based upon the Dirac chord method which is used to compute the average chord length R_{Av} within angular sectors of a convex body for a multiangle treatment of the angular range. The average chord lengths are then used to define mean diffusivity angles within the angular sectors along which the optical pathlengths of the emitted radiation is computed. The second method examined is based upon the integral form of the transport equation through the use of the first-flight kernels. The development of the method would parallel the SSCP method used in reactor physics except for the use of a scattering matrix. Both methods are expected to yield improved results over those obtained using the angle-averaged radiation escape probability scheme particularly if a improved scheme for the frequency domain can be devised.

We have explored the possibility of using the Dirac chord method to improve the angle-averaged radiation escape probability method in the radiation transfer code. It was shown that the Dirac chord method can be used to define a mean diffusivity angle which is required for the computation of the optical pathlength traversed by the emitted radiation. The Dirac chord method can also be used to define mean diffusivity angles for a

multiangle radiation transport algorithm. The multiangle transport algorithm could be incorporated into the existing radiation transfer code. However, this approach would require a non-trivial computational effort (multiangle versus one angle). Given the fact that there are other approximations are used in the current model, such as using frequency-averaged escape probabilities, this may not be the best way to proceed. We feel a better way to proceed in this area is to develop a separate, more exact, radiation transfer model based on a multifrequency approach for the frequency domain and a multiangle approach using the Dirac chord method or an integral transport theory approach using the first-flight kernels of radiation transport for the spatial-angular domain. This model would be used to perform more accurate radiation transport calculations which could be used to benchmark the escape probability code, as well as more readily and accurately assess the importance of effects such as velocity gradients in an expanding plasma and temperature and density gradients. Additionally, this approach would allow for greater frequency-coupling between different atomic transitions, thus enabling the code to reliably model a wider range of spectral regimes.

4. TWODANT Benchmark Calculations

We have performed a series of benchmark calculations to assess the accuracy of the escape probability radiative transfer code. The primary purpose of the calculations was to check the reliability of the angle- and frequency-averaging techniques employed in the escape probability model. To do this, we performed radiation transport calculations with the ONEDANT code (Alcouffe et al. 1984) using input data supplied by RTEP calculations. The output from the two calculations were then compared to determine the magnitude of the errors due to the angle- and frequency-averaging models. Because both codes used the same spatial grids (i.e., the grid of RTEP was the same as the coarse grid for TWODANT), particle densities, absorption cross sections, and emission (source) terms, the differences in the results are expected to arise from the angle- and frequency-averaging approximations in the escape probability model.

4.1. Overview of Angle and Frequency-Averaging Techniques

We first briefly review the angle- and frequency averaging methods in our escape probability model. The photoexcitation rate corrected for stimulated emission is given by (Eq. (15) of Paper I):

$$(N_\ell B_{\ell u} - N_u B_{u\ell})\bar{J} = \sum_{e=1}^{N_D} N_u^e A_{u\ell} Q^{ea}, \tag{34}$$

where N_u and N_ℓ are the populations of the upper and lower states, respectively, $B_{\ell u}$ and $B_{u\ell}$ are the Einstein absorption and induced-emission transition probabilities, and $A_{u\ell}$ is the spontaneous emission rate. $\bar{J}$ is the mean intensity averaged over the line profile ϕ_ν:

$$\bar{J}(r) \equiv \int_0^\infty d\nu \phi_\nu(r) \frac{1}{2} \int_{-1}^{1} d\mu I_\nu(r,\mu), \tag{35}$$

where r is the position in the plasma, $\mu \equiv \cos^{-1}\theta$, θ is the angle between the propagation direction of the photon and the normal to the surface, I_ν is the specific intensity, and the summation is over all N_D zones of the plasma. The zone-to-zone coupling coefficient Q^{ea} between the emitting zone e and absorbing zone a can be written as

$$Q^{ea} = \frac{1}{\tau_e} \int_0^{\tau_e} [P_e(\tau_B + \tau) - P_e(\tau_B + \tau_a + \tau)] d\tau, \tag{36}$$

where $P_e(\tau)$ is the probability that a photon will travel a line center optical depth τ_c before being absorbed averaged over the emission profile $\phi_E(\nu)$:

$$P_e(\tau_c) = \int_0^\infty d\nu \phi_E(\nu) e^{\tau_c \phi_\nu / \phi_{\nu_0}}. \tag{37}$$

The quantity ϕ_{ν_0} is the value of the line profile at the line center frequency ν_0. For lines, we assume that the emission and absorption profiles are identical; that is, we assume "complete redistribution". The optical depths in Eq. (36) represent those of the emitting zone (τ_e), the absorbing zone (τ_a), and the optical depth between zones e and a. The optical depths are computed along a ray defined by the "mean diffusivity angle," $\bar{\theta}(\equiv \cos^{-1}\bar{\mu})$. Apruzese (1981, 1985) found that reasonably accurate, yet very efficient, solutions for Doppler, Lorentz, and Voigt line profiles could be obtained by computing the coupling coefficients along the ray defined by $\bar{\mu} = 0.51$. The primary purpose of the present benchmark calculations is to test the accuracy of these angle- and frequency-averaging methods.

The method for computing the photoionization rate (bound-free absorptions) is similar to the bound-bound case. The photoionization rate is given by:

$$\sum_{e=1}^{N_D} N_u^e \, n_e^e \, \alpha_{rr}^e \, Q^{ea}, \tag{38}$$

where N_u^e is the number of particles in zone e in upper state u (that is, the ground state of the next higher ionization stage), n_e^e is the electron density of zone e, and α_{rr}^e is the radiative

recombination rate in zone e. The coupling coefficients are again evaluated using optical depths computed along $\bar{\mu} = 0.51$. Using the same mean diffusivity angle $\bar{\mu}$ for all transitions improves the computational efficiency. In addition, comparisons with TWODANT results indicate that $\bar{\mu} = 0.51$ provides reasonably good accuracy for both bound-bound and bound-free transitions (see below).

4.2. Overview of TWODANT Calculations

The two-dimensional discrete-ordinates diffusion-accelerated transport code system TWODANT was used to perform the 1-D photon transport calculations for the benchmark comparison with the RTEP code. The form of the radiative transfer equation solved is given in the steady state approximation as:

$$\hat{\Omega} \cdot \bar{\nabla} I(\bar{r}, \hat{\Omega}, \nu) + \chi(\bar{r}, \hat{\Omega}, \nu) I(\bar{r}, \hat{\Omega}, \nu) = \eta(\bar{r}, \hat{\Omega}, \nu) \tag{39}$$

where η and χ are called the emissivity and extinction coefficients. The radiative transfer equation was solved using the multigroup approximation with the photon frequency domain divided up into G groups. The number of groups used in the benchmark calculations ranged from 50 to 100. The emission source term for each group g is given by:

$$S_g = \int_{\nu_g}^{\nu_{g+1}} d\nu \; \frac{4\pi\eta_\nu}{h\nu} \tag{40}$$

where ν_g and ν_{g+1} are the frequency boundaries of group g. The absorption coefficient is given by:

$$\kappa_g = \frac{1}{\Delta\nu_g} \int_{\nu_g}^{\nu_{g+1}} d\nu \kappa_\nu, \tag{41}$$

where $\Delta\nu_g = \nu_{g+1} - \nu_g$. One could also use expressions for S_g and κ_g in which the integrands are weighted by the emission profile or the Planck function. However, as the sizes of the groups ($\Delta\nu_g$) become small, the weighting method becomes irrelevant. Thus, the group-averaged emission and absorption terms defined above were sufficient for our purposes. Calculations were performed using a larger number of groups to confirm this.

The TWODANT transport code system solves the Boltzmann equation in the standard one dimensional (slab, cylindrical, spherical) and two dimensional (planar (x, y) and cylindrical (r, z) and (r, θ)) geometries using the standard multigroup formulation. Suppressing the group index g, the Boltzmann equation is given as

$$\hat{\Omega} \cdot \bar{\nabla}\psi(\bar{r}, \hat{\Omega}, E) + \sigma_t(\bar{r}, , E)\psi(\bar{r}, \hat{\Omega}, E) \tag{42}$$
$$= \int_{4\pi} d\hat{\Omega} \int_0^\infty dE' \sigma_s(E' \rightarrow E, \hat{\Omega}' \cdot \hat{\Omega})\psi(\bar{r}, \hat{\Omega}, E) + S(\bar{r}, \hat{\Omega}, E).$$

In the Boltzmann description of neutral particle/photon transport, the scattering of particles/photons is explicitly described by the scattering kernel, whereas in the radiative transfer equation the scattering of photons is contained in the emissivity and extinction coefficients. Thus to model the radiative transfer equation using the Boltzmann equation, the groupwise scattering matrix elements for the TWODANT code are set to zero. The remaining input requirements for the code are the geometry mesh, total cross sections, the absorption cross sections (extinction coefficients) and the photon sources (emissivity coefficients) which were obtained from the output of the RTEP calculations. RTEP computed position-dependent level populations, and based on these, the group- and position-dependent absorption cross sections and emission terms. The spatial grid in the RTEP calculation was used as the "coarse grid" for TWODANT. Hence, the absorption cross sections and photon sources (emission terms) were entered per frequency group per spatial coarse mesh zone. To avoid numerical instabilities due to opacities differing by orders of magnitude between neighboring cells, the criterion $(\Delta/\lambda) <\mid \mu_1 \mid$ — where Δ is the mesh spacing, λ is the photon mean free path within the mesh interval Δ, and μ_1 is the smallest cosine of the angle with respect to the outward normal in the angular quadrature integration set — was applied to the spatial fine mesh zoning of the geometry considered. This ensured positivity of the fluxes and helped mitigate numerical instabilities. The TWODANT calculations were performed on a DEC3100 workstation using an S_8 discrete-ordinates approximation.

4.3. Results

By using the same spatial grid, densities, absorption cross-sections, and emission terms, we have attempted to find those differences that occur solely due to the different transport schemes: that is, multiangle, multifrequency calculations versus angle- and frequency-averaged calculations. Two figures of merit were examined to assess the reliability of the escape probability model: (1) the position-dependent photoexcitation/photoionization rates, and (2) the frequency-dependent flux at the plasma boundary (note that the term flux in radiative transfer corresponds to the term current in neutron transport, i.e., the flow of particles/photons across a boundary).

We performed 2 sets of calculations. Six calculations each were performed for bound-bound and bound-free cases. Tables 2 and 3 summarize the parameters for those calculations.

Table 2. Bound-Bound Cases

Case No.	Geometry	No. of Zones	No. of Energy Groups	Optical Depth	Quenching Parameter P_Q	R_{outer} R_{inner}
1	Planar	80	50	10^3	10^{-4}	-
2	Cylindrical	50	50	10^3	10^{-4}	-
3	Spherical	50	50	10^3	10^{-4}	3
4	Spherical	50	50	10^3	10^{-4}	300
5	Spherical	50	100	10^3	10^{-4}	300
6	Spherical	100	50	10^3	10^{-4}	300

Table 3. Bound-Free Cases

Case No.	Geometry	No. of Zones	No. of Energy Groups	Optical Depth	$h\nu_1/kT_e$	$\bar{\mu}$
1	Planar	40	50	300	11.9	0.51
2	Cylindrical	40	50	300	11.9	0.51
3	Spherical	40	50	300	11.9	0.51
4	Spherical	40	50	0.37	2.37	0.51
5	Spherical	40	50	11	11.9	0.51
6	Spherical	40	50	300	11.9	0.70

For the bound-bound calculations, the line center optical depth was $\tau_c = 10^3$ and the "quenching parameter" P_Q, which is a measure of the photon scattering (see Paper I), was 10^{-4}. Doppler line profiles were assumed. For spherical geometry, calculations were performed for hollow shell plasmas so that we could check our results against previously published calculations (Kunasz and Hummer 1974). The ratio of the outer radius-to-inner radius was varied between 3 and 300. To ensure that 50 spatial zones and 50 energy groups were adequate, we performed calculations in which the number of each was doubled.

For the bound-free calculations, the base case was a plasma with an optical depth of 300 at the photoionization edge ($E = h\nu_1$) and a temperature such as $h\nu_1/kT_e = 11.9$. The absorption cross-section was assumed to be hydrogenic ($\kappa_\nu \propto \nu^{-3}$). In the RTEP

calculations, this corresponds to a temperature of 10 eV for the Al V $\rightarrow$ Al IV recombination edge ($h\nu_1 = 118.6$ eV). The plasma density in each case was 10^{19} cm^{-3}. We also performed calculations in which the temperature was increased (Case 10) and the optical depth was decreased (Case 11). In addition, we tried a calculation in which the mean diffusivity angle was changed from $\bar{\mu} = 0.51$ to 0.70 (Case 12).

We shall now discuss the results of each case separately. The results are shown in Figures 8 through 18. In each case, the photoexcitation/photoionization rate and the percent differences between RTEP and TWODANT are plotted as a function of zone index. The bound-bound fluxes at the boundary are plotted as a function of scaled frequency $\left(= \frac{\nu - \nu_0}{\Delta\nu_D}\right)$. The bound-free fluxes are plotted vs. $(\nu/\nu_1)^{-1}$. Thus, the photoabsorption edge is at the right ($\nu = \nu_1$). The percent differences for the fluxes are also plotted.

Case 1: Bound-bound case for a planar slab. The photoexcitation rate is greatest at the center of the slab ($\approx 10^9$ transitions/ion/s) and falls by more than an order of magnitude at the slab boundaries. There is some minor numerical noise at the right boundary of the TWODANT calculations due to some roundoff problems in setting up the grid. This does not affect our conclusions.

Throughout the slab, the RTEP photoexcitation rates are 10-15% higher than the TWODANT rates. The RTEP fluxes are ~10-15% low near the center of the line ($\mid \nu - \nu_0 \mid < 2\Delta\nu_D$). (For a discussion of the physics behind the profile inversion, see Avrett and Hummer (1965).) In the wings of the line, the TWODANT flux decreases faster than the RTEP flux. The relative error continues to rise in the wings, but the flux in the wings is very low.

The higher photoexcitation rates and lower flux near the line core for RTEP indicate that the code slightly overestimates the degree of scattering in the plasma. We consider errors of this magnitude to be perfectly acceptable.

Case 2: Bound-bound case for a cylindrical plasma. The photoexcitation rate is greatest along the axis of the cylinder. RTEP again overestimates the photoexcitation rate by 10-15%. The RTEP fluxes are about 7% too low at the line center, and up to 20-25% too high in the wings.

Case 3: Bound-bound case for a hollow sphere. The ratio of the outer radius to inner radius is 3. The RTEP photoexcitation rate is 10-15% larger than TWODANT. The RTEP flux is about 10-15% lower in the line core, and about 15-20% too high in the wings.

Case 4: Bound-bound case for a hollow sphere. The ratio of the outer radius to inner radius is 300. The RTEP photoexcitation rate is 10-20% too high, and the errors in the flux are less than 20%.

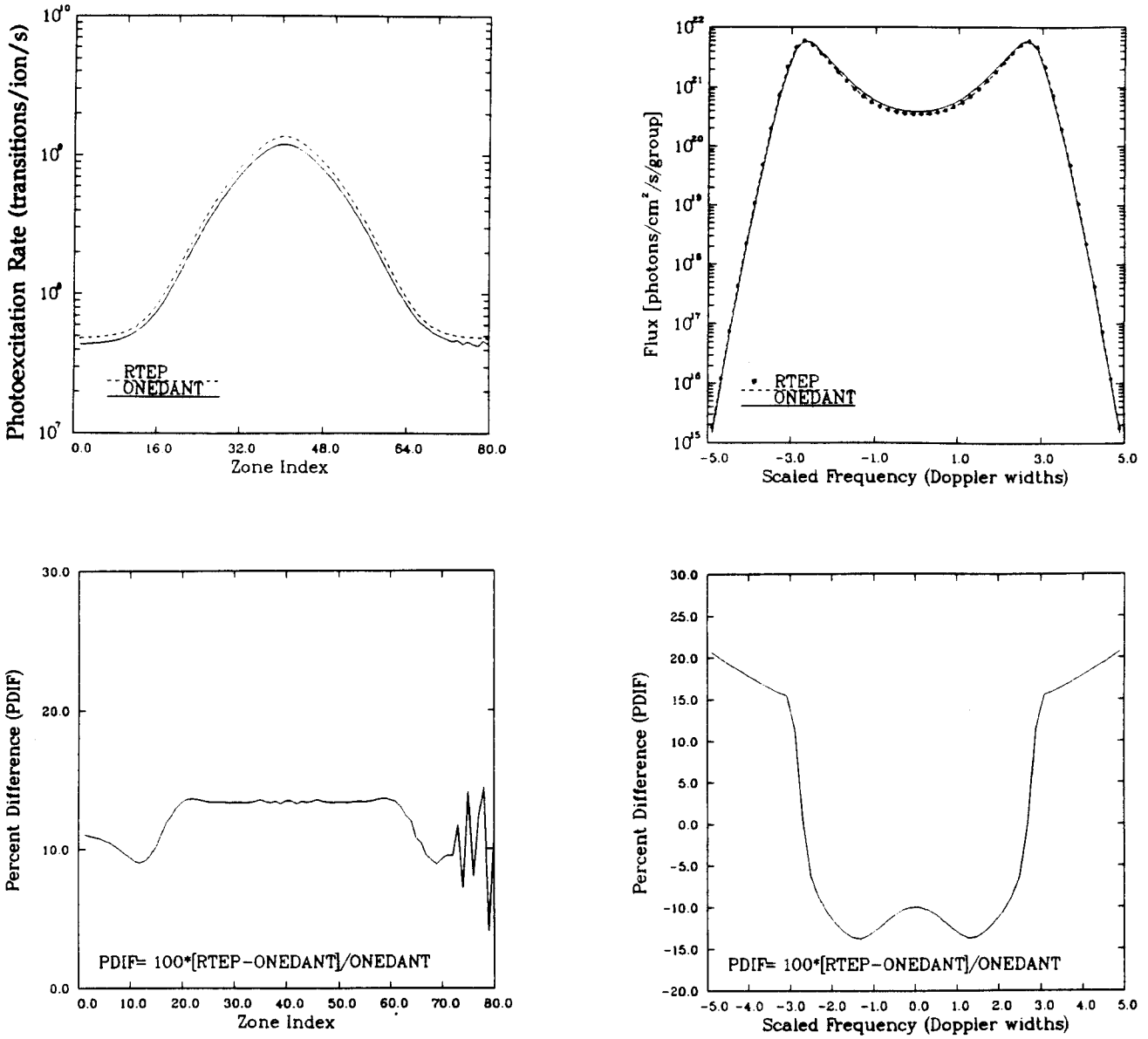

Figure 8. Bound-bound planar case with 80 zones and 50 energy groups. $\tau_0 = 10^3$ and $P_Q = 10^{-4}$ (Case 1).

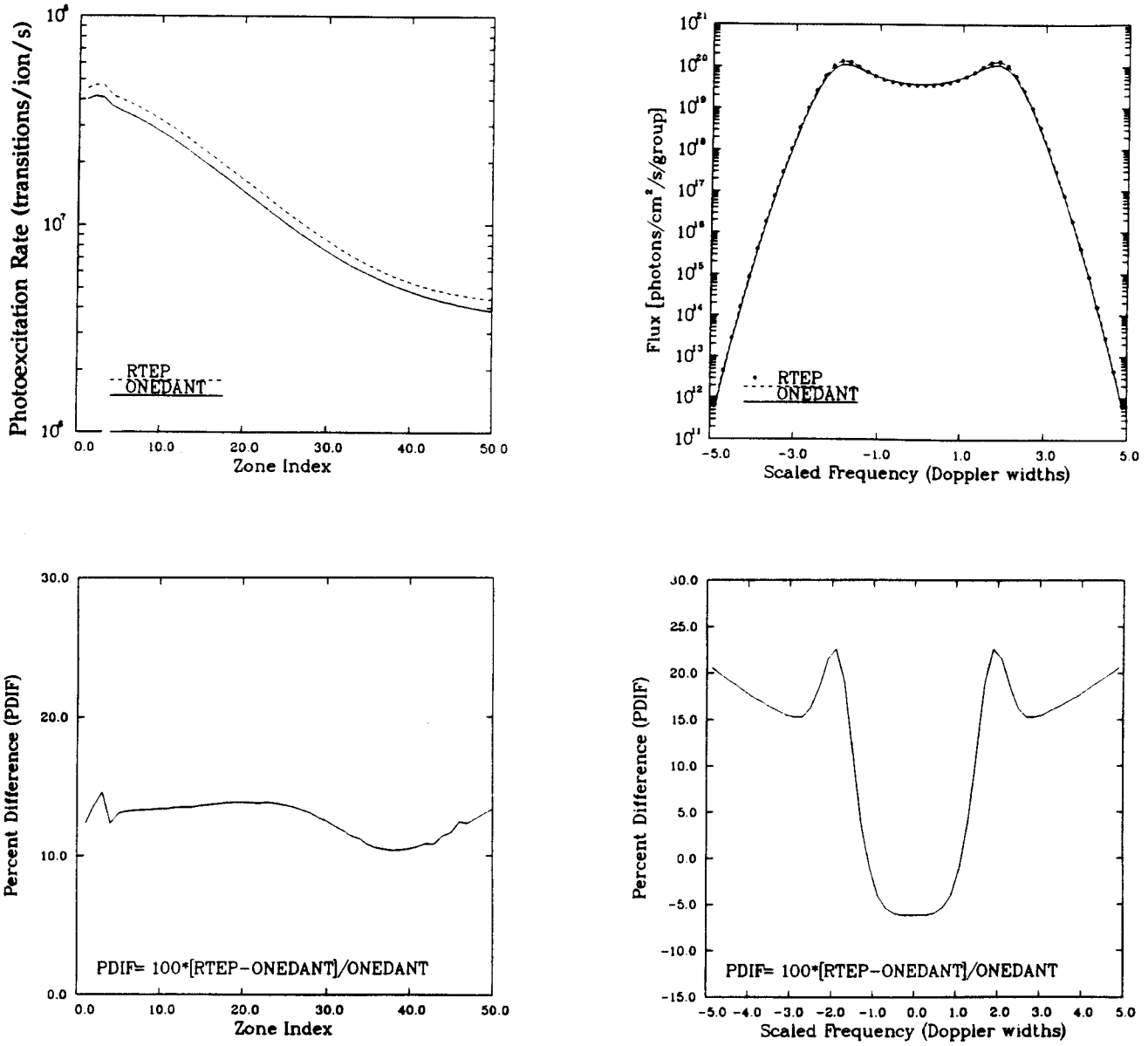

Figure 9. Bound-bound cylindrical case with 50 zones and 50 energy groups. $\tau_0 = 10^3$ and $P_Q = 10^{-4}$ (Case 2).

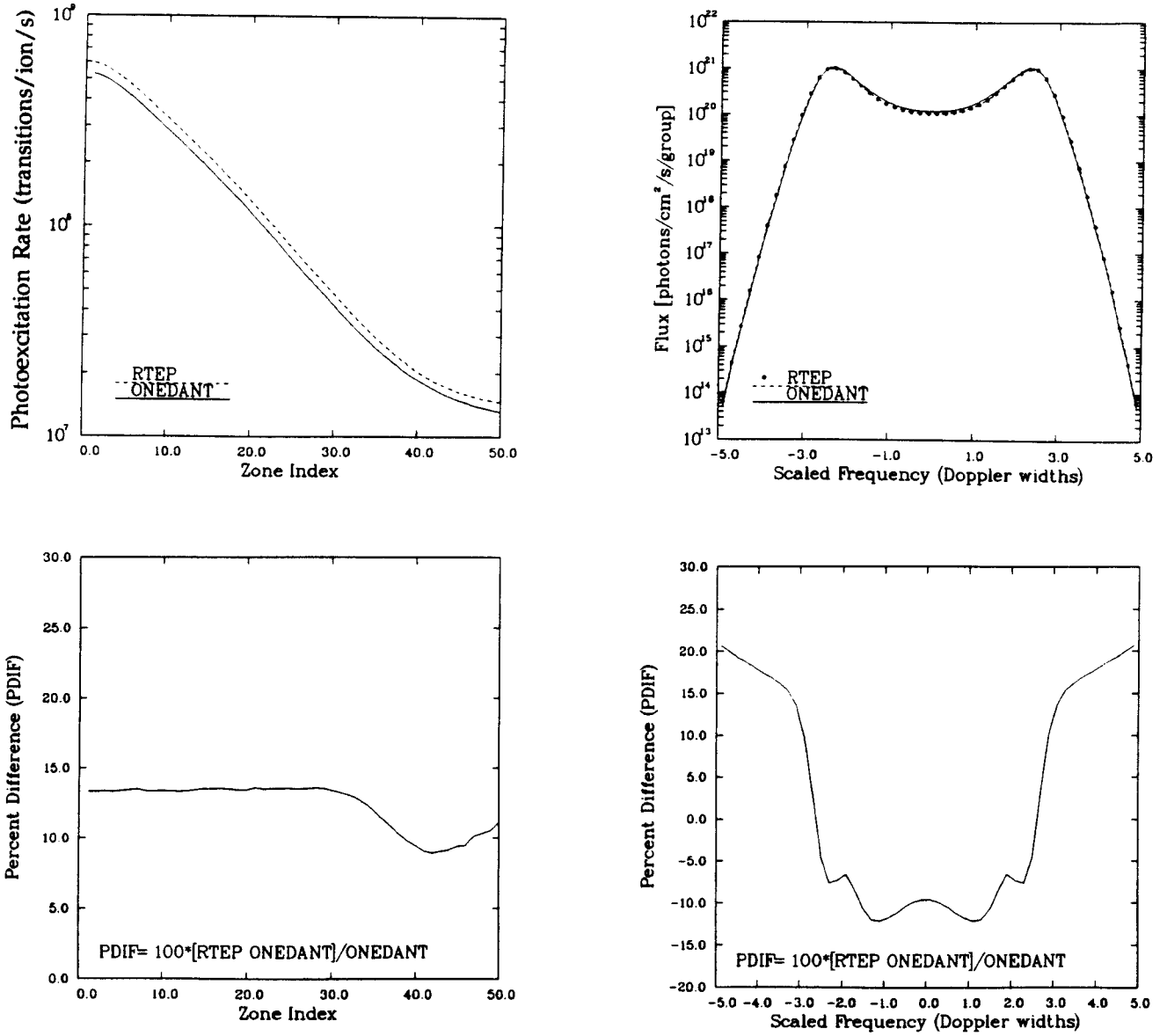

Figure 10. Bound-bound case for a hollow spherical shell with 50 zones and 50 energy groups. $\tau_0 = 10^3$ and $P_Q = 10^{-4}$. The ratio of the outer radius to the inner radius of the shell is 3 (Case 3).

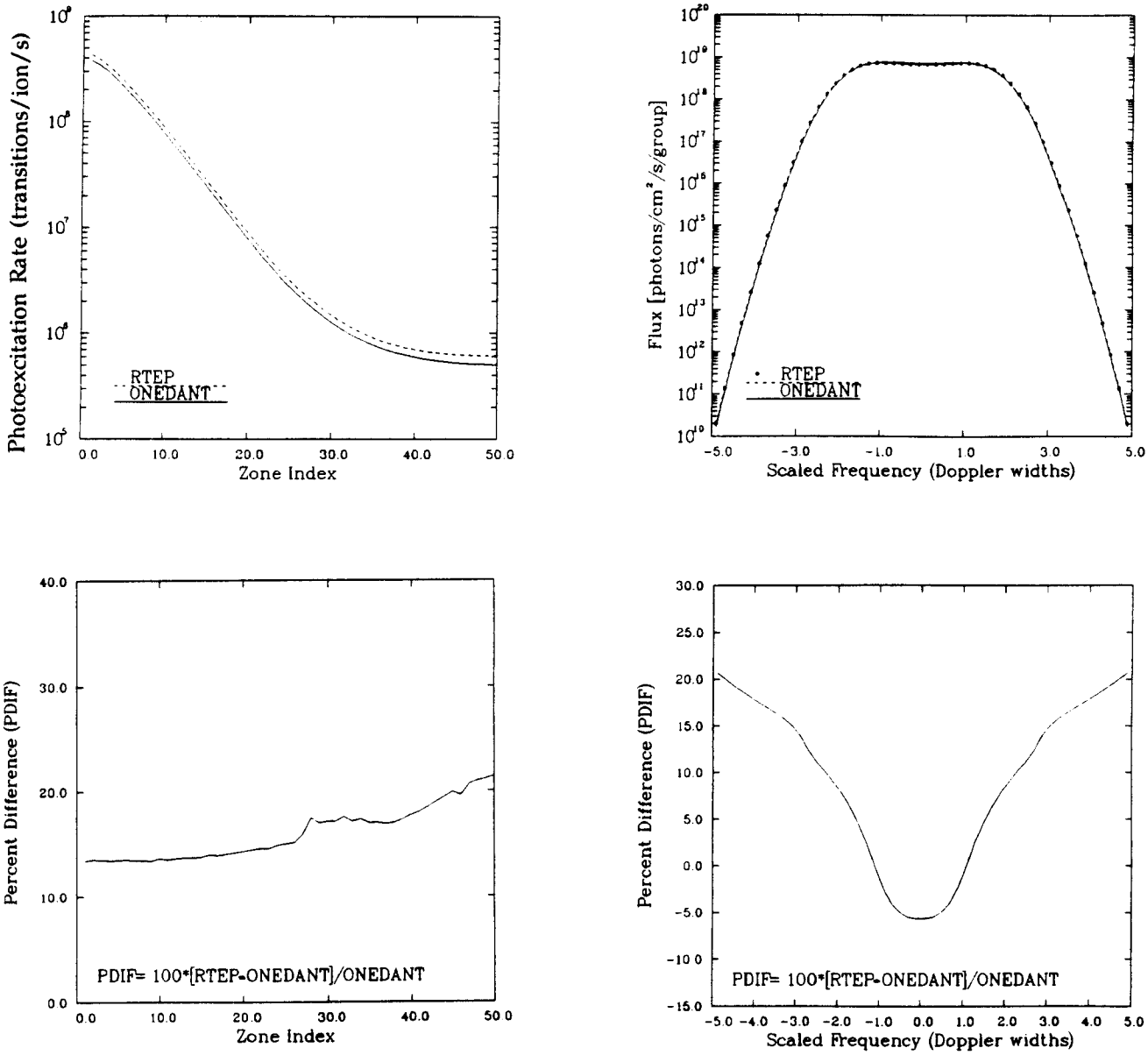

Figure 11. Bound-bound case for a hollow spherical shell with 50 zones and 50 energy groups. $\tau_0 = 10^3$ and $P_Q = 10^{-4}$. The ratio of the outer radius to the inner radius of the shell is 300 (Case 4).

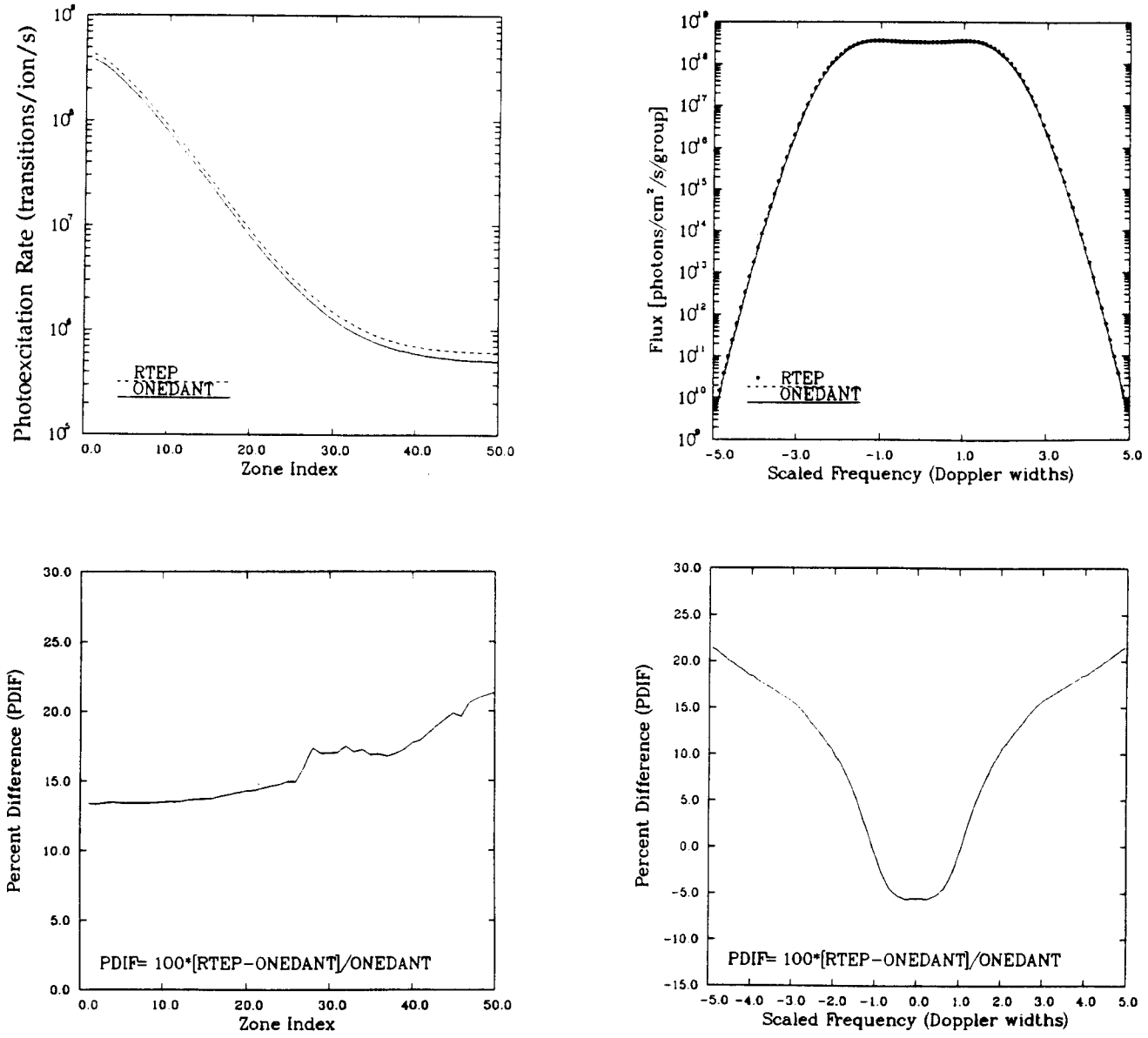

Figure 12. Bound-bound case for a hollow spherical shell with 50 zones and 100 energy groups. $\tau_0 = 10^3$ and $P_Q = 10^{-4}$. The ratio of the outer radius to the inner radius of the shell is 300 (Case 5).

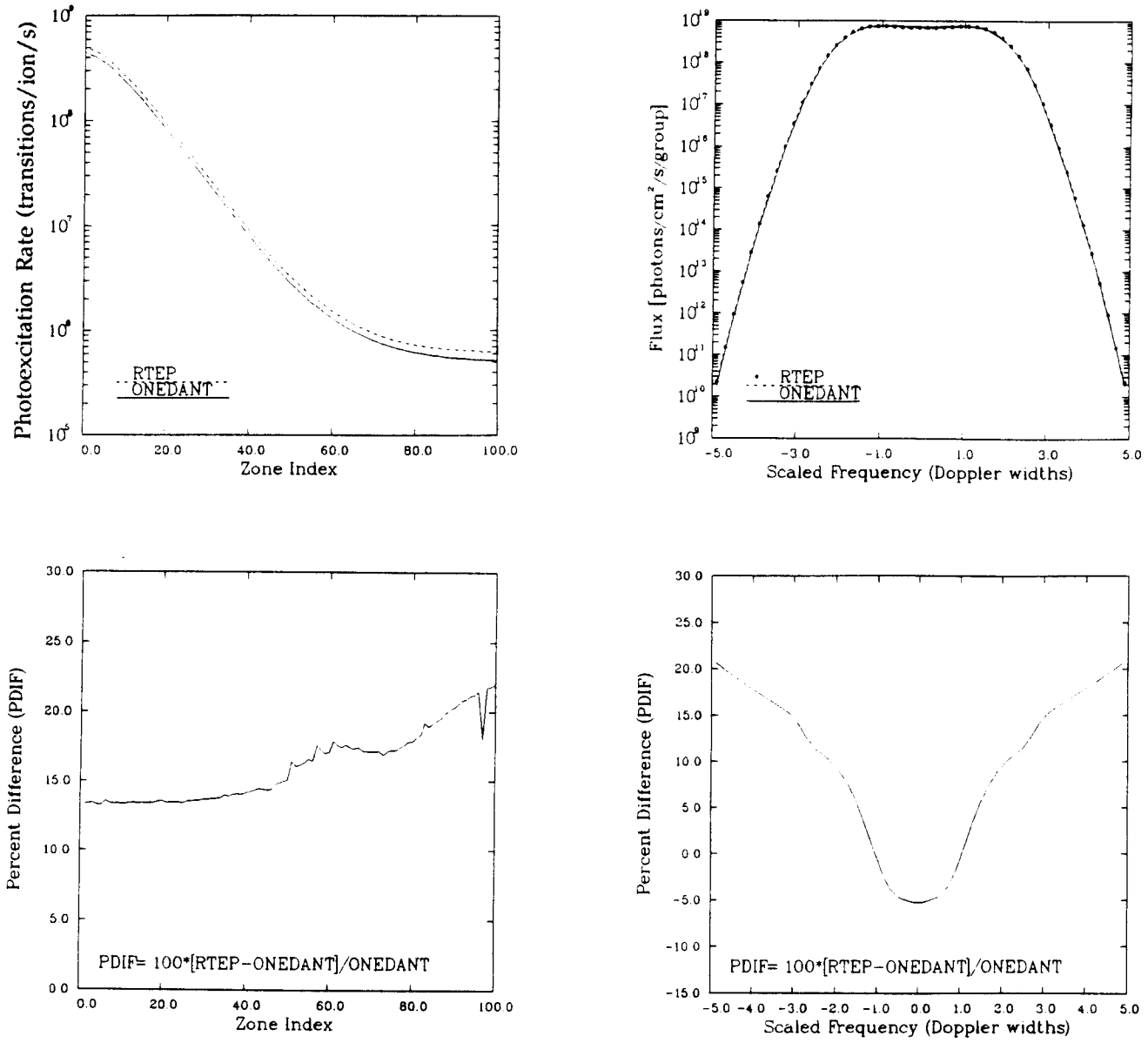

Figure 13. Bound-bound case for a hollow spherical shell with 100 zones and 50 energy groups. $\tau_0 = 10^3$ and $P_Q = 10^{-4}$. The ratio of the outer radius to the inner radius of the shell is 300 (Case 6).

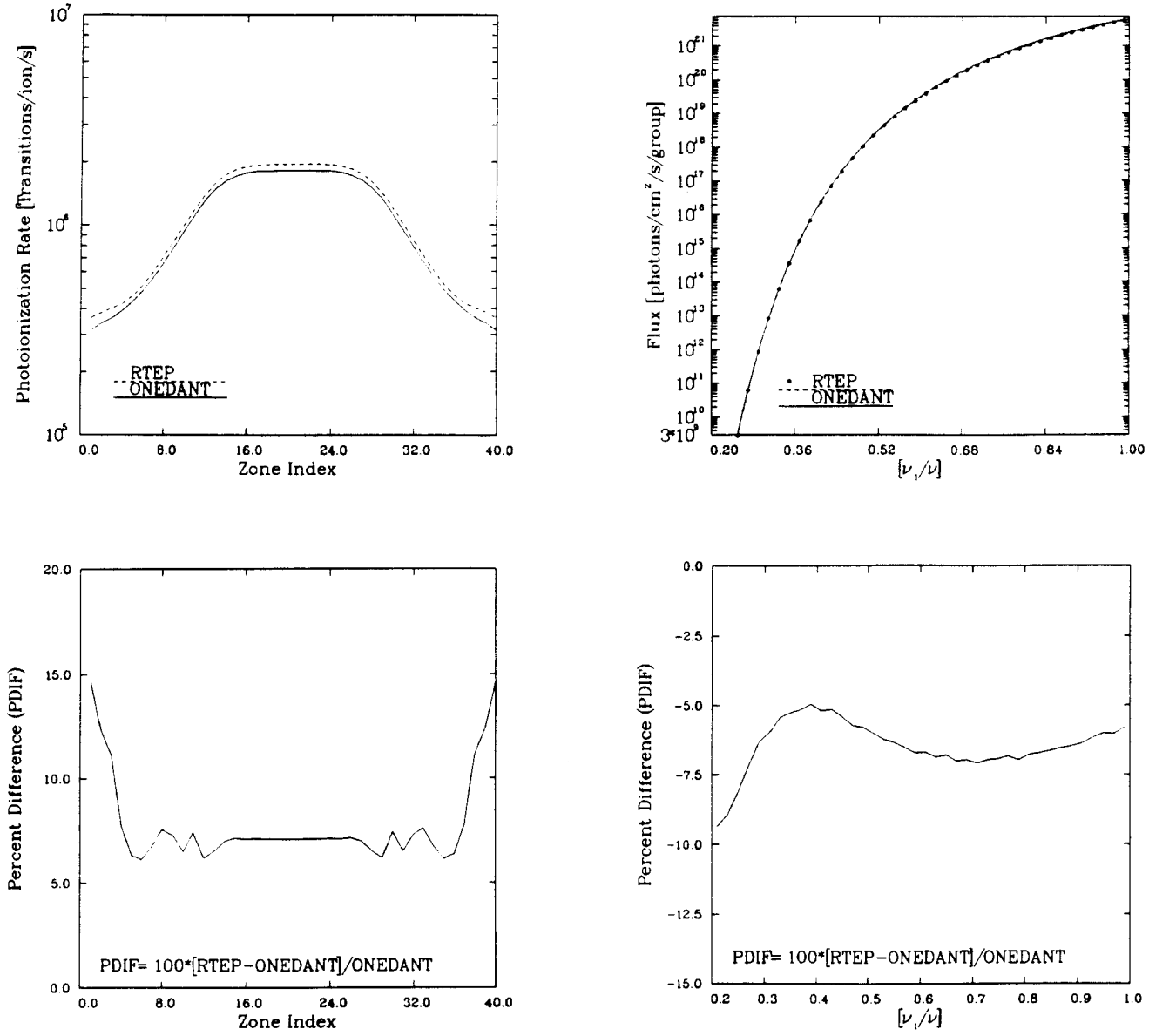

Figure 14. Bound-free planar case with 40 zones and 50 energy groups. $\tau_{edge} = 300$ and $h\nu_1/kT = 12$ (Case 7).

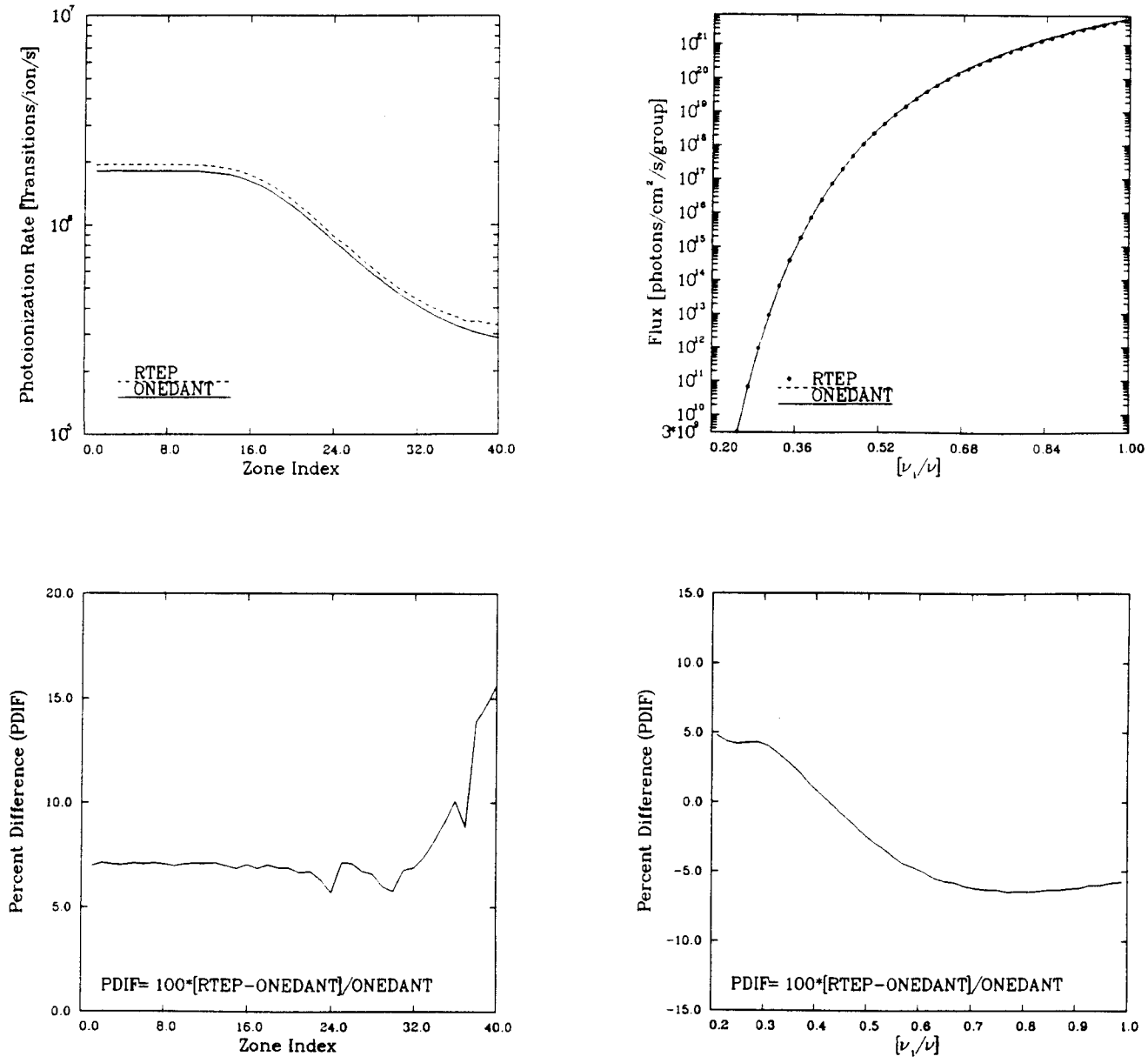

Figure 15. Bound-free cylindrical case with 40 zones and 50 energy groups. $\tau_{edge} = 300$ and $h\nu_1/kT = 12$ (Case 8).

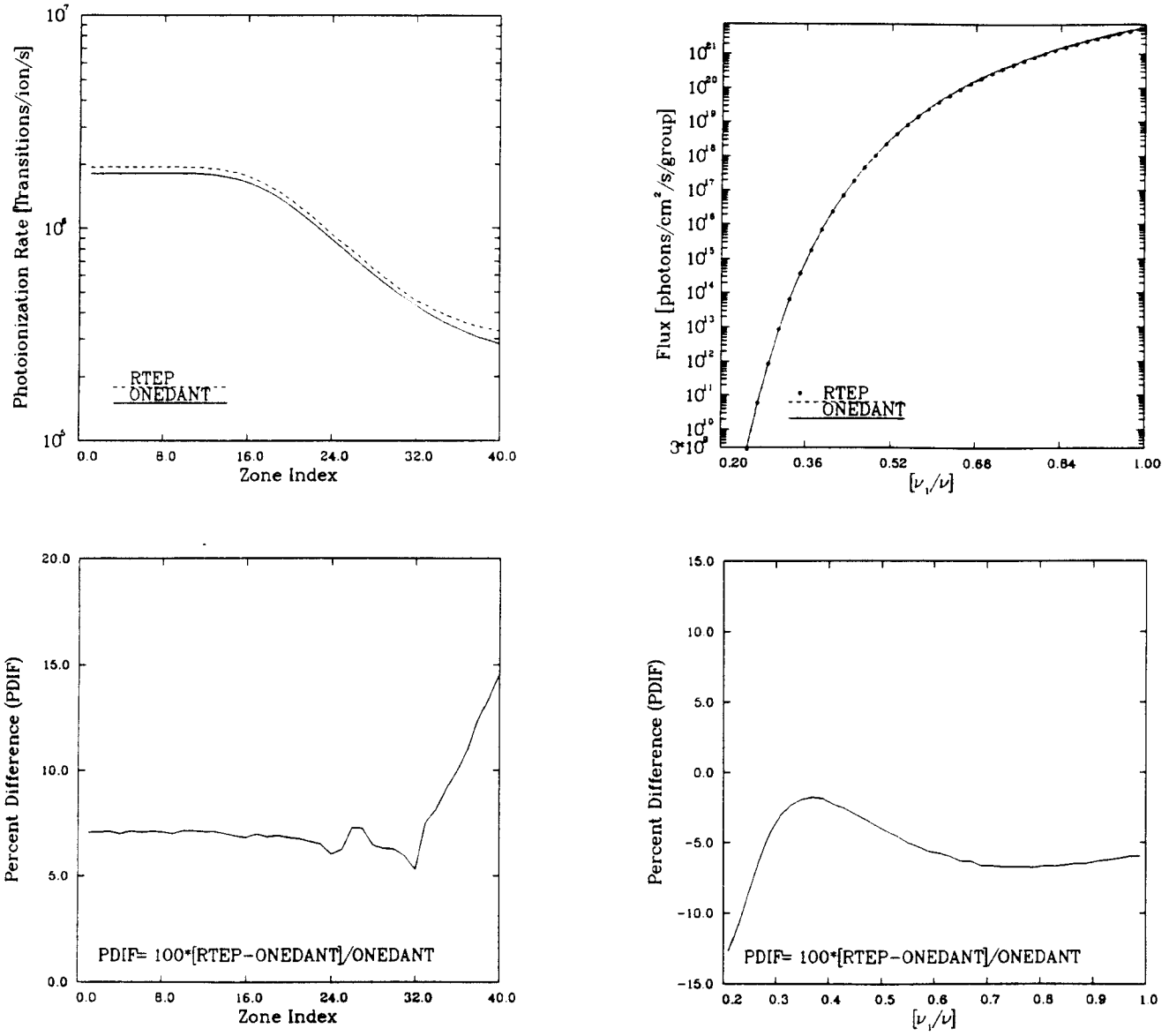

Figure 16. Bound-free case for a spherical plasma with 40 zones and 50 energy groups. $\tau_{edge} = 300$ and $h\nu_1/kT = 12$ (Case 9).

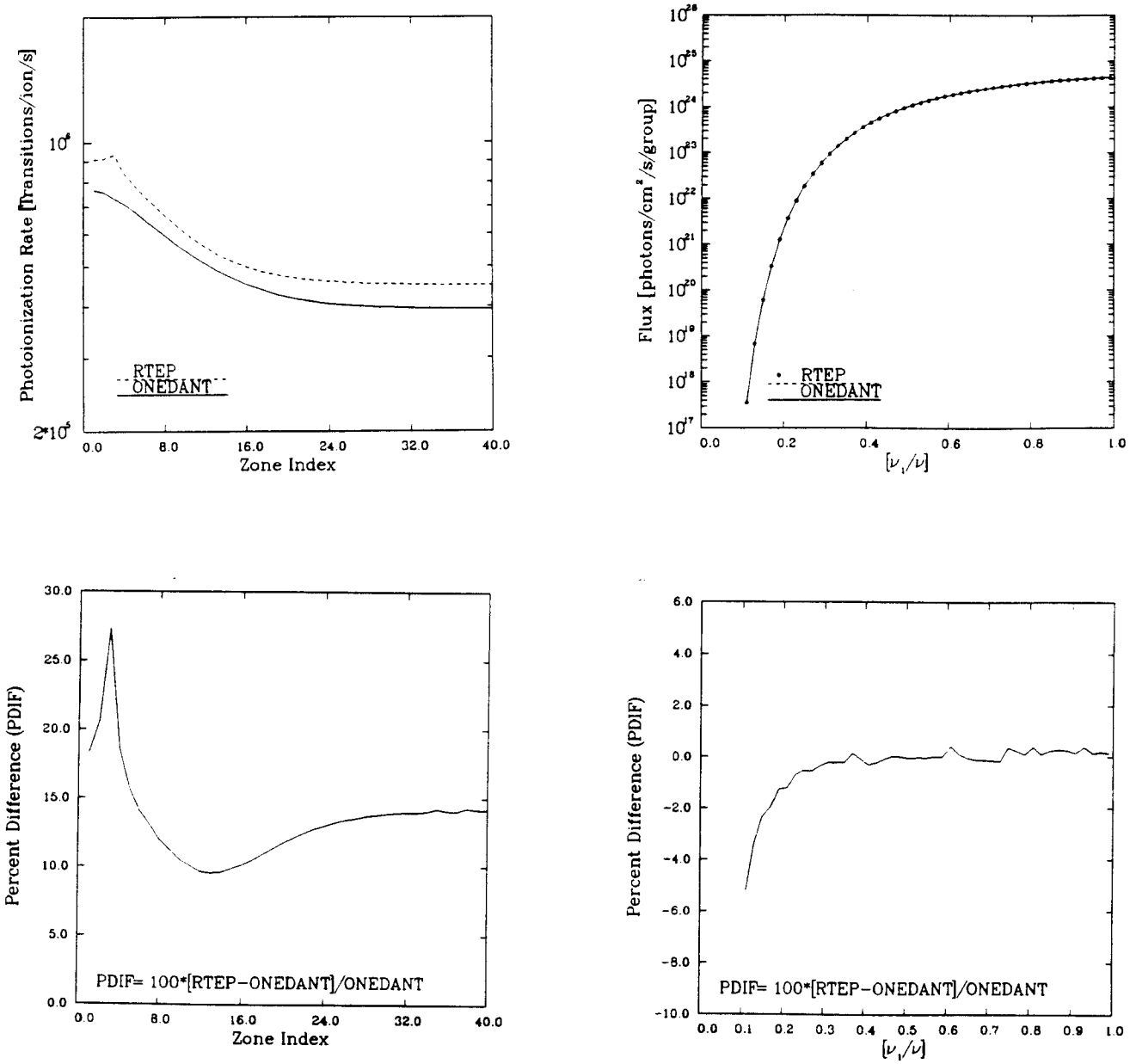

Figure 17. Bound-free case for a spherical plasma with 40 zones and 50 energy groups. $\tau_{edge} = 0.37$ and $h\nu_1/kT = 2.4$ (Case 10).

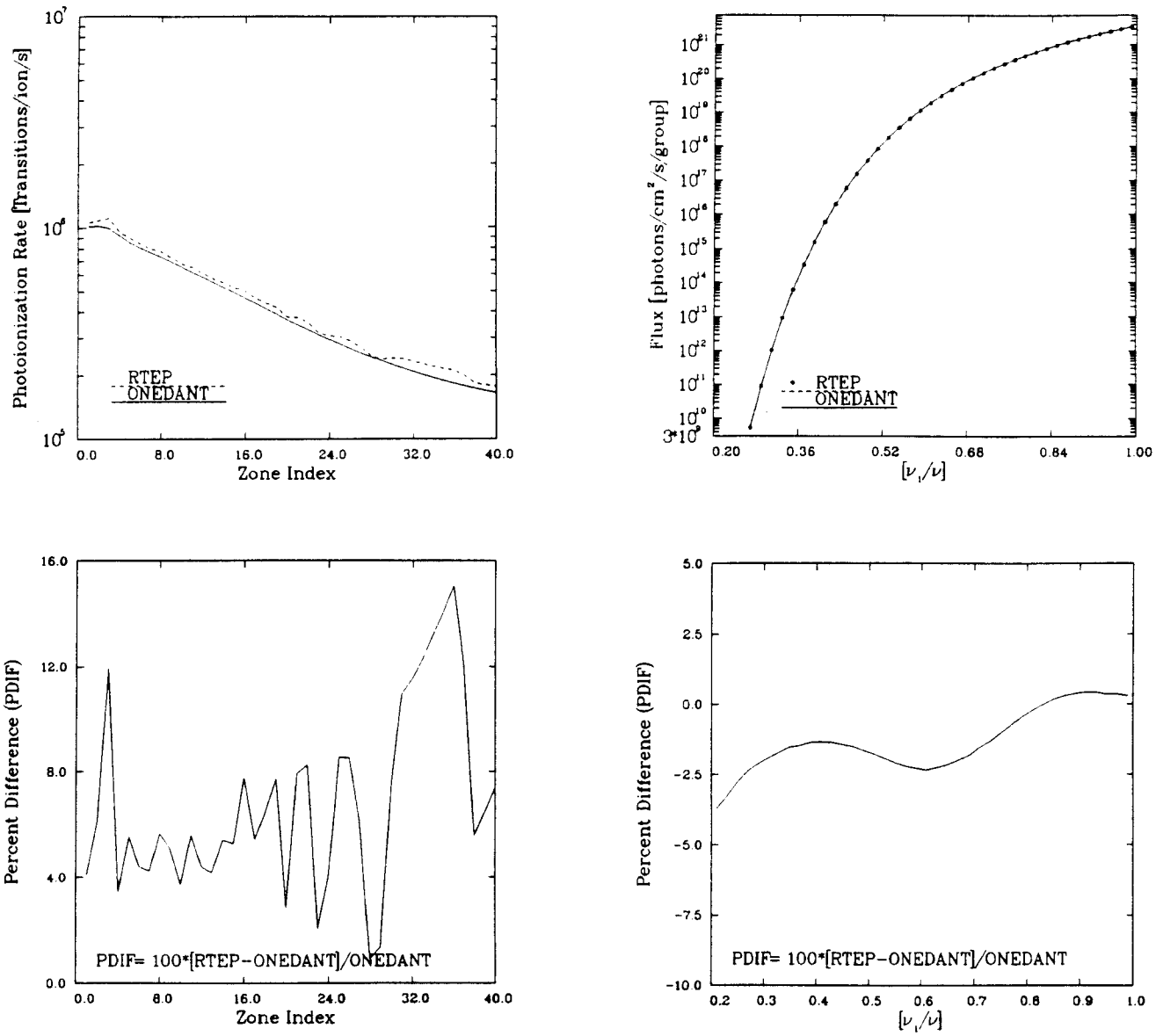

Figure 18. Bound-free case for a spherical plasma with 40 zones and 50 energy groups. $\tau_{edge} = 11$ and $h\nu_1/kT = 12$ (Case 11).

Case 5. Same as Case 4, but with the number of photon energy groups doubled. Results are very similar to Case 4.

Case 6. Same as Case 4, but with the number of spatial zones doubled. Results are again very similar to Case 4. Cases 5 and 6 show that the resolution of our spatial and frequency grids is adequate.

Case 7. Bound-free case for a planar slab. The photoionization rate at the center of the slab is about 2×10^6 transitions/ion/s. The RTEP photoionization rate is about 7% higher than TWODANT at the center of the slab and about 15% higher near the slab boundaries. At the photoionization edge ($\nu_1/\nu = 1$), the RTEP flux is about 6% lower than TWODANT. At $\nu = 5 \cdot \nu_1 (\nu_1/\nu = 0.2)$, RTEP is about 10% lower. The higher photoionization rates and lower fluxes indicate RTEP slightly overestimates the scattering for these conditions. We feel errors of this magnitude are quite acceptable.

Case 8. Bound-free case for a cylindrical plasma. The RTEP photoionization rate is 7% higher than TWODANT along the axis of symmetry, and rises to about 15% higher at the plasma boundary. The RTEP flux is 5-6% too low near the photoionization cutoff.

Case 9. Bound-free case for a spherical (non-hollow) plasma. The RTEP photoionization rate ranges from 5% to 15% higher than TWODANT. The flux is roughly 2-10% lower than TWODANT.

Case 10. Same as Case 9, but with a higher temperature (50 eV). The higher temperature decreased the optical depth to 0.37 and $h\nu_1/kT$ to 2.37. The RTEP and TWODANT fluxes are within 5% at all frequencies, but the photoionization rate error increases to about 25-30% near the center of the sphere. Qualitatively similar results were obtained by Apruzese (1981). Evidently, the angle-averaging model leads to some inaccuracies near the center of cylindrical and spherical plasmas with relatively small optical depths ($\tau < 10$).

Case 11. Same as Case 9, but for a smaller sphere, so that the optical depth was 11. The RTEP photoionization rates are about 3-15% too high, and the errors in the flux are less than 3%. There is some numerical scatter in the RTEP photoionization rates for this case. The source of this is not presently known.

Case 12. (Figure not shown) Same as Case 9, but with $\bar{\mu} = 0.70$ (instead of 0.51). Errors were considerably larger ($\gtrsim 40\%$). Based on calculations of the escape probability integrals, it was thought that having a mean diffusivity that was a function of $h\nu_1/kT$ might improve the accuracy. This idea was not supported by the calculations.

4.4. Summary of Benchmark Calculations

In all cases, we find that the errors introduced by the angle- and frequency-averaging models in RTEP are usually a couple tens of percent and always much less than a factor of 2. Given that the uncertainties in atomic data are often of this magnitude, we conclude that the present model is quite sufficient for studying spectra from laboratory plasmas.

We note, however, that there are certain situations in which frequency-averaging in particular could potentially cause significant errors. An example of this is when the transition energies of 2 lines are very close, so that their line profiles overlap considerably. In the current model, frequency-averaged escape probabilities are obtained by integrating over a single line. Obviously, if there is considerable overlap between the 2 profiles near the line cores, the level populations and emission spectra could be affected. We do not consider this to be a serious flaw in the model. Our intent is only to point out that there may be certain situations in which the accuracy of the model could be affected.

5. Atomic Physics Calculations

In this section, we present an overview of the atomic physics models that are used to provide the data base for the radiative transfer/ionization balance calculations. A much more detailed description of the models used in the atomic physics codes is currently being prepared by Wang (1991), and will be sent to KfK when completed. Here, we describe: (1) our model for the atomic level structure, (2) the models used to compute the transition rate coefficients, and (3) calculations relevant to the production of K_α satellite lines.

A schematic illustration of the transitions we consider is shown in Figure 19 for a simple 3-level atom. Every state is coupled to the ground state of the next higher ionization stage by collisional ionization, photoionization and stimulated recombination, collisional recombination, and radiative recombination. Adjacent ground states are also coupled by dielectronic recombination. The excited states of each ion are coupled to the ground state and all other excited states by collisional excitation and deexcitation, stimulated absorption (photoexcitation) and emission, and spontaneous radiative decay.

Collisional coupling is complete in our calculations. Thus we consider forbidden and spin-flip transitions as well as those which are electric dipole allowed. The interaction between bound electrons is approximated by an $L - S$ coupling scheme. Energy levels and oscillator strengths are normally computed using a single configuration Hartree-Fock approach. However, when a very high degree of accuracy is needed, such as when computing the transition energies of K_α satellite lines, multi-configuration Hartree-Fock calculations are performed.

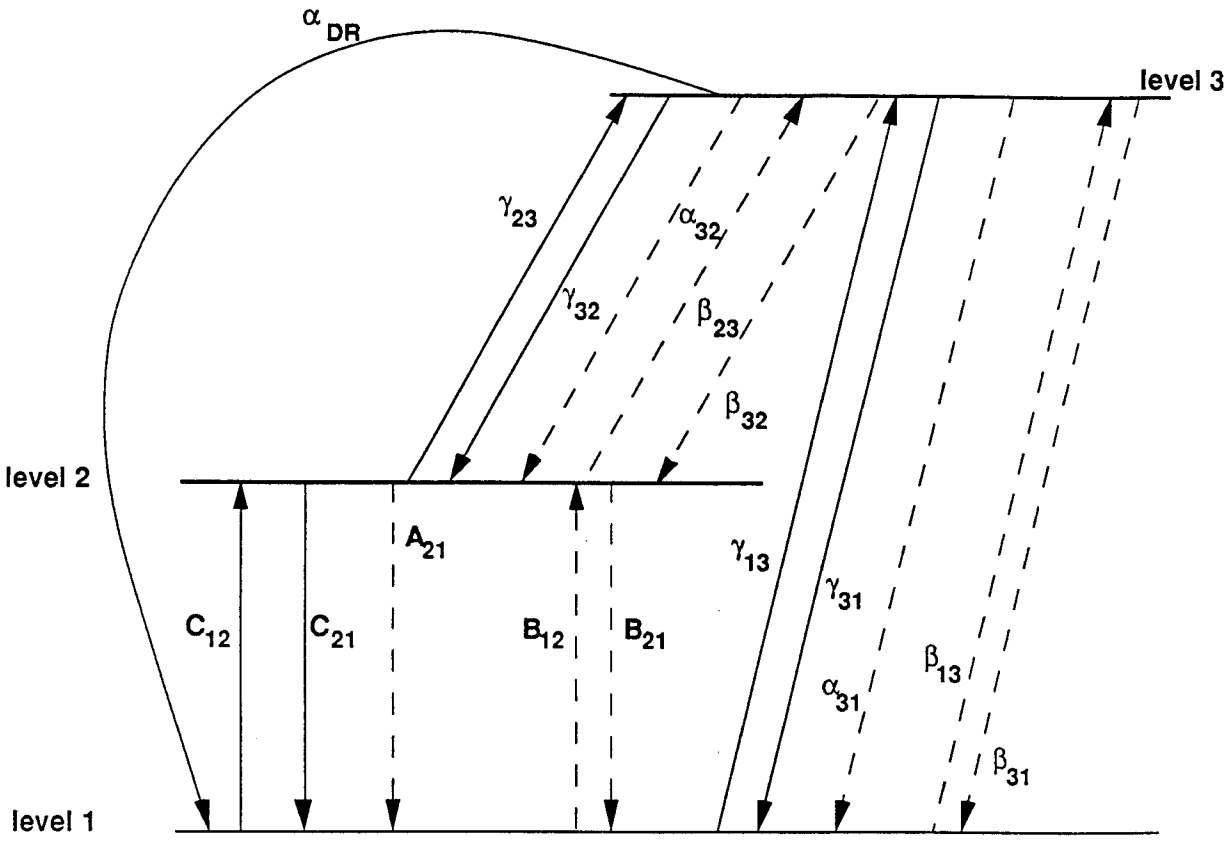

C_{ij} → collisional excitation ($i < j$) or deexcitation ($i > j$)

A_{ij} → spontaneous emission

B_{ij} → photoexcitation ($i < j$) or stimulated emission ($i > j$)

γ_{ij} → collisional ionization ($i < j$) or recombination ($i > j$)

α_{ij} → radiative recombination

α_{DR} → dielectronic recombination

β_{ij} → photoionization ($i < j$) or stimulated recombination ($i > j$)

Figure 19. Schematic illustration of the transitions in a 3-level atom.

For problems involving ion beam-plasma interactions, we also consider the effects of ion-impact ionization and autoionization. Ion-impact ionization rates are computed using a plane-wave Born approximation model with Hartree-Fock wave functions for the bound electrons. To date, our autoionization rates have been determined from previously published fluorescence yields (e.g., Duston et al. (1983) for Al).

5.1. Rate Coefficients

Transition rate coefficients are used to compute the populating and depopulating rates for each level. The rate coefficients are computed as follows.

A. Collisional ionization and recombination

The electron collisional ionization rate coefficients used in this study are calculated using the semi-empirical formula proposed by Burgess and Chidichchimo (1983):

$$q = (2.17 \times 10^{-8}\ \mathrm{cm}^3\ \mathrm{s}^{-1})\ C\ \sum_j\ \zeta_j (I_H/I_j)^{3/2}\ (I_j/kT)^{1/2}\ E_1(I_j/kT)\ w_j \qquad (43)$$

where the summation is over shells j of the initial ion, ζ_j is the effective number of electrons in j, I_j is the effective ionization energy of j, and $I_H = 13.6$ eV. The parameter C is determined from experimental data. For the cases in which experimental data are not available, the value of C is taken to be 2.3. The quantity $E_1(x)$ is the first exponential integral,

$$w_j = [\ln(1 + kT/I_j)]^{\beta/(1+kT/I_j)},$$

and

$$\beta = \frac{1}{4}\{[(100z + 91)/(4z + 3)]^{1/2} - 5\}.$$

Here z is the charge of the initial ion. The electron collisional recombination rate coefficient is obtained by using the principle of detailed balance.

This empirical formula has been shown to produce good agreement with cross-beam experimental data over a wide range of conditions. Figure 20 compares calculated electron impact ionization cross sections with experimental data for Hf^{+3}, Zr^{+3}, and Ti^{+3}. The calculated cross sections are in reasonably good agreement with the experimental data. Typical errors are seen to be $\sim 5 - 25\%$.

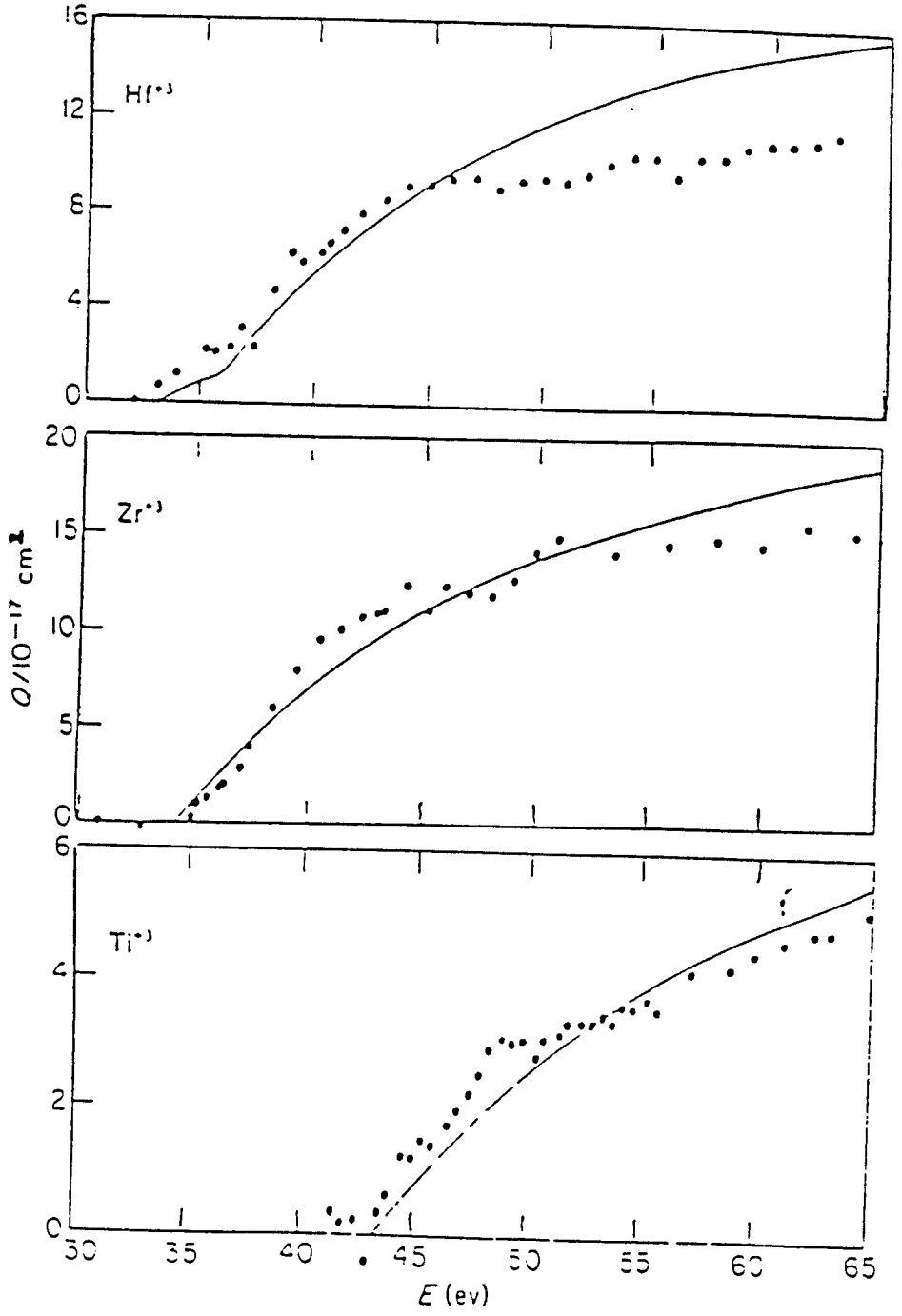

Figure 20. Total electron impact ionization cross section (in units 10^{-17} cm^2) against incident electron energy in eV. The solid curves are based on the semi-empirical formula (Burgess and Chidichchimo 1983), while the circles represent experimental data (Falk et al. 1981).

B. Photoionization, Radiative Recombination, and Stimulated Recombination Rates

Hartree-Fock calculations are performed to obtain frequency-dependent photoionization cross sections. This approach is of course significantly better than using hydrogenic ion cross sections. This is illustrated in Figures 21 and 22, where the photoionization cross sections of NeI and HeI are shown as a function of wavelength. Shown with the Hartree-Fock (HF) results for HeI are curves representing experimental data (Marr and West 1976) and hydrogenic ion cross sections. It is very clear that the HF results are in much better agreement with the experimental data than the hydrogenic cross sections. Figure 23 compares the HF photoionization cross sections for NI with experimental data (Sampson and Cairn 1965). Again, it is seen that HF results are in good general agreement with the data.

The cross section for radiative recombination to the ith atomic level can be obtained from Milne's relation (Sobelman et al. 1981):

$$\sigma^r(\varepsilon) = \frac{g_i(I_i + \varepsilon)^2}{g_e g + \varepsilon m_e c^2}\ \sigma^i(\varepsilon) \tag{44}$$

where σ^i is the photoionization cross section, I_i is the ionization potential of the atom at the i'th state, ε is the kinetic energy of the incident electron, and g_e, g_i, and g_+ are the statistical weights of electron, combined ion, and uncombined ion, respectively.

Rate coefficients at each electron temperature are then obtained by integrating over a Maxwellian velocity distribution. Stimulated recombination rates are determined from the detailed balancing relation with the photoionization rate.

C. Dielectronic Recombination

As shown by Burgess and Seaton (1964), the dielectronic recombination rate in many cases can considerably exceed the radiative recombination rate. Therefore, in low density and high temperature plasmas, dielectronic recombination must be considered. We have calculated the dielectronic recombination rate coefficient using the Burgess-Merts model (Post et al. 1977). Figure 24 shows the dielectronic, radiative, and collisional recombination rates from NeIX to NeVIII as a function of electron temperature. It is clear from these results that dielectronic recombination becomes the dominant recombination process for this ion at temperatures $\gtrsim$ 200 eV.

D. Collisional Excitation and Deexcitation

Three methods are employed for the calculation of excitation cross sections and rate coefficients. For all electric dipole allowed transitions, the excitation cross sections are calculated by using the semiclassical impact-parameter method (SCI) (Burgess and Summer

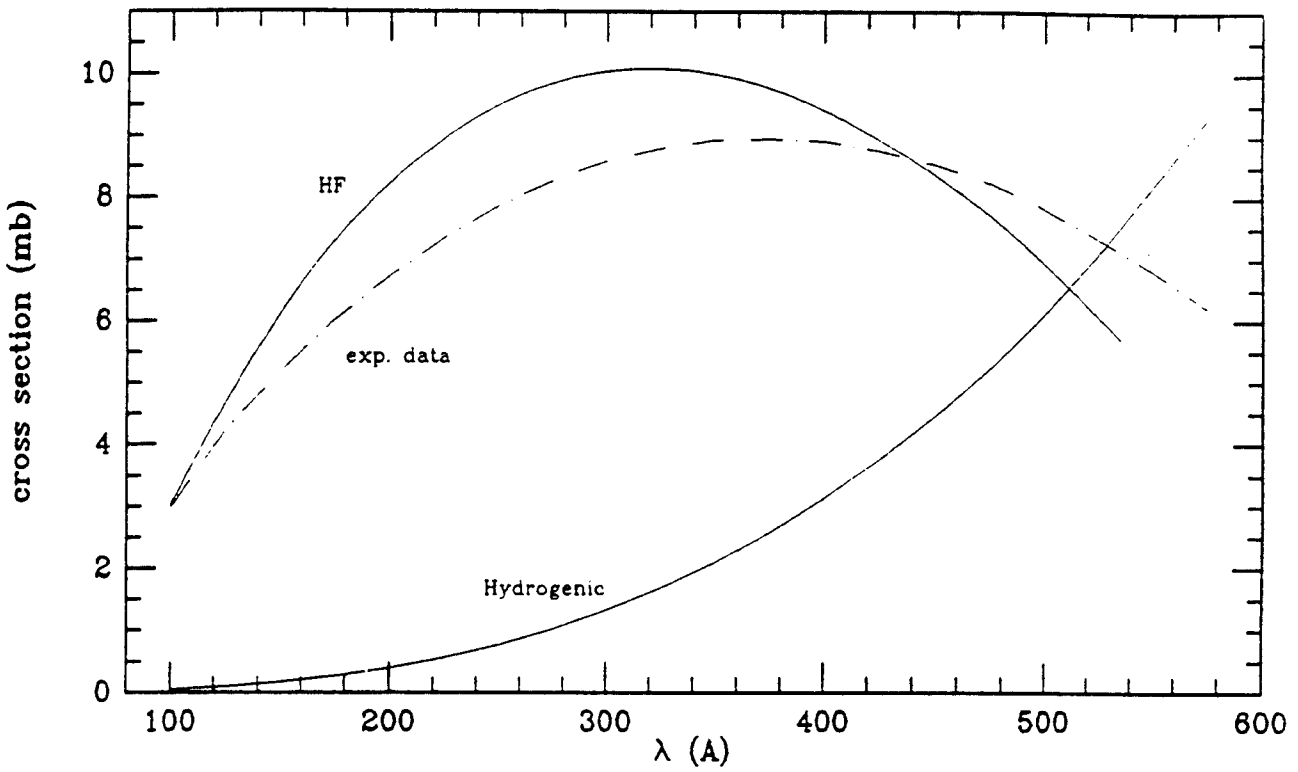

Figure 21. Photoionization cross section for neutral Ne vs. wavelength. Hartree-Fock (HF) calculations are compared with experimental data (Marr and West 1976) and hydrogenic ion approximation results. The photoionization cutoff wavelength is 575 Å (=21.6 eV).

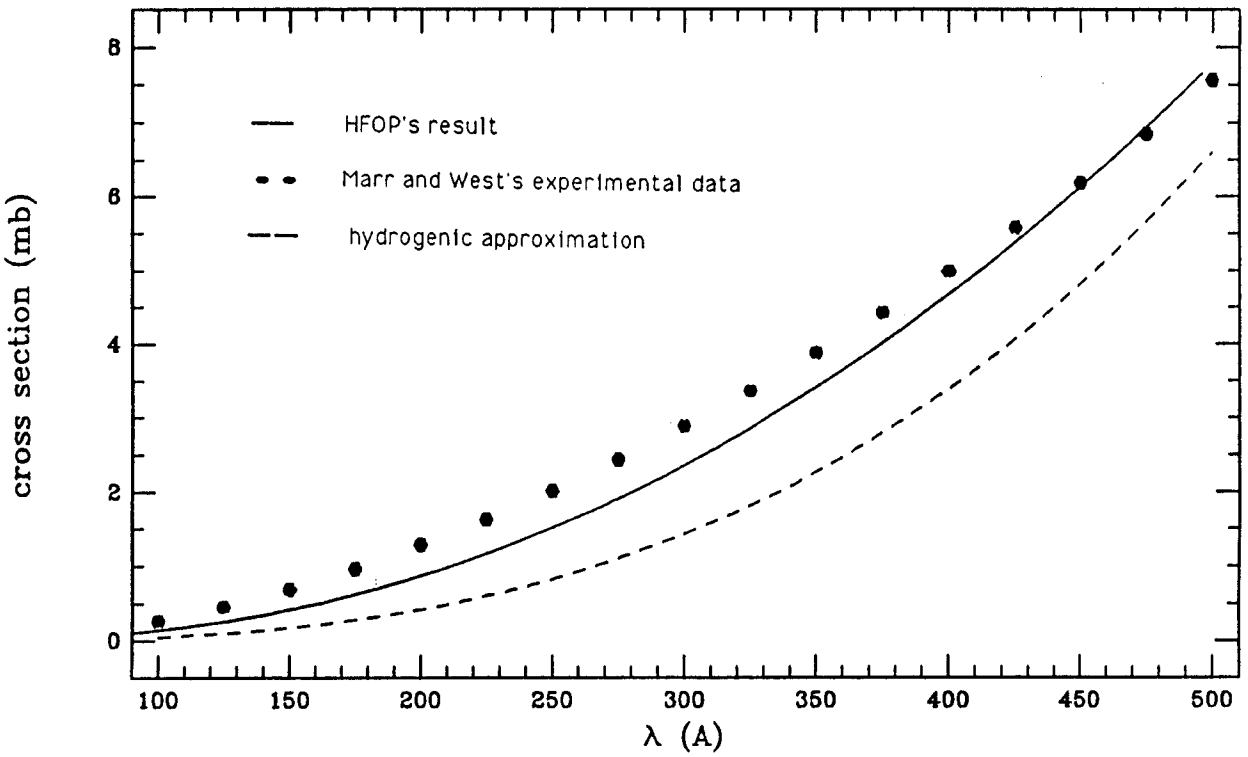

Figure 22. Photoionization cross section for neutral He vs. wavelength. Hartree-Fock results (solid curve) are compared with experimental data and hydrogenic ion approximation results.

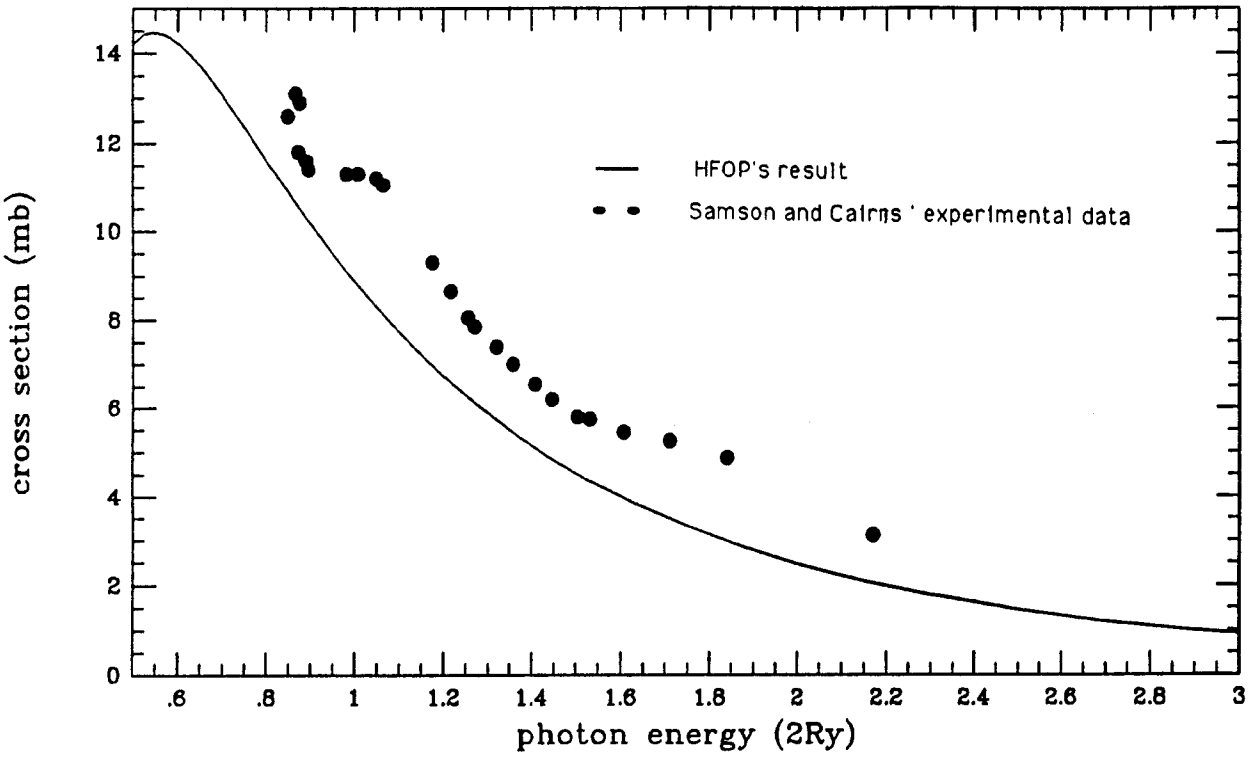

Figure 23. Photoionization cross section for neutral N. Hartree-Fock results (solid curve) are compared with the experimental data of Samson and Cairn (1965).

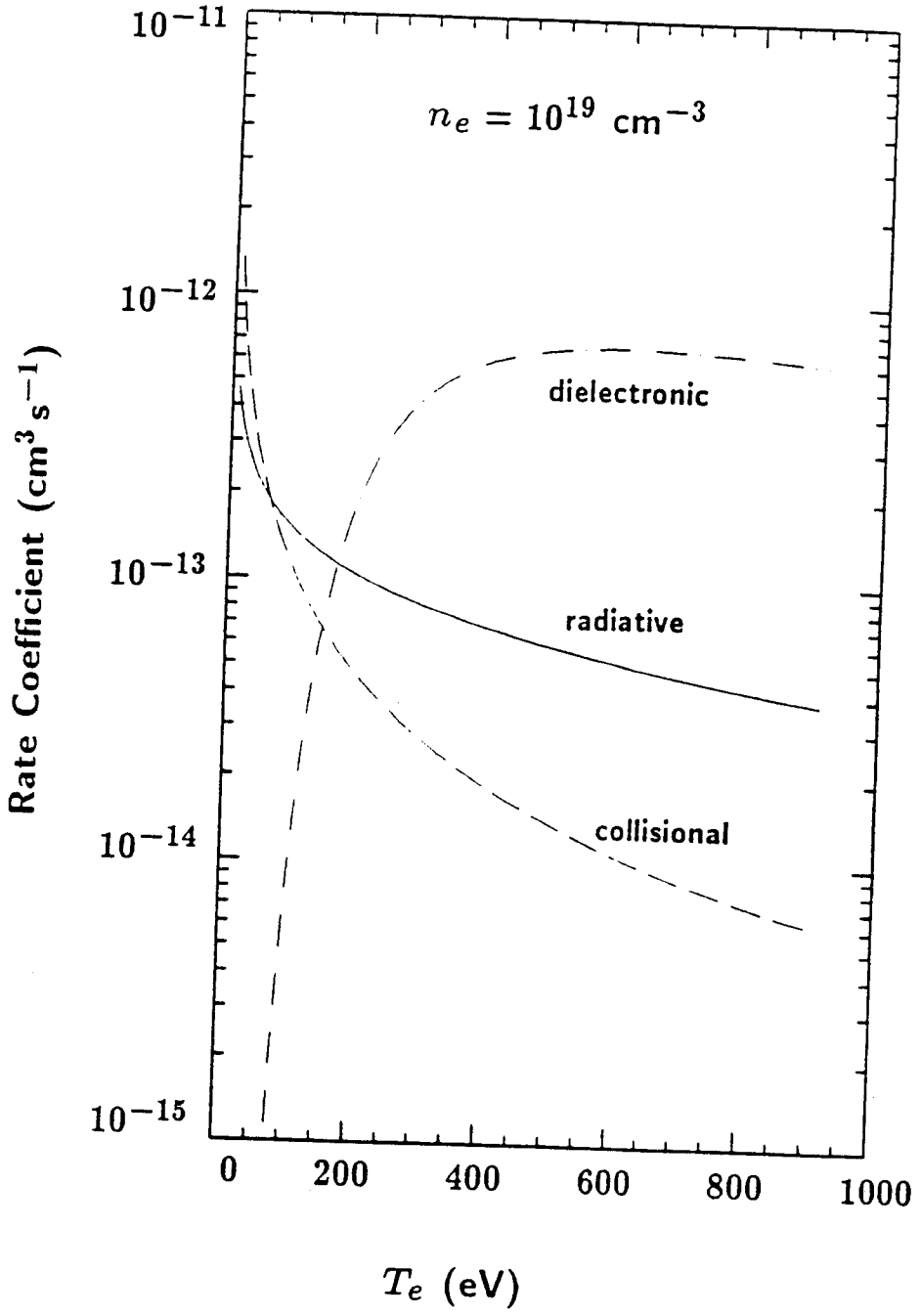

Figure 24. Dielectronic, radiative, and collisional recombination rate coefficients for the transition Ne IX → Ne VIII as a function of electron temperature. The electron density is 1×10^{19} cm^{-3}.

1976). A distorted wave model (DW) (Sobelman et al., 1981) is used to calculate the excitation cross sections of forbidden and spin-flip transitions for helium-like and lithium-like ions, while the orthogonalized function method (Beigman and Vainshtein, 1967) in the Born-Oppenheimer approximation (BOA) is used for other ions. The rate coefficients are obtained by averaging the cross-sections over a Maxwellian electron velocity distribution. The principle of detailed balance is applied to obtain the deexcitation rate coefficients from the excitation rate coefficients.

Figure 25 compares our computed excitation cross sections for LiII using the DW method (solid curve) with those calculated by Van Wyngaarden and Henry (1976) and Christensen and Norcross (1985) using multiconfiguration closed coupling (CC) methods. It is seen that our results are generally within a factor of 2 over the electron kinetic energy range shown. Figure 26 shows our computed electron impact excitation rates for several highly ionized states of Al. Unfortunately, we are unaware of any experimental data for electron impact excitation rates of moderate-to-highly ionized Al.

E. Spontaneous Decay

The spontaneous decay rate for a bound-bound transition is simply proportional to its oscillator strength. We perform Hartree-Fock calculations to determine the oscillator strengths. Table 4 compares our computed oscillator strengths for several transitions of CI, Al III, and Al VIII with those of Smith and Wiese (1971), whose tabulated data are based on experimental data. It is seen that our results are in good general agreement with the Smith and Wiese data, with errors typically ranging from a few percent up to about 25%.

5.2. Atomic Data for K_α Line Spectra

We next discuss our atomic physics calculations of rate coefficients and transition energies relevant to K_α line spectrum. Details of the spectral calculations and the potential of using the K_α spectral region for diagnosing plasma conditions will be discussed in Section 6.2. Here, we will focus on calculations for the proton impact ionization cross sections and transition energies.

Proton impact ionization cross sections are computed using a plane-wave Born approximation model (PWBA) with Hartree-Fock wave functions for bound electrons. Figure 27 shows the cross sections for neutral Al as a function of proton energy. These curves are labeled by the shell from which the electron is ejected. Note that the outer shell cross sections are substantially larger that the inner shell values. Thus, the primary heating (ion stopping) mechanism is the interaction of the proton beam with the outer shell electrons. The calculated cross sections for the 1s shell (which lead to the K_α radiation) are compared with experimental data in Figure 28 (triangles). It is seen that at all proton energies, the

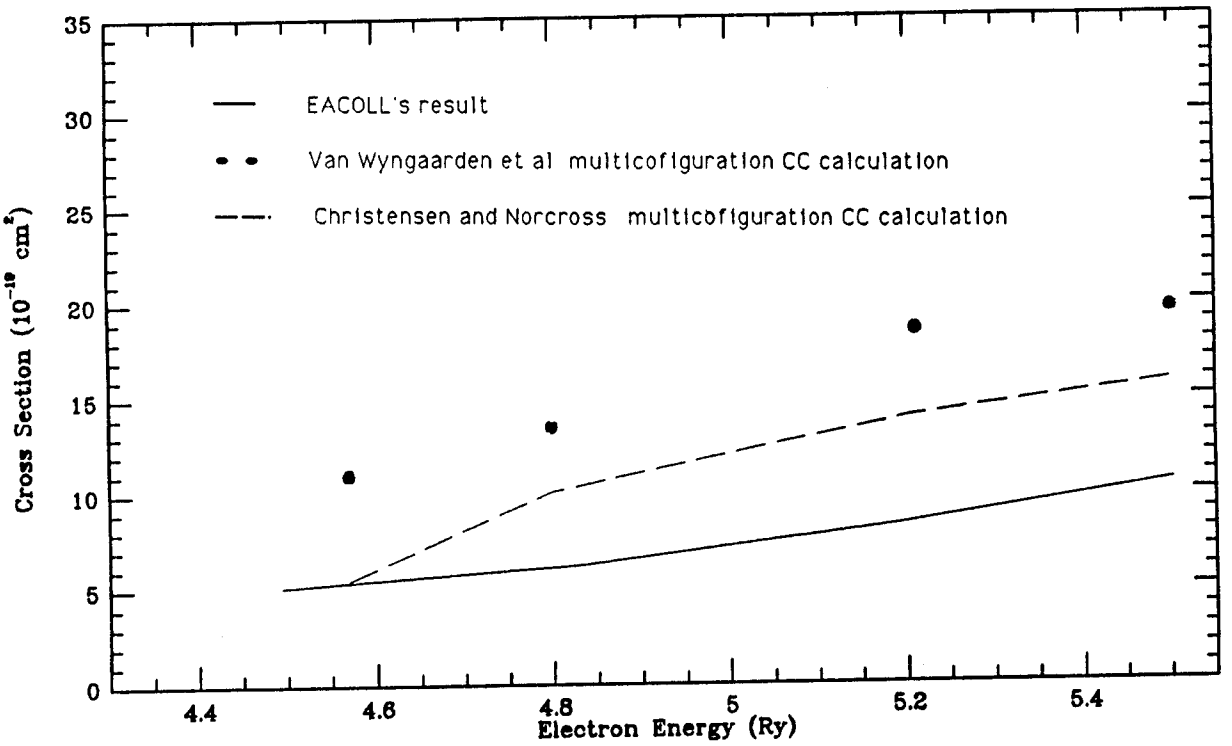

Figure 25. Calculated electron impact excitation cross sections for LiII (solid curve). The closed coupling results of Van Wyngaarden et al. and Christensen and Norcross are also shown.

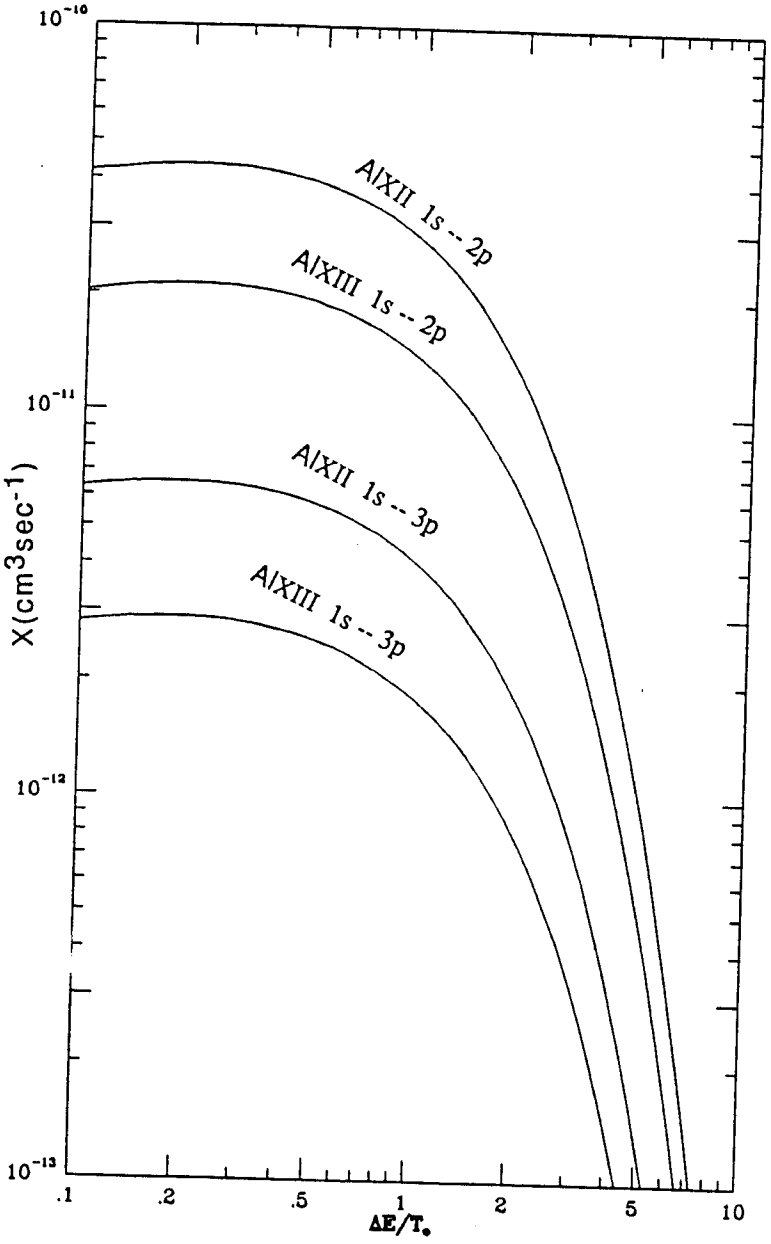

Figure 26. Electron impact excitation rates for H-like and He-like Al calculated using the SCI method.

Table 4.

Oscillator Strengths for CI, AlIII and AlVII

Ion	Transition	f_{SW}	f_{HF}
CI			
	$2s^22p^2\ (^3P)$ -- $2p3s(^3P)$	0.12	0.091
	(^1D) -- (^1P)	0.096	0.092
	$2s^13s^1\ (^3P)$ -- $2p3p(^3P)$	0.37	0.314
	(^3P) -- (^3D)	0.53	0.544
	(^3P) -- (^3S)	0.11	0.122
	(^1P) -- (^1D)	0.56	0.537
	(^1P) -- (^1S)	0.13	0.125
AlIII			
	$2p^63p^1\ (^2P)$ -- $2p^64s^1(^2S)$	0.13	0.129
	$2p^63d^1\ (^2D)$ -- $2p^64p^1(^2P)$	0.17	0.171
	$2p^63d^1\ (^2D)$ -- $2p^65p^1(^2P)$	0.0096	0.0097
	$2p^64s^1\ (^2S)$ -- $2p^64p^1(^2P)$	1.3	1.289
	$2p^64p^1\ (^2P)$ -- $2p^65s^1(^2S)$	0.24	0.233
AlVII			
	$2s^22p^3\ (^4S)$ -- $2s^12p^4(^4P)$	0.21	0.237
	$2p^23s^1\ (^4P)$ -- $2p^23p^1(^4D)$	0.28	0.260
	(^4P) -- (^4P)	0.19	0.169
	(^2D) -- (^2F)	0.21	0.227
	(^2P) -- (^2D)	0.30	0.304
	$2p^23p^1\ (^2F)$ -- $2p^23d^1(^2G)$	0.41	0.300

Notes:

SW, data compiled by Smith and Wiese from experimental data
HF, Our calculation results by using HF method.

calculated cross-sections are within a factor of 2 of the experimental values. It is also expected that the calculations should be even more accurate at higher proton energies because the assumptions in the PWBA model become more valid.

Figure 29 shows how the proton impact ionization cross section for Al K-shell electrons varies with the ionization state of Al. As the ionization stage of the Al increases the cross section decreases in an almost linear fashion. Our calculations indicate that the proton impact ionization for the K-shell electrons for Al II is about a factor of 2 higher than that for Al XIII.

To determine the wavelengths of K_α satellite lines, we have performed multiconfiguration Hartree-Fock calculations with relativistic mass and Darwin corrections. Tables 5 and 6 show results for the energies and transition energies for Al. The main purpose of the calculations was to test the accuracy of the code for use in K_α diagnostics experiments by comparing the computed wavelengths with experimental data. (K_α transitions occur when a proton beam interacts with an Al target, and causes vacancies in the K-shell.) Table 5 shows the energies of the atomic levels, while Table 6 shows the calculated wavelengths and compares them with the peaks in Sandia data (experimental column; Bailey et al. 1991).

The F-like Al (Al V) experimental spectrum of Bailey et al. (1991) shows a high degree of structure. Three emission peaks are clearly seen in the data. This portion of the spectrum is shown in detail in Figure 30. Also shown are the calculated transition energies for 4 K_α transitions. Note that 2 transitions may be contributing to the central peak in the experimental data. The calculated wavelengths match up quite well with the experimental peaks. We estimate the accuracy of the computed wavelengths to be a few milliangstroms (less than 0.1%).

These results represent a significant improvement in accuracy over previous results presented in Bailey et al., where wavelengths were determined from Herman-Skillman calculations (based on a Hartree-Fock-Slater model). The good agreement between our calculations and the experimental data gives us confidence that we can determine which transitions are responsible for the peaks in the experimental emission spectra. This in turn means that plasma temperatures in ion beam-heated targets can be determined more reliably.

6. Target Calculations

We have performed a number of calculations using our radiative transfer and atomic physics codes to predict the emission spectra of targets for future KALIF beam-plasma interaction experiments. The purpose of the calculations is to develop an understanding of the physical processes that influence the emission spectra from targets, and to begin to identify spectral features that can be used to deduce plasma conditions (e.g., temperature

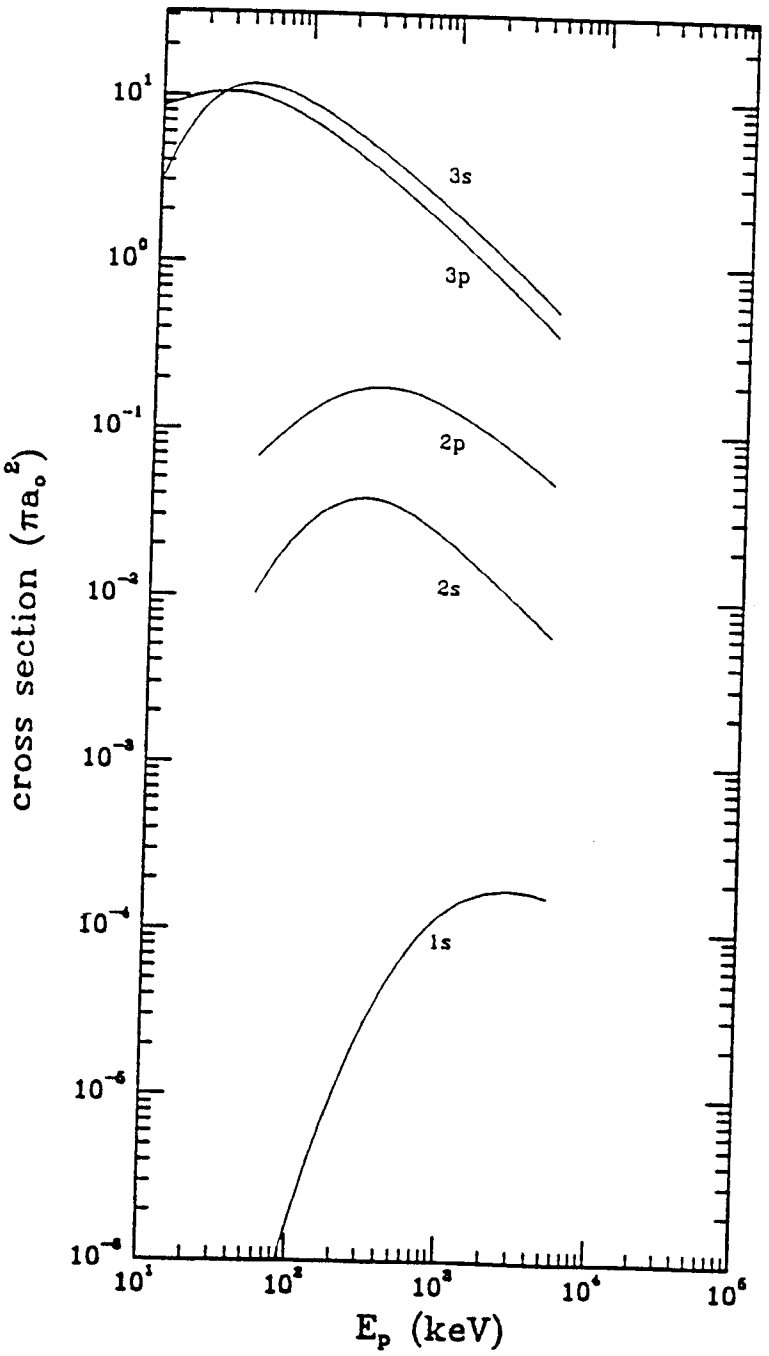

Figure 27. Proton impact ionization cross sections for all shells of neutral Al.

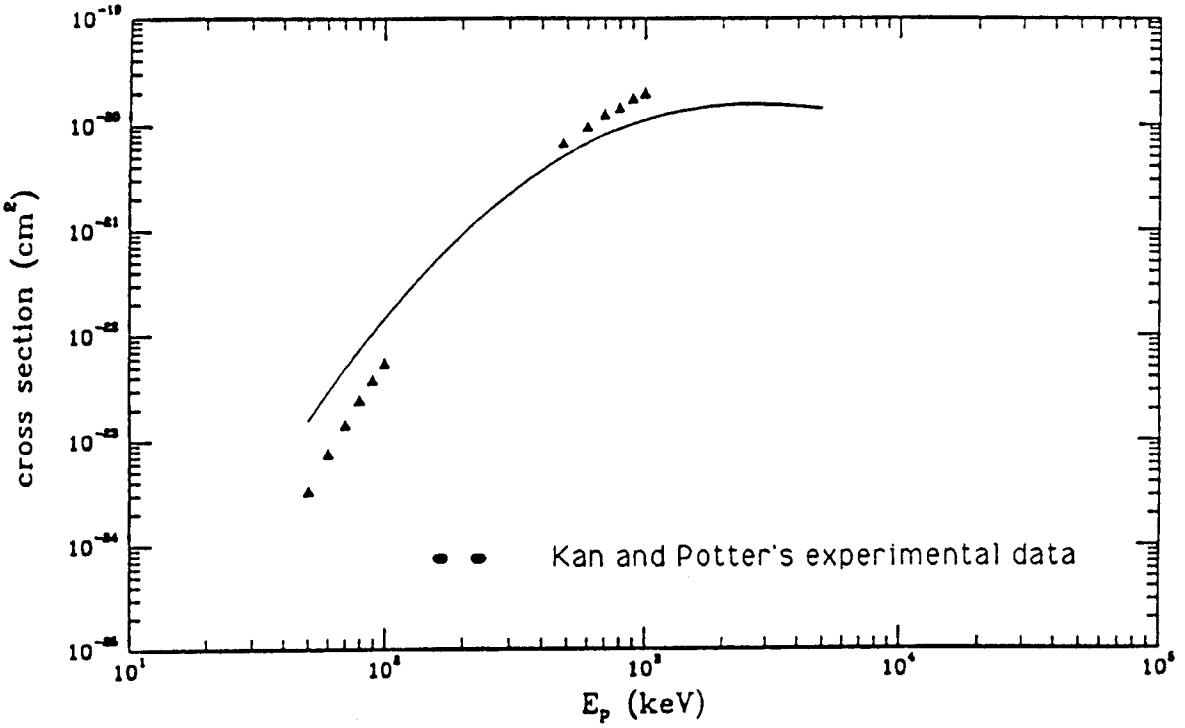

Figure 28. Comparison of calculated proton impact ionization cross section for the 1s shell and the experimental data of Khan and Potter (1965).

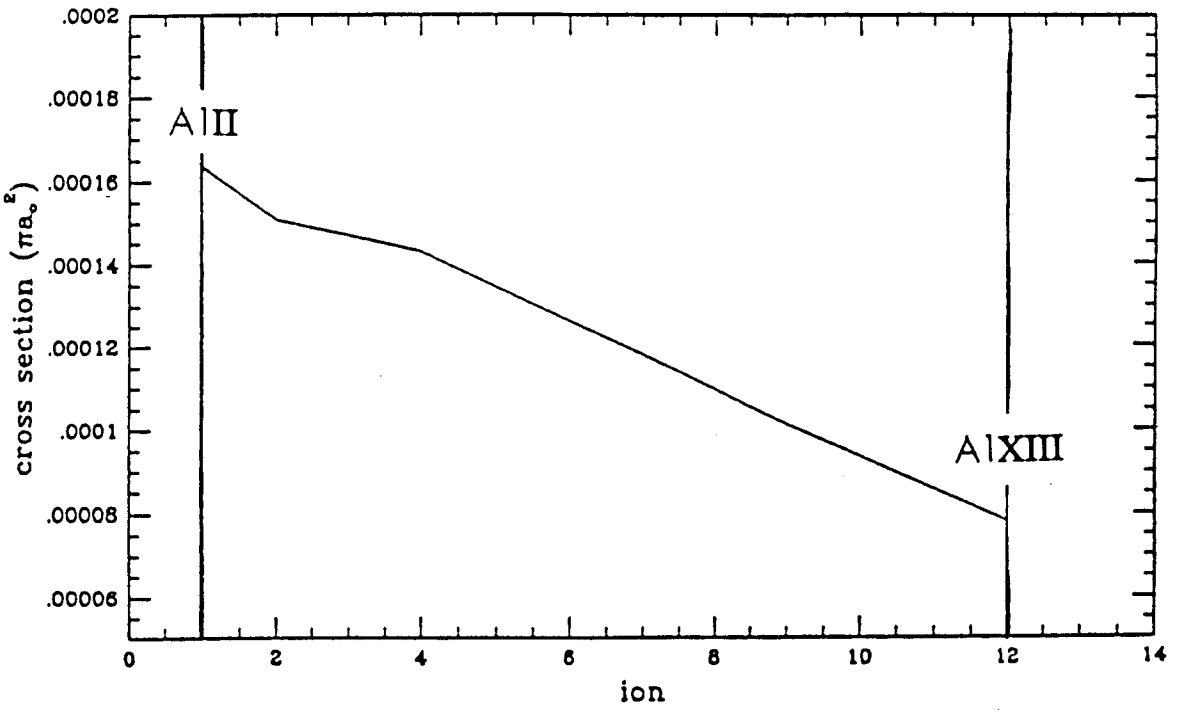

Figure 29. Dependence of the proton impact ionization cross section for the 1s shell on the ionization stage of Al.

Table 5.

Energy Levels of Al Ions (in 2Ry)

Ion	Configuration	Term	E_{mchf}	ΔE_{re}	E_t
AlII	1s(1)2s(2)2p(6)3s(2)	2S	-183.80137	-0.15891	-183.96028
	1s(2)2s(2)2p(5)3s(2)	2P	-238.38741	-0.20861	-238.59602
AlIII	1s(1)2s(2)2p(6)3s(1)	1S	-182.66834	-0.15789	-182.82623
		3S	-182.67897	-0.15800	-182.83697
	1s(2)2s(2)2p(5)3s(1)	1P	-237.23792	-0.20932	-237.44724
		3P	-237.25841	-0.20937	-237.46778
AlIV	1s(1)2s(2)2p(6)	2S	-181.03049	-0.15648	-181.18697
	1s(2)2s(2)2p(5)	2P	-235.64703	-0.20806	-235.85509
AlV	1s(1)2s(2)2p(5)	1P	-174.76074	-0.15601	-174.91675
		3P	-175.02640	-0.15622	-175.18261
	1s(2)2s(2)2p(4)	1S	-229.67681	-0.20769	-229.88450
		1D	-229.86675	-0.20790	-230.07475
		3P	-230.05752	-0.20780	-230.26531
	1s(1)2s(1)2p(6)	1S	-173.42654	-0.14560	-173.57217
		3S	-173.52542	-0.14610	-173.67151
	1s(2)2s(1)2p(5)	1P	-227.92166	-0.19759	-228.11926
		3P	-228.56012	-0.19835	-228.75847
AlVI	1s(1)2s(2)2p(4)	2S	-167.03434	-0.15481	-167.18914
		2D	-167.24941	-0.15505	-167.40445
		4P	-167.60196	-0.15535	-167.75731
	1s(2)2s(2)2p(3)	2P	-222.61890	-0.20704	-222.82594
		2D	-222.81809	-0.20717	-223.02525
		4S	-223.12157	-0.20738	-223.32894
AlVII	1s(1)2s(2)2p(3)	1P	-157.72217	-0.152813	-157.87497
		1D	-157.94252	-0.15300	-158.09552
		3P	-158.01708	-0.15312	-158.17020
		3D	-158.24069	-0.15330	-158.39399
		3S	-158.12499	-0.15313	-158.27812
	1s(2)2s(2)2p(2)	1S	-213.76244	-0.20538	-213.96781
		1D	-214.01984	-0.20568	-214.22545
		3P	-214.23553	-0.20577	-214.44130
AlVIII	1s(1)2s(2)2p(2)	2S	-146.79065	-0.14983	-146.94048
		2D	-147.14976	-0.15014	-147.3002
	1s(2)2s(2)2p(1)	2P	-203.77520	-0.20327	-203.97850
AlIX	1s(1)2s(2)2p(1)	1P	-134.35842	-0.14571	-134.50411
		3P	-134.71062	-0.14612	-134.85674
	1s(2)2s(2)	1S	-191.80689	-0.19975	-192.00664

Table 6.

Wavelengths of the Term-dependent Lines (in Angstroms)

Ion	Initial State	Final State	Wavelength	Exp. data
AlII	1s(1)2s(2)2p(6)3s(2)	1s(2)2s(2)2p(5)3s(2)		
	2S	2P	8.3373	
AlIII	1s(1)2s(2)2p(6)3s(1)	1s(2)2s(2)2p(5)3s(1)		
	1S	1P	8.3395	≅8.340
	3S	3P	8.3380	
AlIV	1s(1)2s(2)2p(6)	1s(2)2s(2)2p(5)		
	2S	2P	8.3324	
AlV	1s(1)2s(2)2p(5)	1s(2)2s(2)2p(4)		
	1P	1S	8.2869	≅8.288
	1P	1D	8.2583	≅8.258
	3P	3P	8.2696	≅8.270
	1s(1)2s(1)2p(6)	1s(2)2s(1)2p(5)		
	1S	1P	8.3508	
	3S	3P	8.2690	
AlVI	1s(1)2s(2)2p(4)	1s(2)2s(2)2p(3)		
	2S	2P	8.1873	
	2D	2P	8.2191	
	2D	2D	8.1896	
	4P	4S	8.1970	≅8.202
AlVII	1s(1)2s(2)2p(3)	1s(2)2s(2)2p(2)		
	1P	1S	8.1207	
	1P	1D	8.0836	
	1D	1D	8.1153	
	3P	3P	8.0949	
	3S	3P	8.1105	
	3D	3P	8.1273	≅8.126
AlVIII	1s(1)2s(2)2p(2)	1s(2)2s(2)2p(1)		
	2S	2P	7.9861	
	2D	2P	8.0370	≅8.044
AlIX	1s(1)2s(2)2p(1)	1s(2)2s(2)		
	1P	1S	7.9216	
	(intercombination line) 3P	1S	7.9705	≅7.969

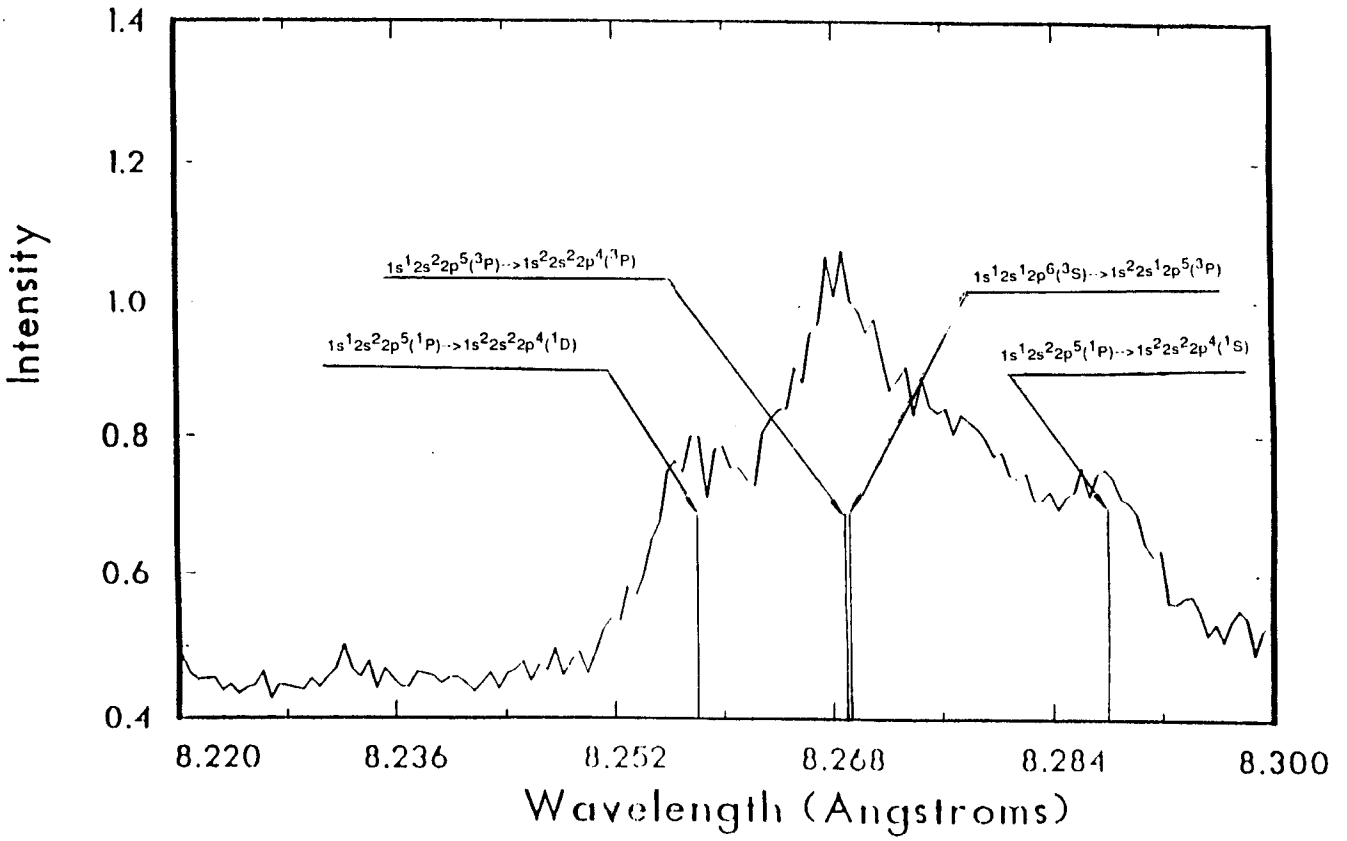

Figure 30. Calculated wavelengths for 4 K_α lines of Al V (vertical lines) are compared with the experimental K_α spectrum obtained by Bailey et al. (1991).

and density). Most of the calculations presented here are for Al plasmas with temperatures in the 10 to 50 eV range and densities of $10^{-2} - 10^{-1}$ times solid density. We also briefly discuss the implications of using carbon targets in the context of using their K_α satellite lines as a temperature diagnostic. All results shown in this section are for planar plasmas with uniform temperatures and densities. We also note the results shown in this section do not include the effects of inner shell photoabsorption.

In this section, we first discuss the general features of target emission spectra. In particular, we will show how the overall spectrum changes as a function of slab thickness and temperature. Secondly, we examine the potential for using K_α satellite lines as a temperature diagnostic for ion beam-heated plasmas. These lines, which result from ion impact ionization of target ions by the incoming beams, can be seen in the soft x-ray part of the spectrum (near 1.5 keV for Al, 0.3 keV for C). Finally, we discuss our recommendations for target experiments on KALIF.

6.1. Emission Spectra of Moderately-Ionized Aluminum

We first examine the emission spectra from Al targets in the absence of an ion beam (i.e., with no K_α line emission). Consider the case of a planar Al foil which has expanded 100 times from its original thickness L_0 . Assume the plasma has a uniform density of $n = 10^{-2} n_0$ ($n_0 \equiv$ solid density $= 6 \times 10^{22}$ cm^{-3} for Al) and uniform temperature T. Let us now examine how the spectral flux varies with original foil thickness and temperature.

Figures 31, 32, and 33 show the spectral fluxes for Al plasmas corresponding to an original foil thickness of 0.1, 1.0, and 10 μm, respectively. The thicknesses of the expanded plasma slabs are therefore 10^{-2}, 10^{-1}, and 1 mm. In each case the plasma temperature is 50 eV and the density $10^{-2} n_0$. In each figure, the blackbody flux is shown for comparison.

With an original foil thickness of 0.1 μm (Fig. 31), the flux below photon energies of $h\nu \lesssim 10$ eV is basically blackbody. However, above 10 eV considerable structure is seen in the spectrum in the form of emission lines and bound-free edges. As the thickness of the foil increases, the flux becomes more like a blackbody over a wider spectral range. Figure 33 shows that for an Al foil with $L_0 = 10$ μm, the spectrum is very much like a blackbody. Since targets used in ion beam experiments tend to be $\gtrsim 10$ μm in size because of the stopping range of the ions, one can expect spectral fluxes to be blackbody-like over a wide spectral range.

The reason for dependence of the emission spectrum on the foil thickness can be understood by examining the frequency-dependence of the optical depth. Figures 34, 35, and 36 show the optical depths corresponding to spectral fluxes shown in Figures 31-33. The optical depths correspond to the entire slab thickness and were computed along a ray per-

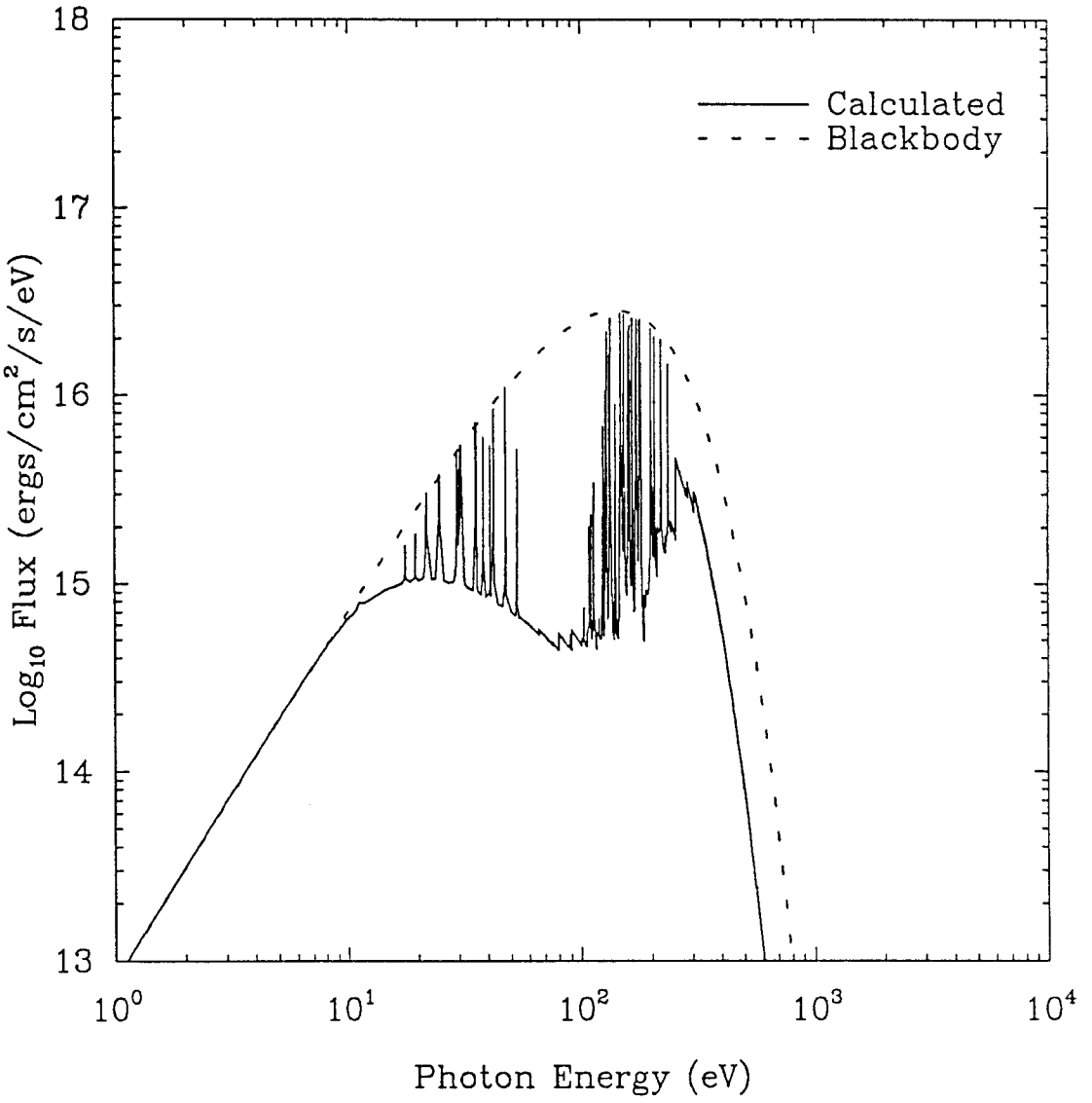

Figure 31. Spectral flux emitted from an Al plasma at $T = 50$ eV and $n = 10^{-2}n_0$. The slab width is 0.01 mm, corresponding to an Al foil with an original thickness of 0.1 μm.

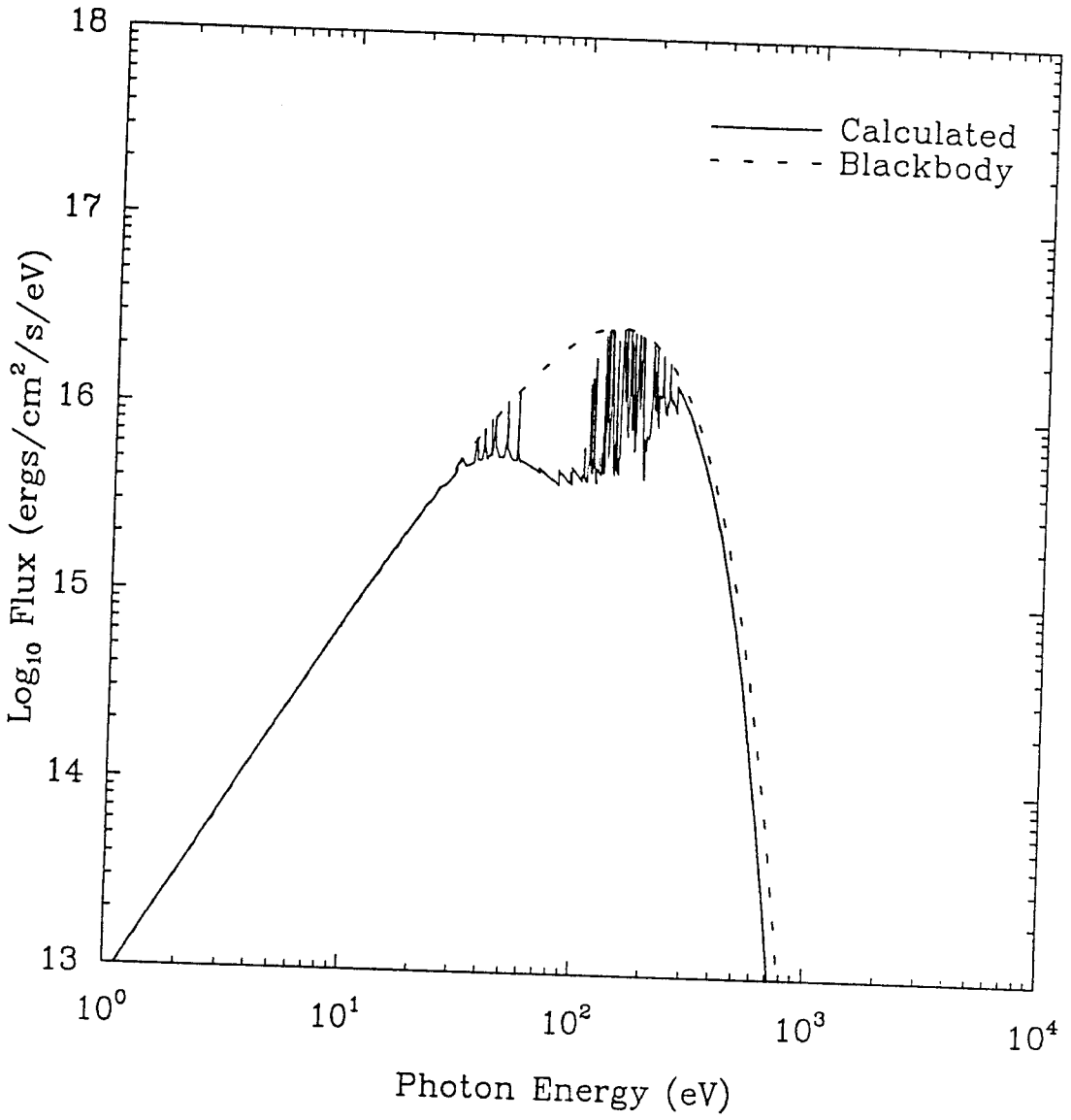

Figure 32. Spectral flux emitted from an Al plasma at $T = 50$ eV and $n = 10^{-2}n_0$. The slab width is 0.1 mm, corresponding to an Al foil with an original thickness of 1.0 μm.

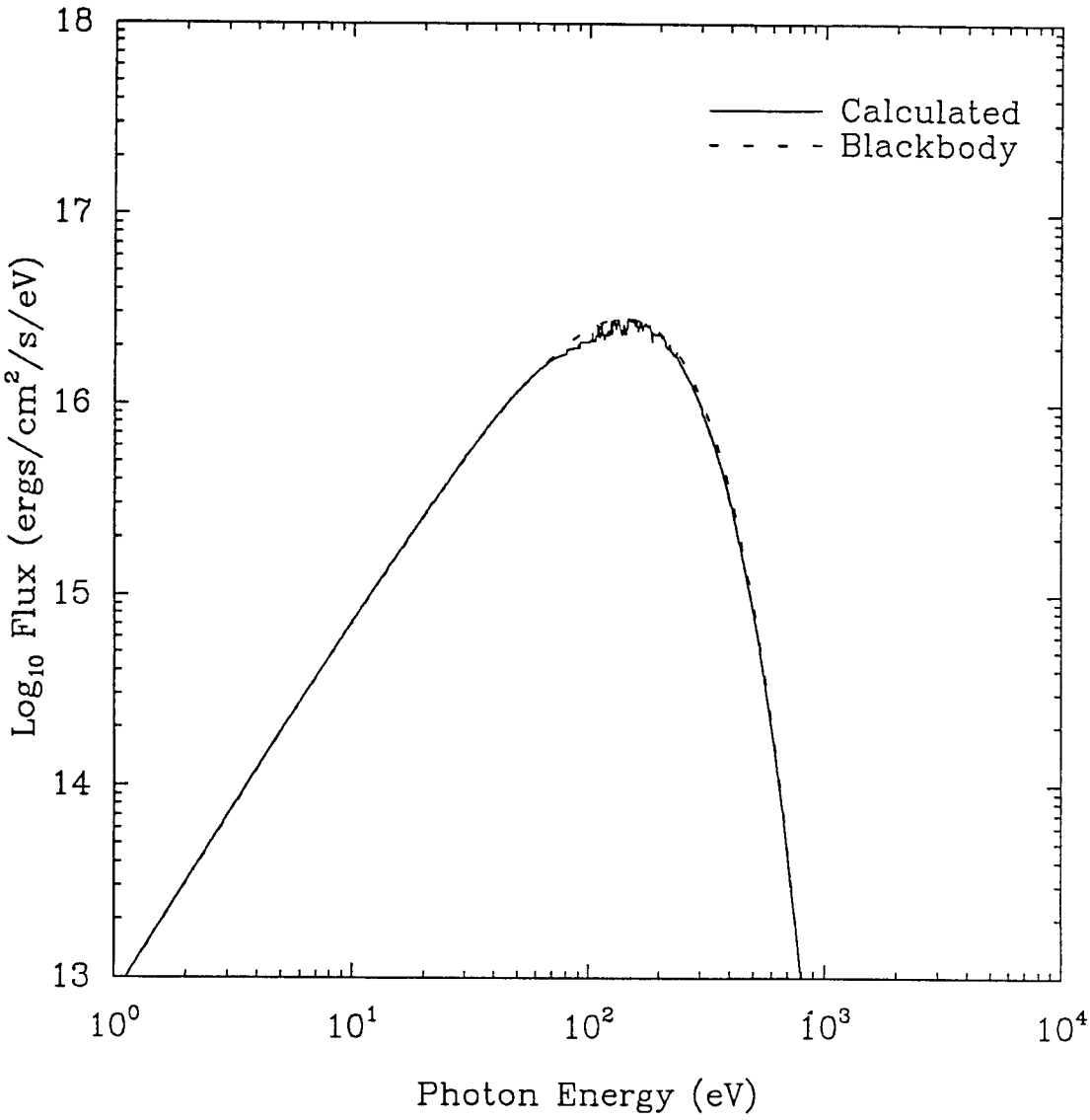

Figure 33. Spectral flux emitted from an Al plasma at $T = 50$ eV and $n = 10^{-2}n_0$. The slab width is 1.0 mm, corresponding to an Al foil with an original thickness of 10 μm.

pendicular to the slab boundary. Note that when the original foil thickness is $\gtrsim 10$ μm (Fig. 36), the plasma is optically thick at all photon energies below 1 keV. However, when $L_0 = 0.1$ μm (Fig. 34), the plasma is optically thin ($\tau < 1$) to continuum radiation at photon energies above 10 eV. Only the line cores are optically thick at these higher frequencies. When the continuum is optically thin, emission lines become discernable in the spectrum. (We again note that these results do not include the effects of inner shell photoabsorption (see Section 2.4).)

The variation in the target emission spectrum with temperature is shown in Figure 37, where the spectral fluxes from Al plasmas with $T = 50$ eV, 15 eV, and 5 eV are shown. In each case, the plasma density is $n = 10^{-2} n_0$, $L = 10^{-2} L_0$, and $L_0 = 1.0$ μm. The corresponding optical depth plots are shown in Figures 38, 39, and 40. As the temperature rises from 5 eV to 50 eV, more structure is discernable in the emission spectra. This is because at lower temperatures (5 eV and below), the peak of the flux curve shifts to lower photon energies where the plasma tends to be optically thick.

Based on these results we expect that the bulk of the radiation emitted by plasmas created during KALIF experiments will very much resemble a blackbody curve at these temperatures. This is because foil thicknesses, which are constrained by the energy deposition properties of the beam, are expected to be $\gtrsim 10$ μm. Also, at photon energies where the plasma is optically thick, the emission spectra will be strongly dependent on the temperatures in the outermost regions of the plasma (facing the detector). We shall now focus on how radiation emitted in the soft x-ray portion of the spectrum for ion beam-heated plasmas can be used to diagnose plasma conditions.

6.2. Using K_α Satellite Lines as a Temperature Diagnostic

Plasmas heated by intense ion or electron beams can emit detectable x-ray line radiation that can provide important constraints for diagnosing plasma conditions (Nardi and Zimamon 1981, Chenais-Popovics et al. 1989, Bailey et al. 1991). The reason is because energetic beams eject inner shell electrons of the target plasma, which can produce fluorescent line radiation as the inner shell vacancy is filled by an outer shell electron. Such lines are called K_α lines when a vacancy in the K shell ($n = 1$) is filled with an electron from the L shell ($n = 2$). Similarly, L_α lines result from a L shell vacancy being filled by an M shell ($n = 3$) electron.

The production of K_α lines when a moderately-ionized Al plasma is irradiated by an intense proton beam is illustrated in Figure 41. For a plasma that is hot enough to have a significant amount of Al V, small concentrations of highly-excited Al VI are produced as a K shell electron is ejected by proton-impact ionization. These highly-excited "autoionizing" levels are depopulated primarily in two ways: (1) a radiationless autoionization in which

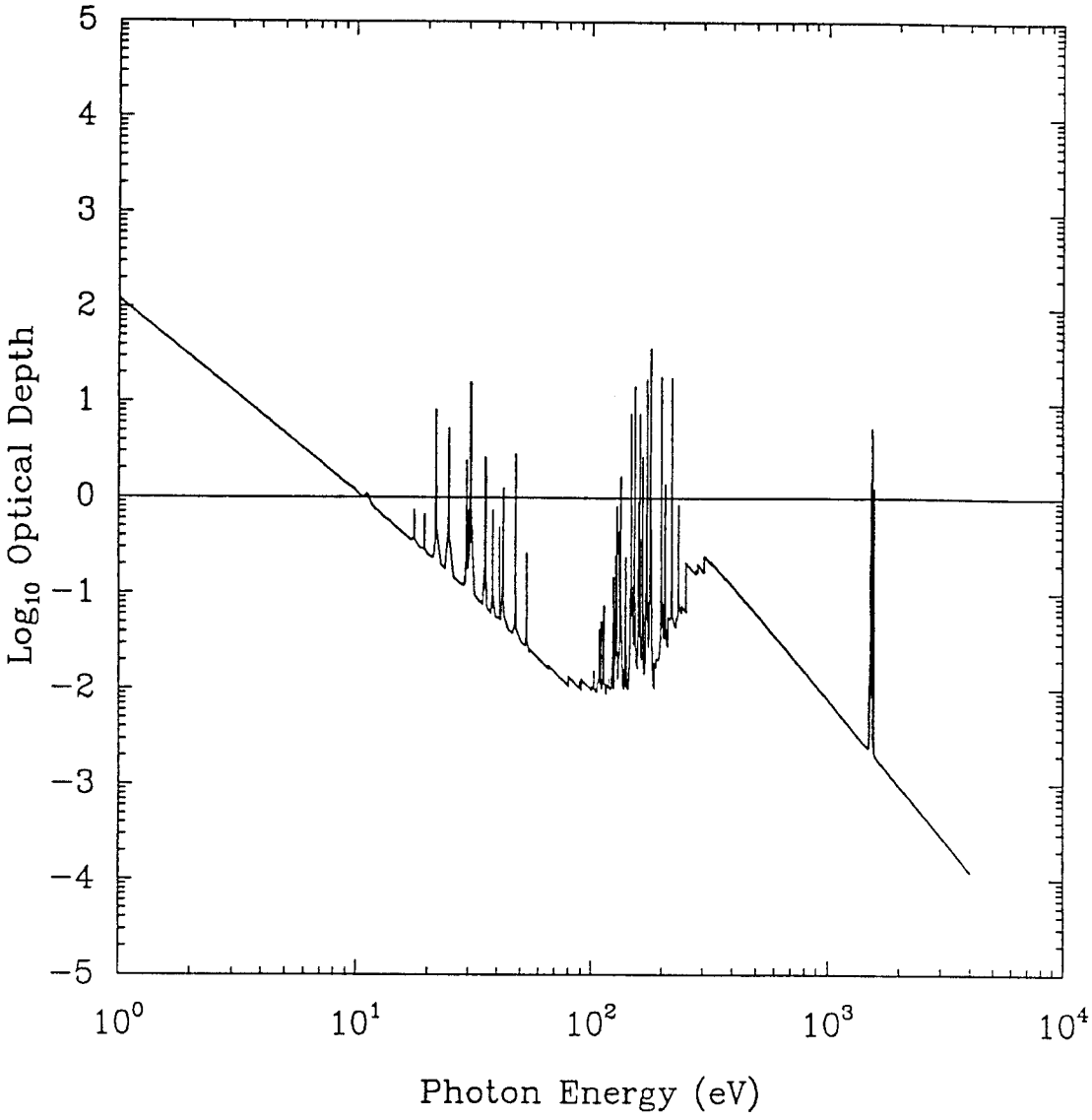

Figure 34. Dependence of optical depth on photon energy for the case shown in Figure 31.

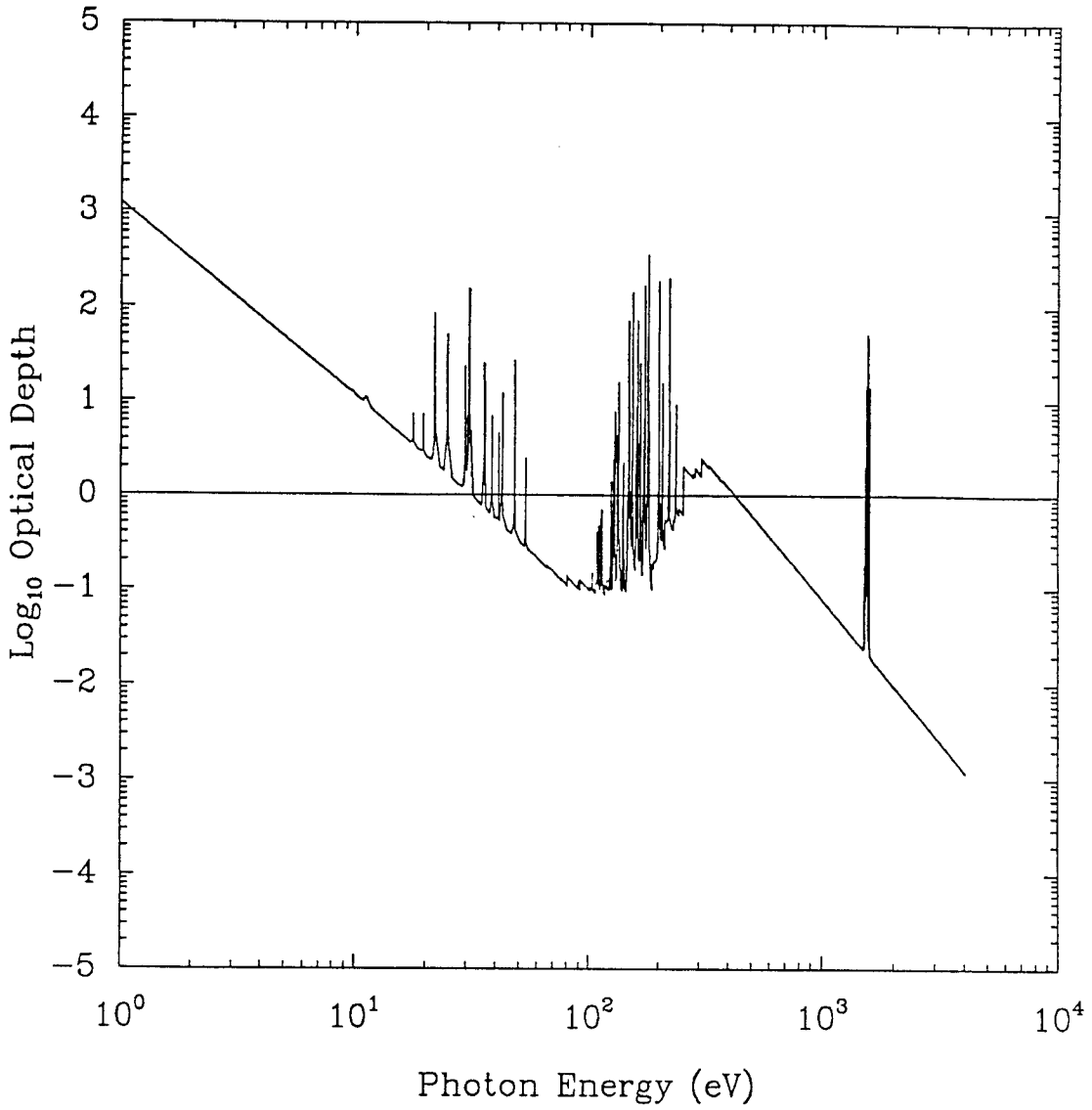

Figure 35. Dependence of optical depth on photon energy for the case shown in Figure 32.

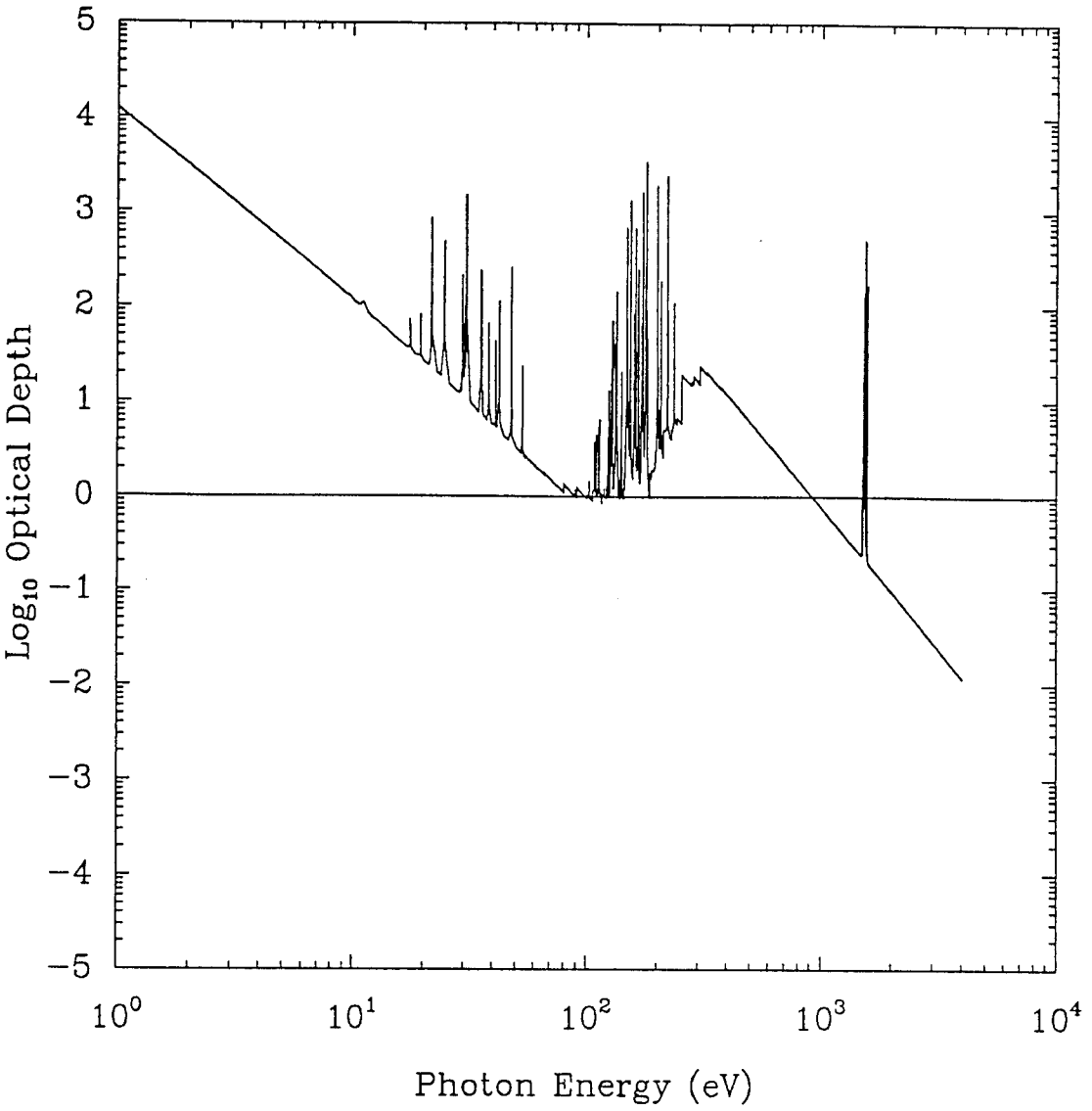

Figure 36. Dependence of optical depth on photon energy for the case shown in Figure 33.

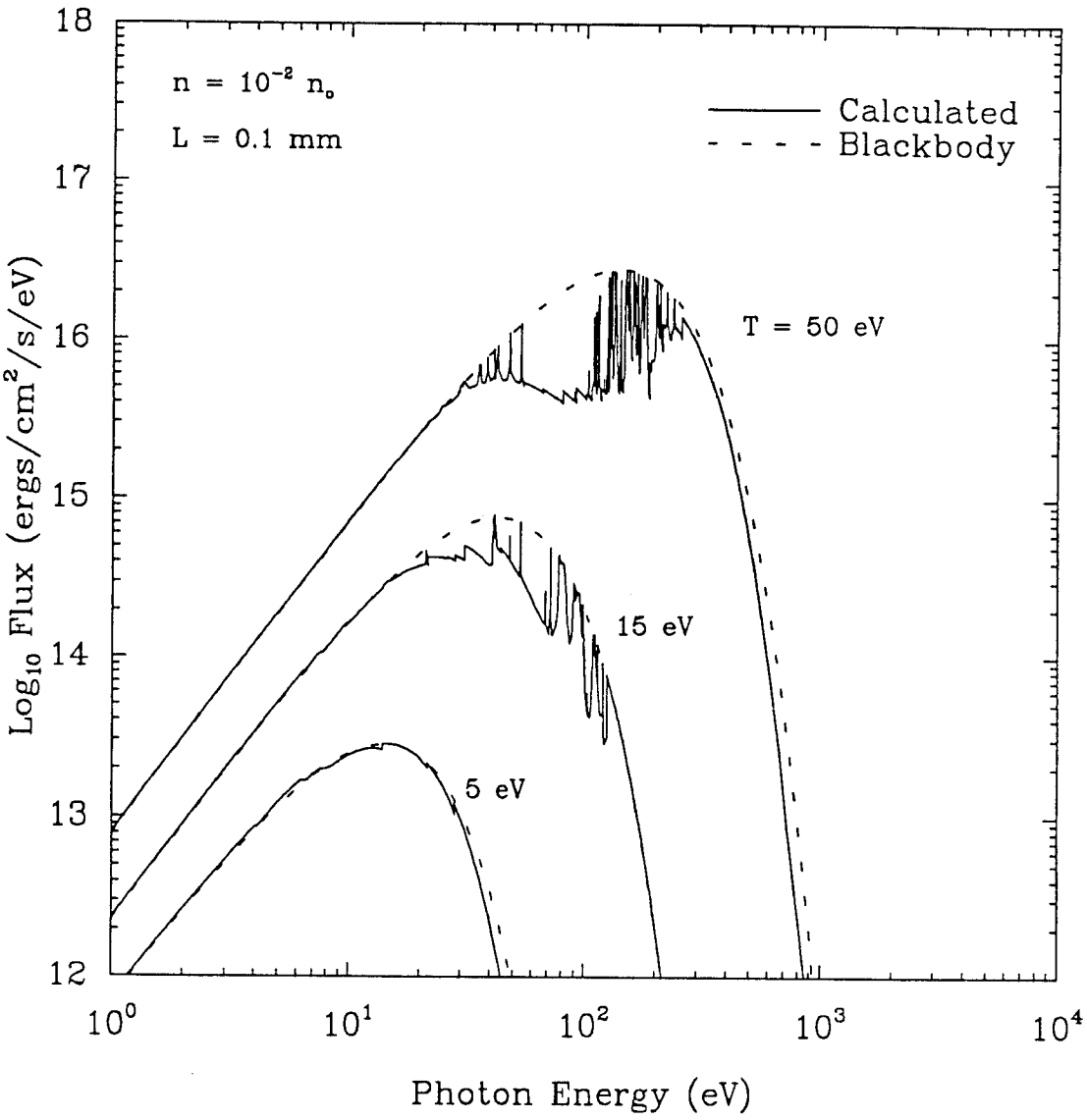

Figure 37. Spectral flux emitted from an Al plasma at $T = 5$ eV, 15 eV, and 50 eV. In each case $n = 10^{-2}n_0$ and $L = 0.1$ mm. The dashed curves represent the blackbody flux for each temperature.

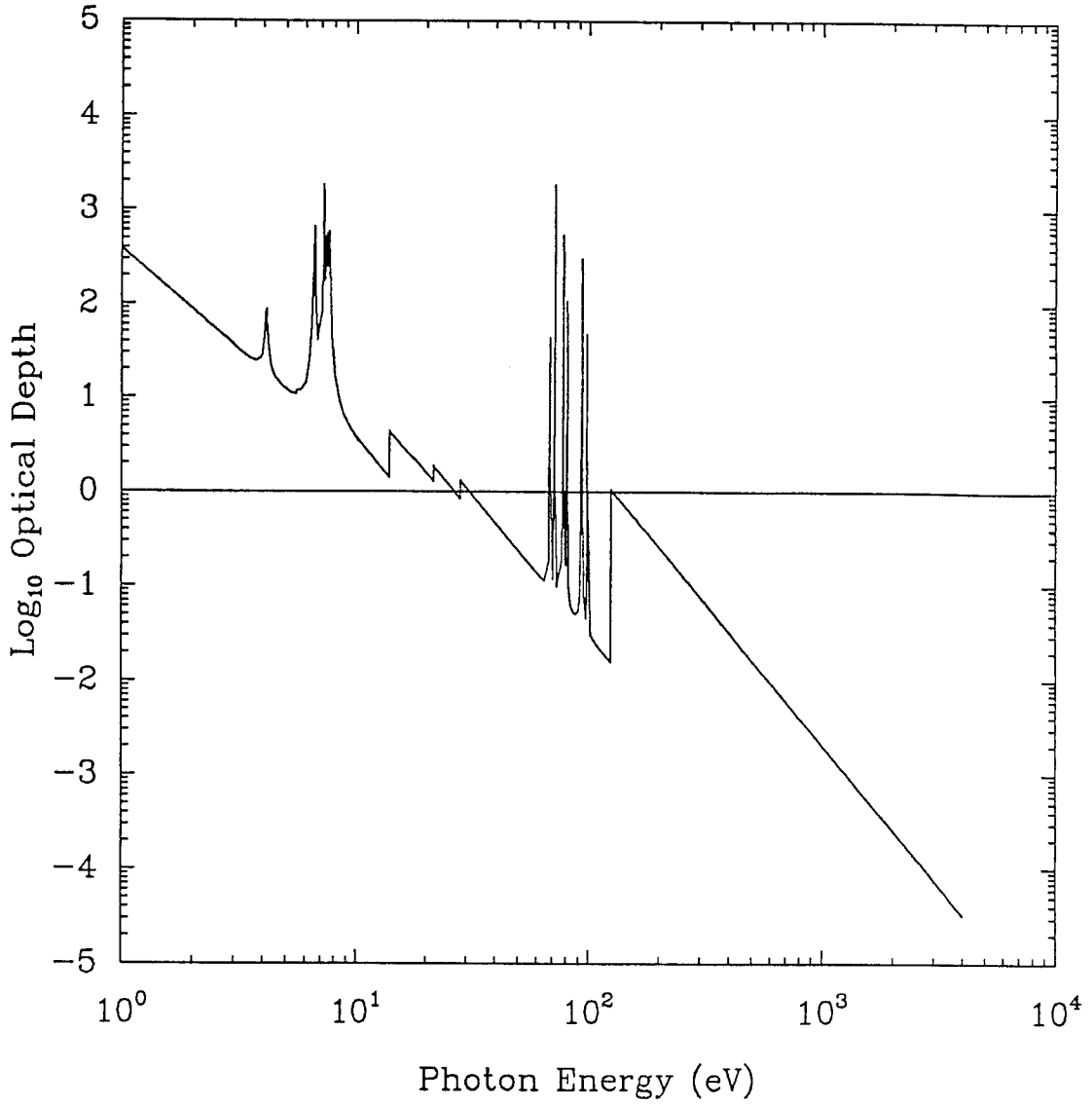

Figure 38. Dependence of optical depth on photon energy for the $T = 5$ eV case shown in Figure 37.

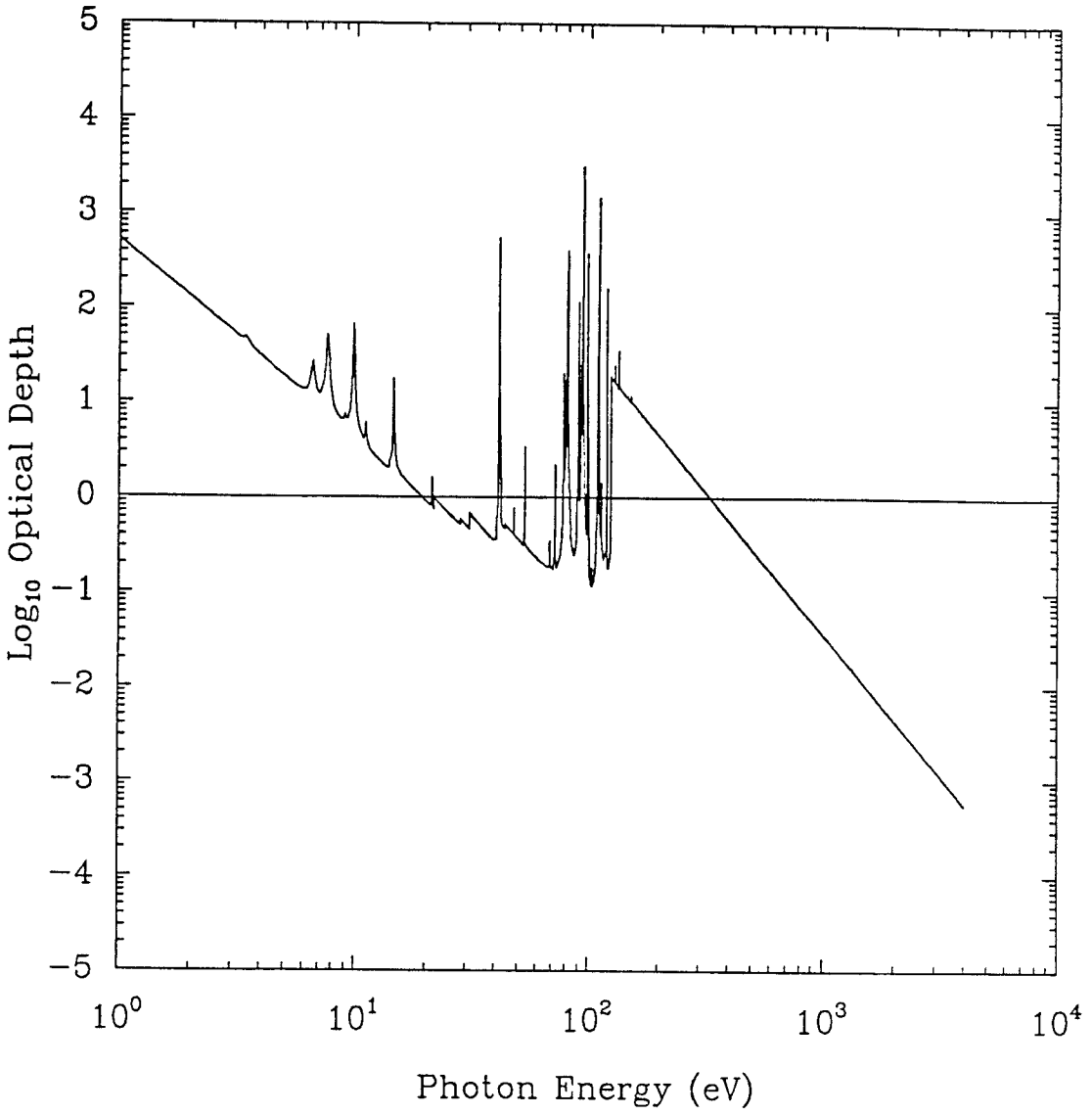

Figure 39. Dependence of optical depth on photon energy for the $T = 15$ eV case shown in Figure 37.

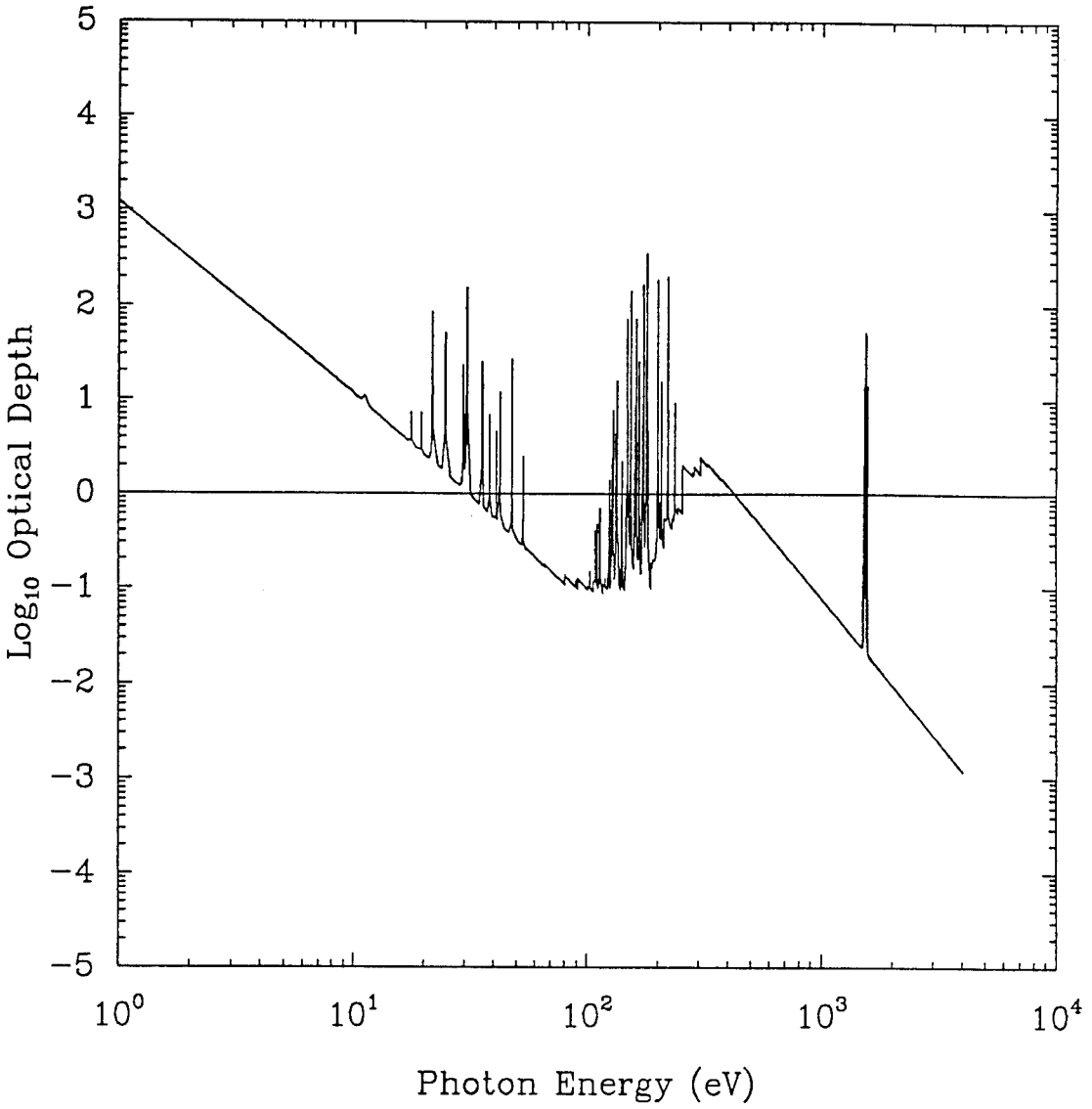

Figure 40. Dependence of optical depth on photon energy for the $T = 50$ eV case shown in Figure 37.

a second electron is ejected as the K shell vacancy is filled, or (2) a spontaneous decay to a lower lying level of Al VI in which a photon with an energy of about 1.5 keV is emitted. Thus, a relatively cool plasma is capable of emitting soft x-ray lines because of the beam-plasma interaction.

This is shown in Figure 42, where the spectral flux is shown for an Al plasma which is interacting with a 1.6 MeV, 0.3 TW/cm^2 proton beam. These beam conditions are typical of those expected for KALIF experiments (Bauer et al. 1988). The Al plasma is assumed to be at $T = 20$ eV, $n = 10^{-2}n_0$, and $L = 1$ mm; this corresponds to an original foil thickness of 10 μm. Note that at photon energies below 0.5 keV the flux is basically blackbody. This is because the plasma is optically thick at these photon energies (see Fig. 43). Near 1.5 keV, the K_α emission lines are clearly present. Figure 43 shows that these lines can be optically thick, with optical depths exceeding 10^3. This indicates that the self-attenuation of line radiation will significantly affect the emission spectrum.

Let us now examine in detail the narrow region of the spectrum near 1.5 keV in which the K_α lines are located. For the calculations in the remainder of this section, we assume the proton beam energy and power density are 5 MeV and 5 TW/cm^2, respectively. Figure 44 shows the K_α line spectrum calculated for an Al plasma with a temperature of 10 eV, a density of $10^{-1}n_0$, and original foil thickness of 10 μm. For comparison, the time-integrated experimental spectrum obtained on PBFA II at Sandia National Laboratories is shown (Bailey et al. 1991). Note that two curves are shown in the experimental plot. The upper curve represents the lower curve values magnified 15 times. The ionization indices refer to the ionization stage prior to proton impact ionization. In the experimental spectrum, K_α lines from Al I-IV, have the largest fluxes. The wavelengths for these ionization stages lie close together because the number of M shell electrons has little influence on the transition energy. However, as the Al becomes more ionized and the number of L shell electrons decreases, the K_α lines are noticeably blue-shifted. Ionization stages up to Al IX are clearly seen in the experimental spectrum.

The calculated relative intensities of the Al I-IV and Al V in Figure 44 agree quite well with the experimental spectrum. This suggests that the portion of the plasma most readily seen by the detector was at a temperature of about 10 eV or below for a majority of time during the experiment. At 10 eV, however, the plasma is too cold to produce K_α line radiation from the higher ionization stages.

Figure 45 shows the K_α spectrum from an Al plasma at 40 eV, $n = 10^{-2}n_0$, and $L_0 = 10$ μm. In this case, K_α lines from Al VIII and Al IX have the highest intensities. The calculated wavelengths of the K_α lines line up quite well with the peaks in the experimental spectrum. On the other hand, the relative strengths of the lines are not consistent with the time-integrated spectrum. This indicates that either: (1) the plasma spent a relatively short period of time at these temperatures, or (2) the K_α lines from the higher ionization

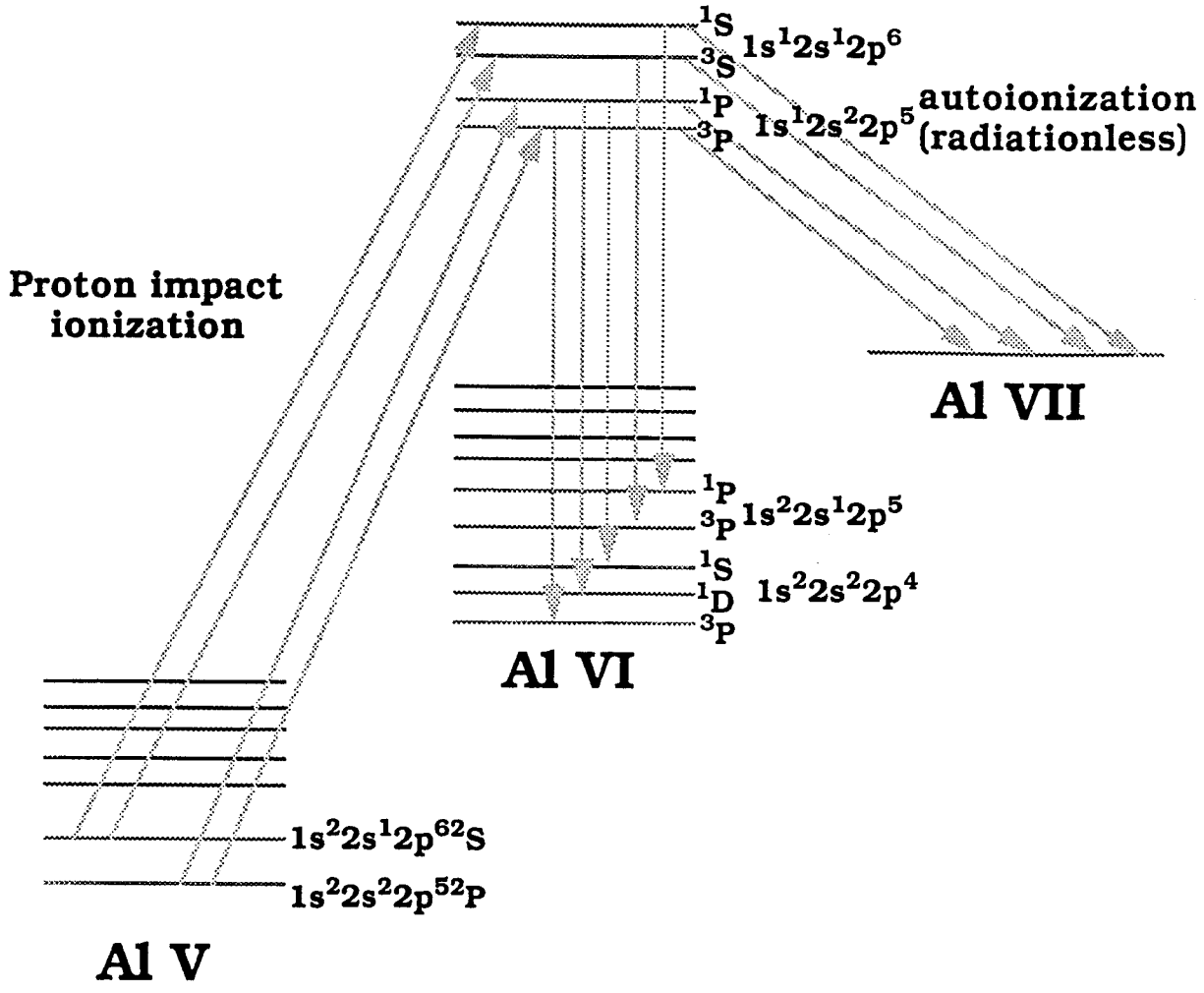

Figure 41. Schematic illustration of the atomic processes involved in the production of K_α fluorescence lines.

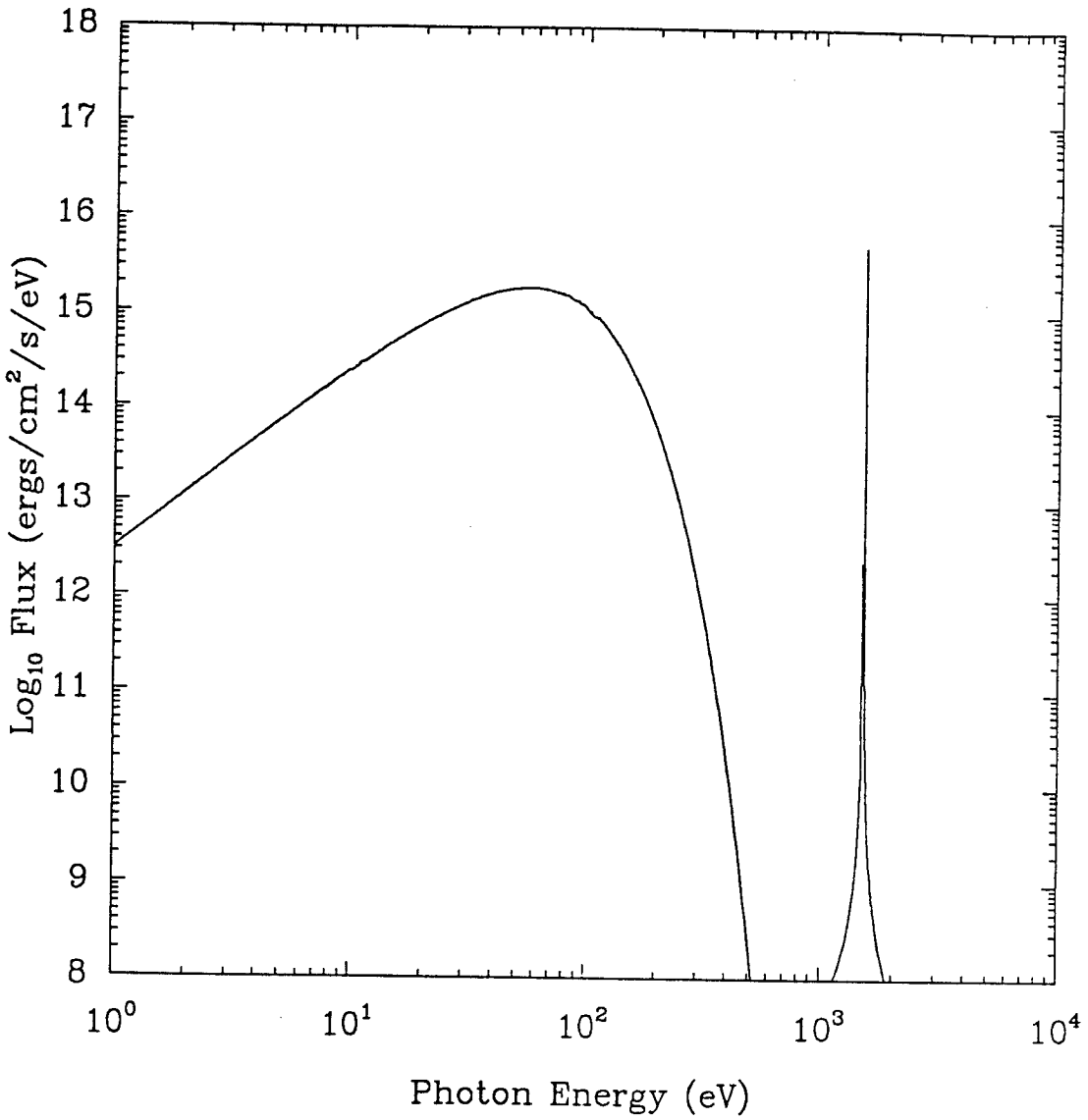

Figure 42. Spectral flux from an Al plasma being heated by a 1.6 MeV, 0.3 TW/cm^2 proton beam. The plasma conditions are $T = 20$ eV, $n = 10^{-2}n_0$, and $L = 1$ mm. The K_α lines are near 1.5 keV.

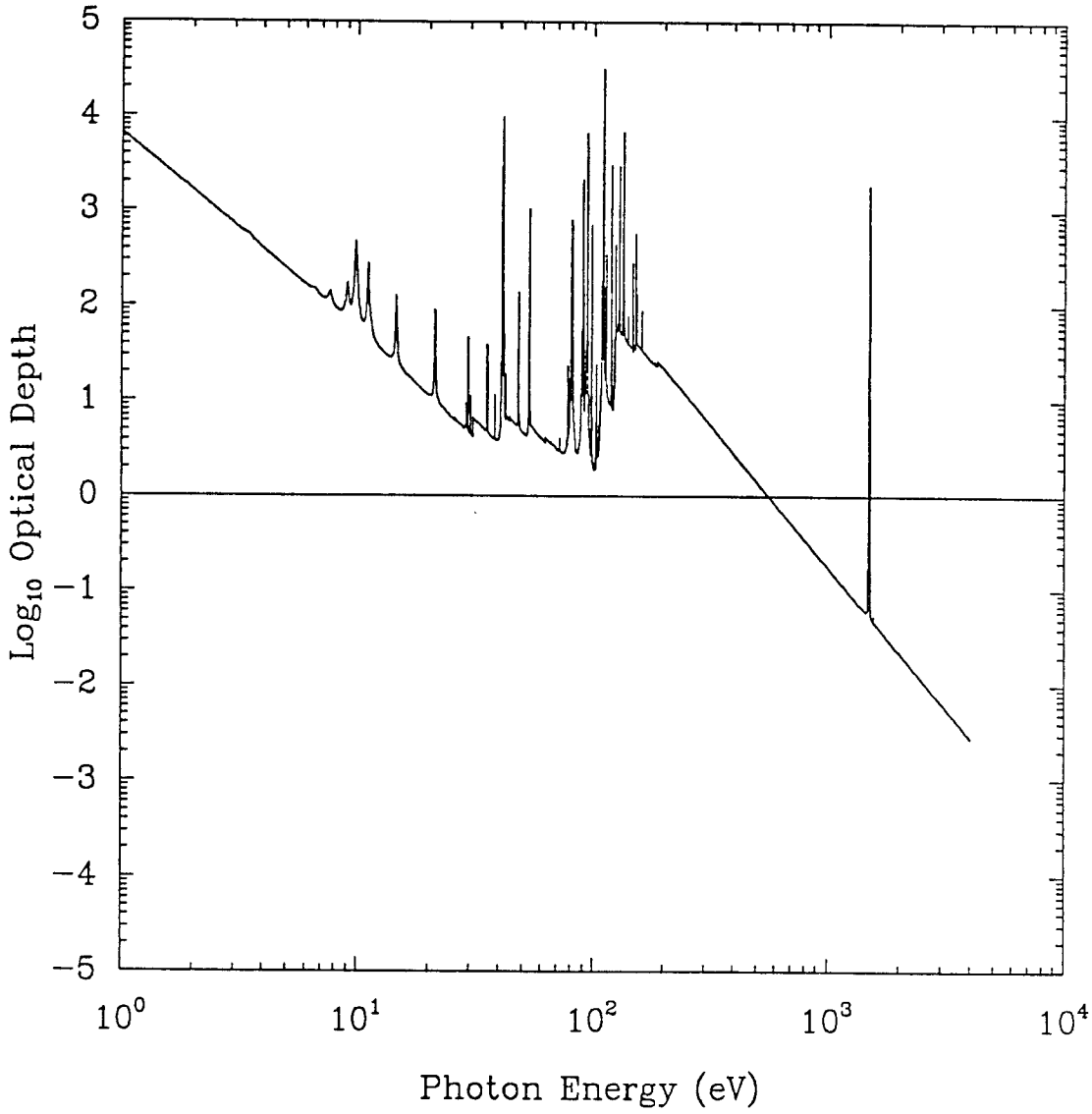

Figure 43. Frequency dependent optical depths for the case shown in Figure 42. Note the large optical depths for the K_α lines near 1.5 keV.

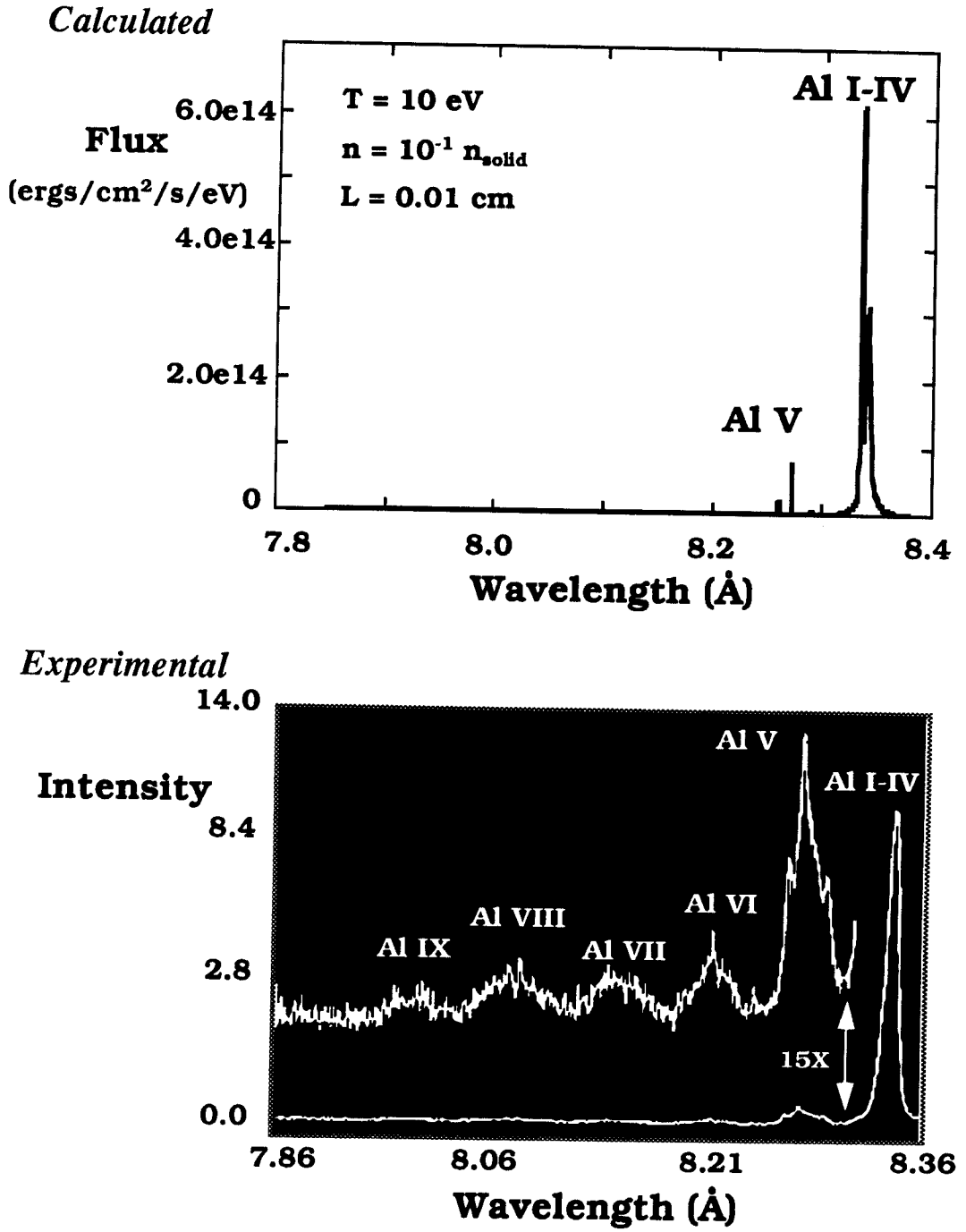

Figure 44. (Top) Calculated K_α line spectrum from an Al plasma at $T = 10$ eV, $n = 10^{-1} n_0$, and $L = 0.1$ mm being heated by a 5 MeV, 5 TW/cm^2 proton beam. (Bottom) Experimental time integrated spectrum from Bailey et al. (1991).

stages originate in a hotter region of the plasma, and these K_α lines are attenuated by cooler material that resides between the detector and the hot plasma. In this case, the attenuation would be primarily due to L shell photoabsorption.

The experimental data also shows some structure within the Al V profile. This region is shown in more detail in Figure 46, where again a calculated spectrum with $T = 20$ eV and $n = 10^{-1}n_0$ is compared with the experimental spectrum. We believe the structure in the experimental Al V profile results from at least 4 transitions. The calculated wavelengths for these transitions are indicated in the experimental plot. (See Section 5 for a description of the atomic physics calculations.) It is seen that 2 transitions at the "term" level ("fine structure" levels have not been considered) match up well with the central peak in the experimental spectrum. Figure 46 also shows the calculated relative intensities also agree well with the experimental spectrum. This good agreement with experimental data gives us confidence that K_α line radiation offers an excellent opportunity for diagnosing plasma conditions in ion beam-heated targets.

The influence of opacity effects on the radiation escaping the plasma is very significant. This is seen in Figure 47, where the K_α line fluxes from a $T = 40$ eV, $n = 10^{-2}n_0$ Al plasma are plotted for two cases. The dotted curve is from a calculation in which attenuation effects were ignored; that is, the plasma was assumed to be optically thin. The solid curve was obtained from calculations in which opacity effects were fully accounted for. Note that the fluxes in the optically thin case are typically 3 orders of magnitude higher than in the optically thick case. It is also seen that the relative fluxes of 2 lines can be significantly influenced by opacity effects. For instance, the Al VIII line at 8.04 Å is about a factor of 5 higher than the Al IX line at 7.98 Å in the optically thin case. However, when opacity effects are included, the lines have peak fluxes that are nearly equal. This clearly demonstrates the importance of transport effects in this spectral region for laboratory plasmas.

It is also of interest to know the location at which the K_α photons originate. Photons at the cores of optically thick lines originate near the "edge" of the plasma; that is, where the line center optical depth becomes small. On the other hand, photons from optically thin lines and those from the wings of optically thick lines can originate deep within the plasma and still be detected. This is shown in Figure 48, where the differential emission flux ($= \partial F(r, \nu)/\partial r$) is plotted as a function of frequency and position at which the photons originate. Note that the position axis is on a logarithmic scale and that the detector is at the right. The relatively dark regions are the regions with the largest fluxes. The way to interpret this plot is to look at the gradients in the differential flux at a given wavelengths (in the horizontal direction). At wavelengths where there are significant gradients, such as near 8.05 and 8.20 Å, the flux seen by the detector is due to photons originating very close to the edge of the plasma. At wavelengths where there are no noticeable gradients, the plasma is optically thin and behaves like a volume emitter.

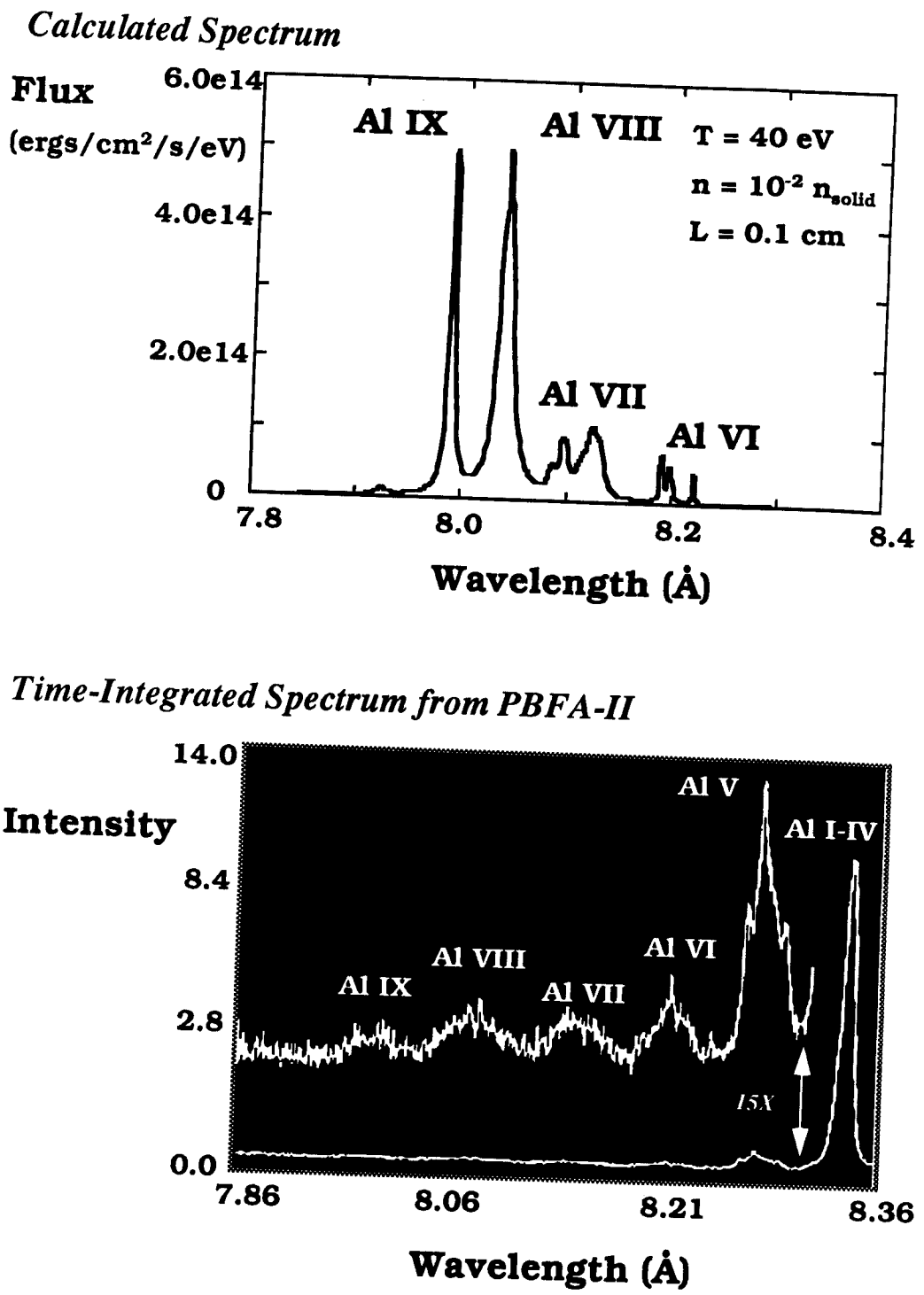

Figure 45. (Top) Calculated K_α line spectrum from an Al plasma at $T = 40$ eV, $n = 10^{-2} n_0$, and $L = 1.0$ mm being heated by a 5 MeV, 5 TW/cm^2 proton beam. (Bottom) Experimental time integrated spectrum from Bailey et al. (1991).

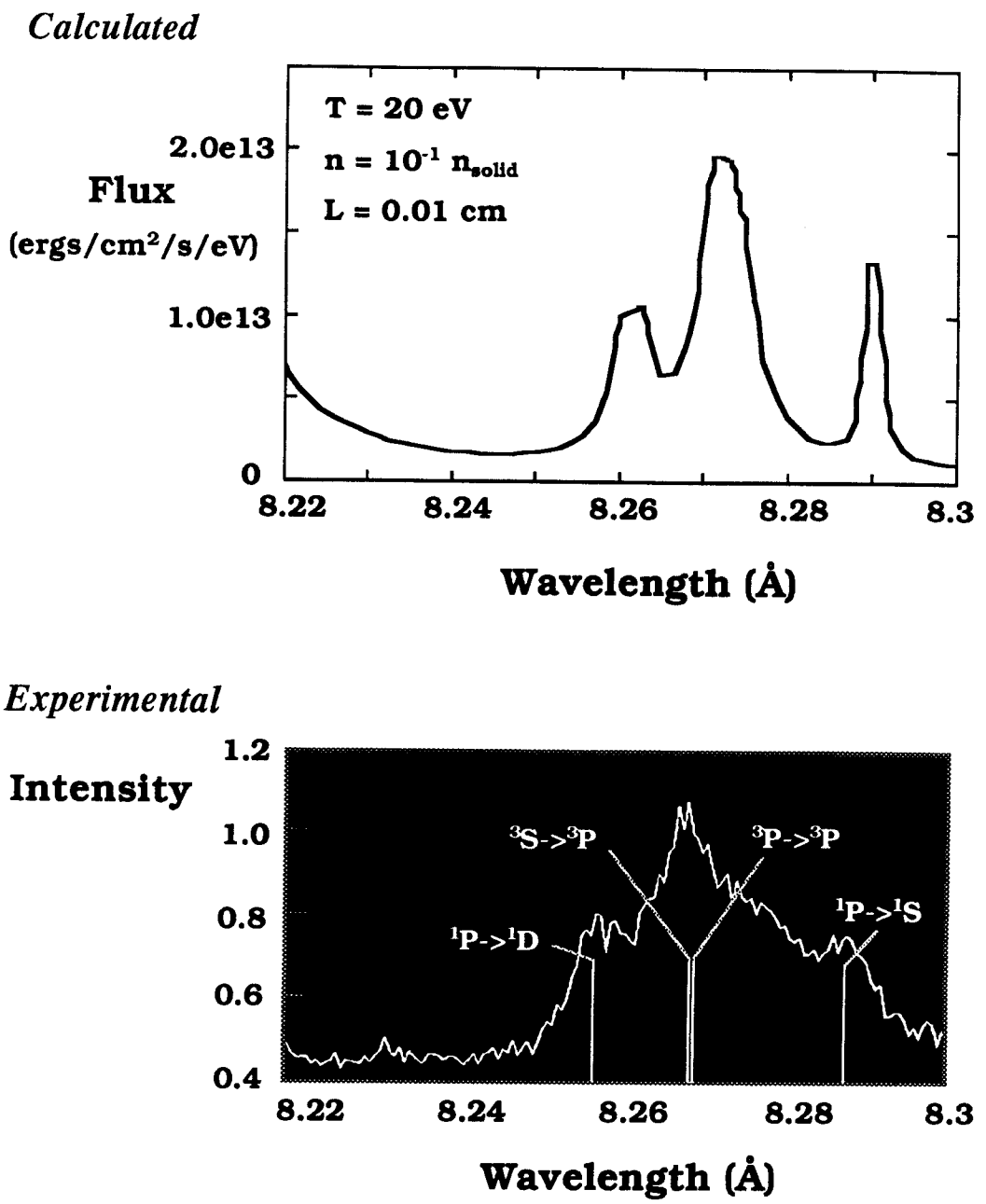

Figure 46. Comparison of calculated and experimental K_α spectrum for Al VI (Al V before proton impact ionization). The calculated spectrum is for an Al plasma at $T = 20$ eV, $n = 10^{-1}\ n_{solid}$, and $L = 0.01$ cm.

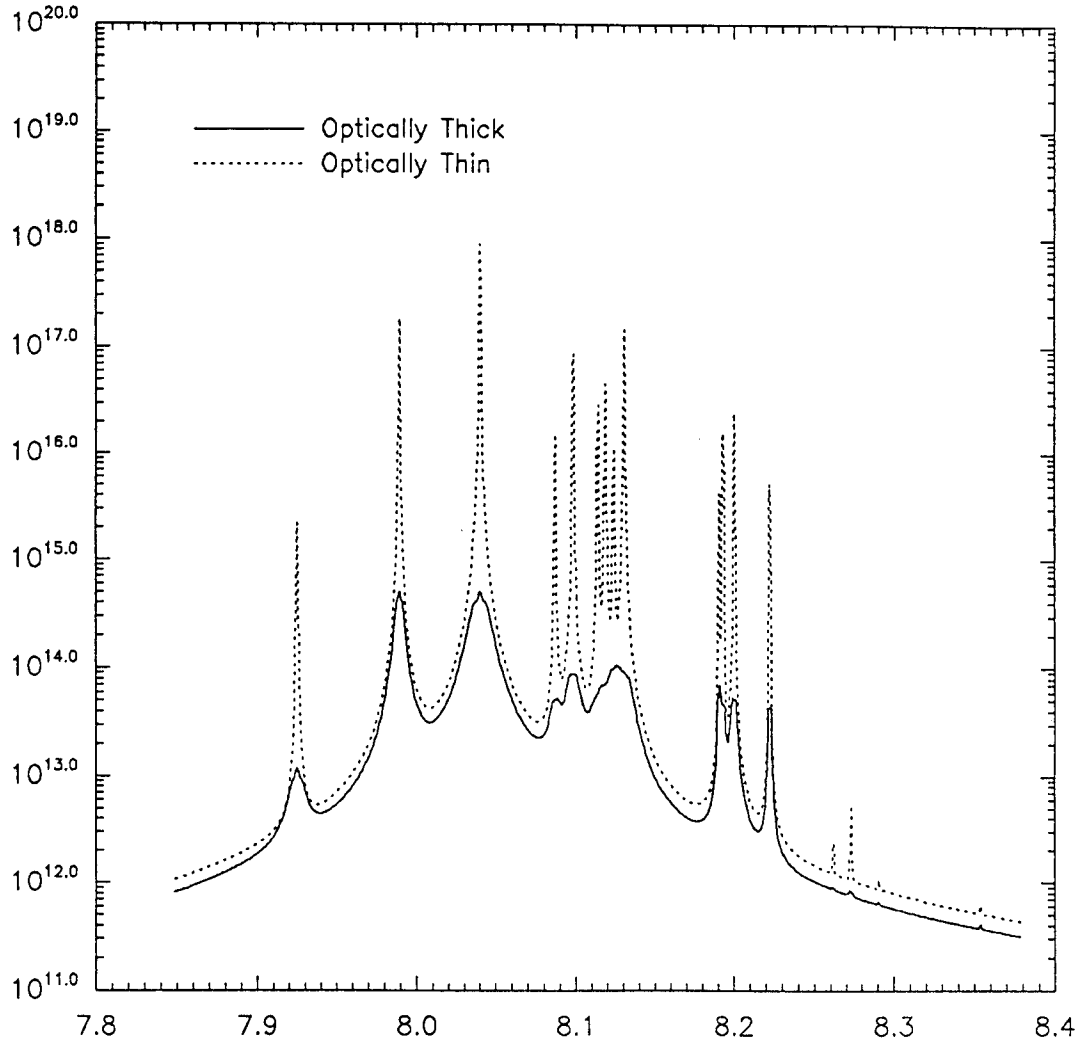

Figure 47. Comparison of calculated and experimental K_α spectral fluxes for an Al plasma at $T = 40$ eV, $n = 10^{-2}\ n_{solid}$, and $L = 0.01$ cm. The solid and dashed curves correspond to the optically thick and optically thin cases, respectively.

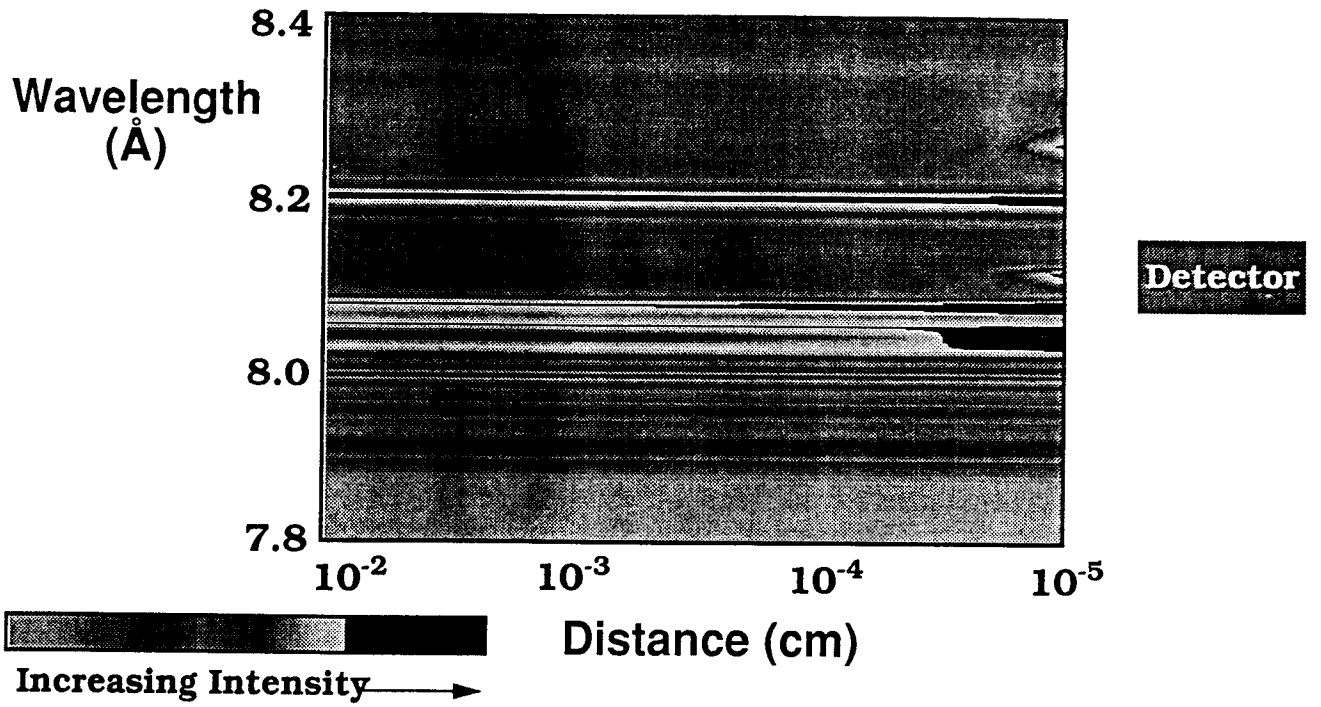

Figure 48. Contribution to the K_α spectral flux at the plasma boundary facing a detector. The areas near the boundary with large intensity gradients indicate the radiative seen by the detector at those wavelengths originate very close to the boundary. Note that the distance scale is logarithmic.

Clearly, the spectral intensities at different wavelengths provide information about the conditions at different locations in the plasma. Thus, in the K_α spectral region one can see into the plasma at different depths, and can attempt to deduce conditions in the interior regions of the plasma.

6.3. Recommendations for Beam-Plasma Experiments on KALIF

In the Sandia PBFA II experiments, it was seen that K_α satellite lines present a good opportunity for diagnosing plasma temperatures in beam-target interaction experiments. In that experiment, the proton beam energy was about 4-5 MeV, and power density was roughly 1-2 TW/cm^2 (Bailey et al. 1991). The peak electron temperature obtained in the Al target plasma was $\sim$ 20 to 60 eV. This temperature was high enough to produce significant amounts of Al with ionization stages above Al IV; that is, Al ions with K_α wavelengths that are easily distinguishable from those of Al I-IV.

Because the beam power density in KALIF experiments is expected to be lower than $\sim$ 0.3 TW/cm^2, it is unclear whether the plasma temperatures attained in KALIF experiments will greatly exceed 10 eV. This is an important consideration because Al V and higher ionization stages — that is, those ionization stages whose K_α lines can be experimentally resolved — begin to be present in significant amounts at temperatures $\gtrsim$ 10 eV. If the Al target plasma temperatures do not exceed 10 eV, it would be difficult to determine the ionization balance because the K_α lines of Al I-IV are difficult to resolve.

If plasmas temperatures exceed 10 eV in the KALIF experiments, plasma conditions can be deduced from the K_α line spectrum in conjunction with radiative transfer calculations. On the other hand, if plasma temperatures do not exceed 10 eV, we suggest 3 possible alternatives. First, one could consider measuring Al L_α line fluxes near 70 eV. Recall L_α lines are produced by a proton-impact ionization of an L-shell ($n = 2$) electron, followed by the subsequent transition of an electron from the M shell to the L shell. These lines may be detectable because: (1) the peak of the blackbody is down around 15 eV (see Fig. 37); (2) the continuum optical depths are $\lesssim 1$ for 10 μm foils (see Figures 38 and 39); and (3) the cross sections for proton impact ionization of L shell electrons is larger than those for K shell electrons (see Fig. 27). The L_α lines for Al I-IV could be expected to be resolvable experimentally because the transition energies should depend strongly on the number of electrons in the M shell.

A second possibility is to use a carbon-based target (perhaps some type of plastic). This is because the K_α lines for all ionization stages of carbon should be resolvable. This is seen in Table 7, where the transition energies and wavelengths for several ionization stages of carbon are listed. Note that the carbon lines are shifted by an amount comparable to those of the higher ionization stages of Al. For carbon $\Delta\lambda/\lambda \approx .07$ Å/42 Å = .017,

while for Al $\Delta\lambda/\lambda \approx .08$ Å/8 Å = .010. Thus, a spectrometer with comparable spectral resolution to that in the PBFA II experiment should be able to distinguish between the different ionization stages of carbon. The third possibility is to use an Al target that is doped with a small amount (perhaps 1%) of lower-Z material (perhaps $5 < Z < 10$); that is elements with a partially filled L shell. These elements would also have K_α lines that can be experimentally resolved.

Clearly, ion beam-induced transitions offer many possibilities for deducing plasma conditions in target experiments. Experimental spectra in conjunction with a judicious mix of hydrodynamics simulations and non-LTE radiative transfer calculation can lead to an improved understanding of beam-plasma interaction physics.

Table 7. K_α Transition Energies for Carbon*

Ion	Transition	Transition Energy (eV)	Wavelength (Å)
CII	$1s^1 2s^2 2p^2 \rightarrow 1s^2 2s^2 2p^1$	287.0	43.20
CIII	$1s^1 2s^2 2p^1 \rightarrow 1s^2 2s^2$	291.7	42.50
CIV	$1s^1 2s^1 2p^1 \rightarrow 1s^2 2s^1$	296.3	41.84
CV	$1s^1 2p^1 \rightarrow 1s^2$	304.2	40.75

*Based on single-configuration Hartree-Fock calculations. Relativistic effects are not included.

7. Summary

During the past year, we have made several improvements to our non-LTE radiative transfer model. New features that have been added include: the transport of bound-free radiation; the attenuation of line radiation by photoabsorption; the computation of frequency-dependent spectral fluxes at the plasma boundary; Stark line broadening effects; and methods to accelerate convergence when computing the atomic level populations. In addition, we have performed benchmark calculations using the ONEDANT transport code to test the accuracy of the angle- and frequency-averaging techniques in the radiative transfer code. Our results showed that the errors were typically $\sim 5-25\%$, a level of error which is quite modest for a model with such a high degree of computational efficiency.

We have also explored the possibility of using the Dirac chord length method to improve the angle-averaging technique in the radiative transfer code. We feel that because of the

non-uniform level population densities in non-LTE plasmas, this approach would lead to a sufficiently high degree of computational complexity that it would not be the best way to improve the accuracy of the radiative transfer code. It is thought a better way to proceed is to add a model which computes zone-to-zone coupling coefficients based on multiangle, multifrequency solutions to the radiative transfer equation. This approach would also allow for greater frequency-coupling between different atomic transitions, thus enabling the code to reliably model a wider range of spectral regimes.

Calculations were performed to simulate beam-plasma interaction experiments that could be performed on KALIF. Our results show that K_α satellite line radiation (near 1.5 keV for Al, and 0.29 keV for C) offers a good opportunity for diagnosing temperatures in ion-beam heated plasmas. Very good agreement was found between our numerical simulations and the experimental K_α spectrum obtained at Sandia National Laboratories on PBFA II.

In regards to beam-plasma interaction experiments to be performed on KALIF, we feel that targets that are composed (at least in part) of carbon may offer a better opportunity for diagnosing temperatures from K_α satellite lines than pure Al targets. This is because the K_α lines from the lowest 4 ionization stages of Al are very close together and are difficult to resolve experimentally. K_α lines from the lower ionization stages of C, however, are much more easily resolved experimentally. This is an important consideration if the maximum plasma's temperature attained in an experiment is $\sim$ 1-5 eV. One may also wish to consider either doping an Al target with a small amount ($\sim 1\%$) of a lower-Z element, or attempting to observe the L_α line spectrum from low-temperature Al plasmas. Additional calculations to support target experiments on KALIF will be performed in the future.

8. Acknowledgements

The authors gratefully acknowledge support from Kernforschungszentrum Karlsruhe (KfK) through Fusion Power Associates.

9. References

Alcouffe, R. E., Brinkley, F. W., Marr, D. R., and O'Dell, R. D. 1984, Los Alamos National Laboratory Report LA-10049-M, Los Alamos, N.M.

Apruzese, J. P. 1981, *J.Q.S.R.T.* **25**, 419.

Apruzese, J. P. 1985, *J.Q.S.R.T.* **34**, 447.

Apruzese, J. P., Davis, J., Duston, D., and Clark, R. W. 1984, *Phys. Rev. A* **29**, 246.

Apruzese, J. P., Davis, J., Duston, D., and Whitney, K. G. 1980, *J.Q.S.R.T.* **23**, 479.

Auer, L. 1987, in Numerical Radiative Transfer, ed. W. Kalkofen (Cambridge University Press, New York), p. 101.

Avrett, E. H., and Hummer, D. G. 1965, *Mon. Not. R. Astr. Soc.* **130**, 295.

Bailey, J., Carlson, A. L., Chandler, G., Derson, M. S., Dukart, R. J., Hammel, B. A., Johnson, D. J., Lockner, T. R., Maenshen, J., McGuire, E. J., Melhorn, T. A., Nelson, W. E., Ruggles, L. E., Stygar, W. A., and Wenger, D. F. 1991, *Lasers Part. Beams*, in press.

Bauer, W., Bluhm, H., and Goel, B. 1988, Kernforschungszentrum Karlsruhe Report 14-04-02P-16A, Karlsruhe, Germany.

Beigman, I. L., and Vainshtein, L. A. 1967, *Sov. Phys. JETP* **25**, 119.

Burgess, A., and Chidichchimo, M. C. 1983, *Mon. Not. R. Astr. Soc.* **203**, 1269.

Burgess, A., and Seaton, M. J. 1964, *Mon. Not. R. Astr. Soc.* **125**, 355.

Burgess, A., and Summer, H. P. 1976, *Mon. Not. R. Astr. Soc.* **174**, 345.

Case, K. M., de Hoffmann, F., and Placzek, G. 1953, Los Alamos National Laboratory Report, Los Alamos, New Mexico.

Chenais-Popovics, C., Fievet, C., Geindre, J. P., Gauthier, J. C., Luc Koenig, E., Wyart, J. F., Pepin, H., and Chaker, M. 1989, *Phys. Rev. A.* **40**, 3194.

Christensen, R. B., and Norcross, D. W. 1985, JILA Data Center Report No. 30, Boulder.

Clark, R. W., and Davis, J. 1990, *Phys. Fluids B* **2**, 1698.

Clark, R. W., Davis, J., and Cochran, F. L. 1986, *Phys. Fluids* **29**, 1971.

Dirac, P. A. M. 1943, Declassified British Report MS-D-5, Part I.

Duston, D., Clark, R. W., Davis, J., and Apruzese, J. P. 1983, *Phys. Rev. A* **27**, 1441.

Duston, D., and Davis, J. 1981, *Phys. Rev. A* **23**, 2602.

Falk, R. A., Dunn, G. H., Griffin, D. C., Bottcher, C., Gregory, D. C., Grandall, D. H., and Pindzola, M. S. 1981, *Phys. Rev. Lett.* **47**, 494.

Hummer, D. G., and Voels, S. A. 1988, *Astron. Astrophys.* **192**, 279.

Khan, J. M., Potter, D. L., and Worley, R. D. 1965, *Phys. Rev.* **139**, A1735.

Karzus, W. J., and Latter, R. 1961, *Astrophys. J. Suppl. Ser.* **6**, 167.

Kavenoky, A. 1969, CEA-N-1077, Centre d' Etudes Nucléaires de Saclay, France.

Kier, P. H., Robba, A. A. 1967, Argonne National Laboratory Report ANL-7326.

Kier, P. H. 1965, Argonne National Laboratory Report ANL-7033.

Kunasz, P. B., and Hummer, D. G. 1974, *Mon. Not. R. Astr. Soc.* **166**, 19.

Lewis, E. E. 1967, *Nucl. Sci. and Eng.*, **28**, 311.

MacFarlane, J. J., Wang, P., and Moses, G. A. 1990, University of Wisconsin Fusion Technology Institute Report UWFDM-822 and Fusion Power Associates Report FPA-90-1, Madison, WI (Paper I).

Marr, G. V., and West, J. B. 1976, *At. Data Nucl. Data Tables* **18**, 497.

Mihalas, D. 1978, Stellar Atmospheres, Second Edition (Freeman, New York).

Mihalas, D., Mihalas, B. W. 1984, Foundations of Radiation Hydrodynamics, Oxford University Press.

Nardi, E., and Zinamon, Z. 1981, *J. Appl. Phys.* **52**, 7025.

Ng, K. C. 1974, *J. Chem. Phys.* **61**, 2680.

Olson, G. L., Auer, L. H., and Buchler, J. R. 1986, *J.Q.S.R.T.* **35**, 431.

Post, D. E., Jensen, R. V., Tarter, C. B., Grasberger, W. H., and Lokke, W. A. 1977, *At. Data Nucl. Data Tables* **20**, 397.

Reilman, R. F., and Manson, S. T. 1979, *Astrophys. J. Suppl. Ser.* **40**, 815.

Rybicki, G. B. 1971, Conference on Line Formation in the Presence of Magnetic Fields, National Center for Atmospheric Research Report, Boulder, CO.

Samson, J. A. R., and Cairns, R. B. 1965, *J. Opt. Soc. Am.* **55**, 1035.

Smith, M. W., and Weise, W. 1971, *Astrophys. J. Suppl. Ser.* **23**, 103.

Solelman, I. I., Vainshtein, L. A., and Yukov, E. A. 1981, Excitation of Atoms and Broadening of Spectral Lines (Springer-Verlag, New York).

Tsuchihashi, T. 1979, JAREI-1259 (1979).

Tsuchihashi, T. 1983, JAERI-1285, and 1986, JAERI-1302.

Van Wyngaarden, W. L., and Henry, R. J. W. 1976, *J. Phys. B* **9**, 1461.

Wang, P. 1991, Ph.D. Dissertation, Dept. of Nuclear Engineering and Engineering Physics, University of Wisconsin, in preparation.